Investigation of Static and Dynamic Reaction Mechanisms at Interfaces and Surfaces Using
Density Functional Theory and Kinetic Monte Carlo Simulations

Thomas L. Danielson

Dissertation submitted to the faculty of the Virginia Polytechnic Institute and State University in
partial fulfillment of the requirements for the degree of

Doctor of Philosophy
In
Materials Science and Engineering

Celine Hin
William T. Reynolds
David E. Clark
Diana Farkas

Investigation of Static and Dynamic Reaction Mechanisms at Interfaces and Surfaces Using
Density Functional Theory and Kinetic Monte Carlo Simulations

Thomas L. Danielson

Abstract

The following dissertation is divided into two parts. Part I deals with the modeling of
helium trapping at oxide-iron interfaces in nanostructured ferritic alloys (NFAs) using density
functional theory (DFT). The modelling that has been performed serves to increase the knowledge
and understanding of the theory underlying the prevention of helium embrittlement in materials.
Although the focus is for nuclear reactor materials, the theory can be applied to any material that
may be in an environment where helium embrittlement is of concern. In addition to an improved
theoretical understanding of helium embrittlement, the following DFT models will provide
valuable thermodynamic and kinetic information. This information can be utilized in the
development of large-scale models (such as kinetic Monte Carlo simulations) of the
microstructural evolution of reactor components. Accurate modelling is an essential tool for the
development of new reactor materials, as experiments for components can span decades for the
lifetime of the reactor.

Part II of this dissertation deals with the development, and use of, kinetic Monte Carlo
(KMC) simulations for improved efficiency in investigating catalytic chemical reactions on
surfaces. An essential technique for the predictive development and discovery of catalysts relies
on modelling of large-scale chemical reactions. This requires multi-scale modelling where a

common sequence of techniques would require parameterization obtained from DFT, simulation of the chemical reactions for millions of conditions using KMC (requiring millions of separate simulations), and finally simulation of the large scale reactor environment using computational fluid dynamics. The tools that have been developed will aid in the predictive discovery, development and modelling of catalysts through the use of KMC simulations. The algorithms that have been developed are versatile and thus, they can be applied to nearly any KMC simulation that would seek to overcome similar challenges as those posed by investigating catalysis (such as the need for millions of simulations, long simulation time and large discrepancies in transition probabilities).

Dedication

With love to my mother and father, to whom I owe a lifetime of gratitude for their unconditional love and support.

Acknowledgements

Table of Contents

List of Figures

List of Tables

Attributions

Celine Hin – Ph.D., Institut National Plytechnique de Grenoble, France, 2005. Assistant Professor, Department of Materials Science and Engineering and Department of Mechanical Engineering, Virginia Tech.

Aditya Savara – Ph.D., Northwestern University, Evanston, IL, 2008. Staff Scientist, Oak Ridge National Laboratory.

Eric Tea – Ph.D., Université Paris-Sud, France, 2011. Post Doctoral Research Associate in Celine Hin's research group, Virginia Tech.

Specific Contributions of Co-Authors

Dr. Celine Hin was a PI or Co-PI in all portions of the dissertation.

Dr. Aditya Savara was a Co-PI with Dr. Celine Hin in Part II of the dissertation

Chapter 4

Dr. Eric Tea provided calculations of the potential energy landscape in Y_2O_3.

Chapter 5

Dr. Eric Tea provided calculations of the potential energy landscape in $Y_2Ti_2O_7$.

Chapter 6

Dr. Eric Tea provided significant guidance on performing potential energy landscape calculations of the oxide nanocluster.

Part I - The ab initio Investigation of Helium Trapping at Oxide Nanoclusters in Nanostructured Ferritic Alloys

1.   Introduction

As of January 2016, the global human population has well surpassed 7 billion with an expected population exceeding 8 billion by the year 2025, according to the estimates and projections of the US Census Bureau. With this rising population comes an ever increasing need to expand the global energy grid in order to meet the increased demand for the output of power. Currently, much of the world's energy grid relies heavily on the use of fossil fuels for energy production. However, rising concern of the human influence on global climate change from greenhouse gas emissions has created the need to seek alternative energy that is capable of producing large outputs with significantly decreased emissions. Nuclear energy, produced by the fission or fusion of atoms, is orders of magnitude more energy dense than any fossil fuel and the power production results in negligible emission of greenhouse gases. As a result, nuclear energy is one of the most promising contributors for the expansion of the global energy grid and consequently, nuclear reactor technology and efficiency continue to evolve. However, the need to produce power in an environmentally clean and safe manner remains a primary concern.   One of the first lines of defense for protecting the population and the environment from nuclear contamination are the materials used for reactor components.   Materials that are capable of containing the nuclear reactions must be capable of withstanding high temperatures, high pressures, high neutron flux, and the creation of transmutation products, such as He. One of the most promising alloys for serving such purposes are a class of oxide dispersion strengthened steels called nanostructured ferritic alloys (NFAs) [1].

The highly non-equilibrium alloying processes carried out to create NFAs produce several microstructural characteristics that are responsible for their prime candidacy as reactor fuel

claddings, structural materials and first wall components. The most defining microstructural characteristic is the high number density of oxide nanoclusters, which are responsible for precipitation hardening the material, maintaining a high dislocation density at high temperatures and most importantly, for the purposes of this dissertation, trapping the transmutation product, helium. In the subsequent chapters, a thorough investigation of the interaction of helium with two common oxide nanoclusters in NFAs, Y_2O_3 and $Y_2Ti_2O_7$, is carried out using density functional theory (DFT) in order to develop an understanding of the helium trapping mechanisms of oxide nanoclusters in NFAs. It will be shown that the largest interaction between helium and the oxides is with the constituent oxygen atoms, the extent of which is electron-electron repulsion. Even with this it is shown that helium is significantly more energetically stable in the oxide than in Fe. The kinetics of helium are thoroughly investigated to show that the migration barriers are significantly higher in the oxides than in BCC Fe due to the imposition brought forth by complex potential energy surfaces of the oxides. Finally, an investigation which embeds a nanocluster in the Fe matrix is carried out which will show that trapping becomes favorable due to significant differences in the potential energy surface of Fe and the oxide. This arises from differences between the metallic bonding in Fe and localized iono-covalent bonding in the oxides. From this, a complete understanding of the trapping mechanisms of helium at the oxide-Fe interface is developed in order to further the understanding of the materials community on the prevention of helium embrittlement.

References
[1] G.R. Odette, M.J. Alinger, B.D. Wirth, Annual Review of Materials Research, 38 (2008) 471-503.

2.   Introduction to Density Functional Theory

Density functional theory (DFT) has become an increasingly useful computational tool for materials research since the advent of supercomputers. DFT is capable of providing structural, electronic and energetic information pertaining to atomic, molecular and crystalline specimens. The current section will outline the underlying features of DFT and will provide a description of the techniques that have been used to analyze the data from DFT simulations of helium in NFAs. In the current work, DFT as implemented by the VASP code has been used for all simulations and the following framework will be discussed in the context of VASP.

Density functional theory approximates a solution to the many-body Schroedinger equation:

$$\hat{H}\Psi = [\hat{T} + \hat{V} + \hat{U}]\Psi = [\sum_{i}^{N}(-\frac{\hbar^2}{2m_i}\nabla_i^2) + \sum_{i}^{N}V(\vec{r}_i) + \sum_{i<j}^{N}U(\vec{r}_i,\vec{r}_j)]\Psi = E\Psi$$

where, *H,* the Hamiltonian, is defined by the sum of the kinetic energy, *T*, the potential energy of external positively charged nuclei, *V,* and the interaction between electron pairs, *U. E* and Ψ are the ground state energy of the system and the electron wavefunction respectively. This problem is extremely computationally expensive due to the electron-electron interaction term. This term considers the interaction of an electron with all other electrons in the system and thus, computational time scales exponentially with the number of atoms. To simplify the problem and alleviate this significant computational expense, the description of atomic species is performed using pseudopotentials that are dependent upon a plane-wave basis set. The pseudopotentials treat the atomic nucleus and the core electrons as fixed and only treat a certain number (depending on atomic species) of electrons as interacting valence electrons. An additional simplification was proposed by Hohenberg and Kohn, which has now become the framework for DFT: the specification of the ground state density, *n(r)*, determines the external potential *V(r)* uniquely [1,2].

Derived from the theory of Hohenberg and Kohn are the Kohn – Sham equations, which give the ground state energy in DFT. The Kohn – Sham equations are expressed as follows:

$$(-\frac{1}{2}\nabla^2 + \upsilon(r) + \int \frac{n(r')}{|r-r'|}dr' + \upsilon_{xc}(r) - \varepsilon_j)\varphi_j(r) = 0$$

$$n(r) = \sum_{j=1}^{N} |\varphi_j(r)|^2$$

$$\upsilon_{xc}(r) = \delta E_{xc}[n(r)]/\delta n(r)$$

Where φ_j are the orbitals from which the density $n(r)$ is derived. Finally, the ground state energy can be expressed as [1,3]:

$$E = \sum_{1}^{\upsilon} \varepsilon_j - \frac{1}{2}\int \frac{n(r)n(r')}{|r-r'|}dr\,dr' - \int \upsilon_{xc}(r)n(r)dr + E_{xc}[n(r)]$$

These equations are exact so long as the description of the energy associated with exchange and correlation between valence electrons, E_{xc}, is exact. E_{xc} can be defined in the pseudopotentials in multiple ways: within (i) the local density approximation (LDA), (ii) the local spin density approximation (LSDA) and (iii) the generalized gradient approximation (GGA). For the purpose of this research, only the generalized gradient approximation (GGA) has been used to describe the exchange-correlation effects and this approximation is generally regarded as the most accurate. Within the GGA, E_{xc} is defined as:

$$E_{xc}^{GGA} = \int f(n(r),|\nabla n(r)|)dr$$

Which takes into account both the charge density $n(r)$ and the gradient of the charge density (for a more rigorous derivation of the Hohenberg – Kohn and Kohn-Sham formulations, see references 1-3).

Within the Kohn-Sham framework of DFT, computing time typically scales with N^2 or N^3, where N is the number of atoms [1]. Typically, DFT simulations are on the order of hundreds of atoms or less, depending on what is being tested. For simple structural calculations of a single

crystal with no defects, the primitive cell is typically sufficient to obtain accurate representations of the structure. However, for calculations of crystals containing defects, supercell calculations are necessary in order to ensure that periodic defects are non-interacting and convergence of the total energy of the system should be tested to find the minimum sufficient simulation size.

In order to investigate the interaction of helium with oxide nanoclusters in NFAs, the following techniques and data have been utilized:

- The charge density

- The electron localization function (ELF)

- The nudged elastic band method (NEB)

- The helium potential energy surface (PES) in the crystal

where, the charge density and ELF provide insight to changes in the constituent bonds and the interaction between helium and neighboring atoms, the NEB gives energetic barriers for helium and the path associated with the barrier, and the PES provides the energy landscape from the perspective of a helium atom within the crystal.

References
 [1] W. Kohn, A.D. Becke and R.G. Parr. J. Phys. Chem. **100**, 12974-12980 (1996).

[2] P. Hohenberg and W. Kohn. Phys. Rev. **136**, 3B (1964).

[3] W. Kohn and L.J. Sham. Phys. Rev. **140**, 4A (1965).

3. Structural and electronic effects of helium interstitials in $Y_2Ti_2O_7$: A first-principles study

3.1 Abstract

Results describing the interaction of helium with the $Y_2Ti_2O_7$ structure are presented. Density functional theory has been used to determine the solution energy of a variety of interstitial sites in $Y_2Ti_2O_7$, as well as to explain the effects of helium on the electronic structure. A large effect due to electron – electron repulsion is observed between the oxygen and helium electrons and an overall change in the bonding nature of atoms in the immediate vicinity is noticed when helium interstitials are present. This is a preliminary study to understanding the mechanisms causing complex oxide nanoclusters to serve as trapping sites for helium in nanostructured ferritic alloys.

3.2 Authors and Affilitations

Thomas Danielson[1] and Celine Hin[1,2]

[1]Department of Materials Science and Engineering, Virginia Polytechnic Institute and State University, Blacksburg, VA, USA

[2]Department of Mechanical, Virginia Polytechnic Institute and State University, Blacksburg, VA, USA

[*]Corresponding Author Email: thomasd1@vt.edu

3.3 Introduction

Nanostructured ferritic alloys (NFAs) have shown great promise as first wall and structural components for advanced fission and fusion reactor systems due to their capability of withstanding high neutron fluence, high temperatures and pressures, and high concentrations of transmutation product helium due to (n,α) reactions[1-4]. The accumulation of helium, especially due to its

negligible solubility in metals, presents a major challenge in selecting the appropriate materials for withstanding harsh reactor environments[5]. Many studies have been devoted to understanding the characteristics and theory of helium in metals.

Ab initio simulations have shown that the self-interaction of helium interstitials in iron is attractive making the formation of helium clusters favorable [6]. Production of helium during irradiation is accompanied by displacement damage and a resulting vacancy concentration far beyond equilibrium. Vacancies act to stabilize the formation of clusters of helium, and lead to the eventual growth of larger helium bubbles [6-8]. The very low migration barrier of helium in BCC iron results in diffusion of interstitials to preferential nucleation sites such as dislocations, grain boundaries and voids [6,9-12]. Especially at high temperatures (i.e. $T > \frac{1}{2} T_m$), helium bubbles become highly pressurized leading to significant deformation of the surrounding lattice, ultimately compromising the mechanical properties of the material [13,14]. Implantation experiments have shown the consequence of pressurized bubble induced lattice deformation to be intergranular fracture under applied stress due to helium embrittlement [15,16]. Similarly, it has been shown that tensile stress increases the rate of growth of helium bubbles, especially along grain boundaries and triple junctions, of particular concern in high-pressure reactor environments [17]. Thus, it is of critical importance to prevent helium bubble formation along grain boundaries, dislocations and voids.

NFAs offer a promising solution to the problem of moderating the formation of large helium bubbles at high-risk locations due to the presence of a high number density of complex oxide nanofeatures (NFs) that act as trapping sites for helium. There are three main mechanisms for the transport of helium from matrix to the grain boundaries; helium diffusion, helium bubble migration and by the motion of dislocations [5,16]. As helium diffuses along dislocation networks

and through the matrix material, the $Y_2Ti_2O_7$, Y_2O_3 and Y_2TiO_5 NFs impede diffusion of helium and act as trapping sites for helium bubble formation, preventing its eventual delivery to grain boundaries [9]. Transmission electron microscopy experiments carried out by Edmondson et al. have shown evidence of bubbles trapped at NFs, where approximately 4.4% of bubbles are located on coarsened precipitates and approximately 48.6% are trapped at NFs, where the surface of the NF is nearly completely covered by bubbles [12,18,19]. Trapped helium bubbles also act as very effective trapping sites for helium atoms diffusing through the material effectively decreasing the amount of helium that reaches grain boundaries [16]. Thus, effective helium trapping at NFs has the potential to significantly reduce the risk of helium embrittlement.

Despite experimental evidence showing NFs acting as helium bubble trapping sites, a theoretical understanding of the energetic mechanisms governing the nucleation, growth and trapping of bubbles at the surface of NFs is lacking. In order to develop a more thorough understanding of these phenomena, multi-scale models must be developed to model the kinetics of helium in candidate materials for nuclear reactor environments. The parameterization of multi-scale models relies on obtaining different thermodynamic and kinetic information (i.e. solution energies, defect formation energies, migration barriers, etc.) both in the ferrite matrix and in the oxide nanoclusters. The ability to develop more accurate models of helium in reactor environments will enable further prevention of helium embrittlement in the next generation of nuclear reactors. Thus, this study deals with the behavior of He in $Y_2Ti_2O_7$ using density functional theory (DFT). We determine the different interstitial positions available for helium in the oxide, the relative stability of each interstitial position, as well as the structural and electronic interactions of helium with $Y_2Ti_2O_7$. Each of these results will be useful data to parameterize kinetic Monte

Carlo simulations in order to study the trapping effect of helium at the interface between the oxides and the ferritic matrix.

In the next Section, the simulation setup and theory are presented. Section 3.5 presents the results obtained on the relative stability of interstitial sites, the structural and electronic effects of helium interstitials. Finally, a discussion of the results and their significance is presented in section 3.6.

3.4   Theory and Calculation

The structure of $Y_2Ti_2O_7$ has been explored using density functional theory (DFT) in order to determine the relative stability and electronic effects of He interstitials on the ground state properties of the lattice. DFT calculations have been performed as implemented by the VASP code [20-23] using pseudopotentials generated with the projector-augmented wave (PAW) method [24,25]. The generalized gradient approximation (GGA) from Perdew, Berke and Ernzerhof (PBE) [26,27] describes the exchange-correlation effects. The semi core 3p electrons and the 4s and 4p electrons have been treated as valence electrons for Ti and Y respectively. A uniform 4x4x4 Monkhorst-Pack K-mesh has been used for brillouin zone integration. A Gaussian smearing scheme with a width of .05 eV has been used for two relaxations, and the tetrahedron method has been used for a final static calculation of the ground state energy of the system, as well as the density of states. The energy with respect to K-points has been converged to less than 0.001 eV. The plane wave energy cutoff has been tested within the range from 500 to 650 eV, where the variation of total energy is within 0.05 percent of the total energy. A plane wave energy cutoff of 598.62 eV has been used. Relaxation of the electronic structure has been converged to 10^{-7} eV. For each simulation, one fully periodic unit cell has been used, where the ions, cell volume and cell shape are each relaxed to their ground state.

DFT-GGA does not explicitly account for Van der Waals interactions. Because of this, the isolated He – He interaction energy has been tested at a range of interatomic distances from 0.15 to 0.4 nm and compared with full configuration interactions (CI) [28] and quantum Monte Carlo (QMC) simulations [29] which do include Van der Waals interactions. This has been performed for different He GGA potentials in order to determine the most accurate description of the helium atom available in VASP. The GGA from PBE shows the best agreement (Figure 3.1) with the CI and QMC simulations with the largest absolute difference being .0225 eV and thus, the method of PBE has been used for describing the exchange correlation effects with confidence that VASP can appropriately reproduce the behavior of helium.
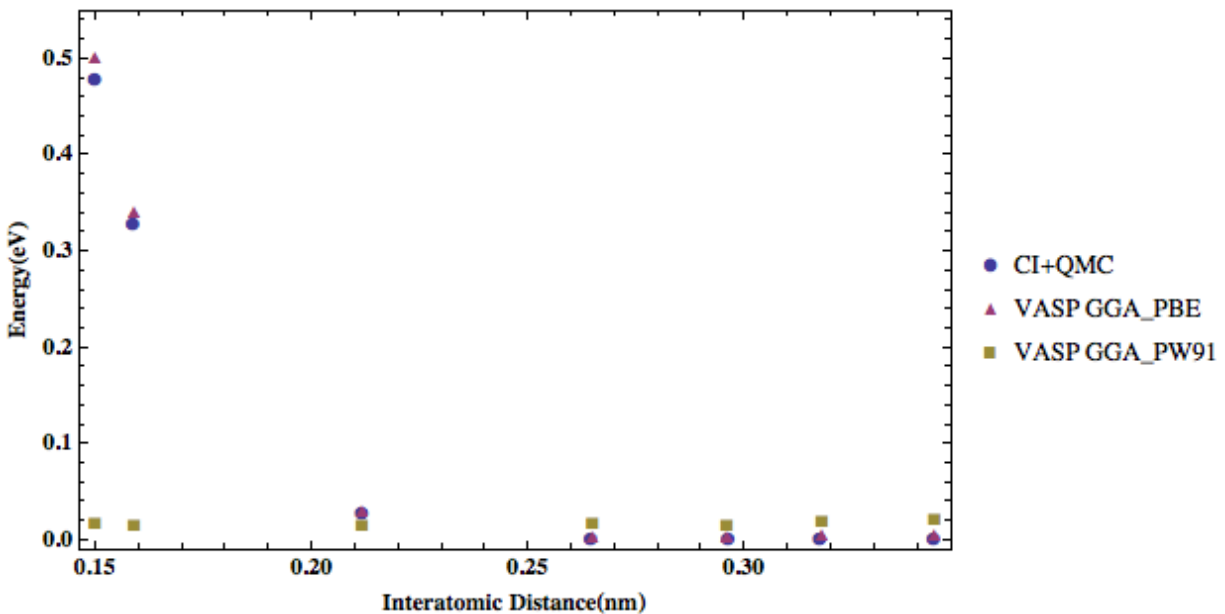
Figure 3.1 Comparison of the interaction energy of a helium dimer in the ranges of 0.15 and 0.344 nm with CI [28] and QMC [29] data using potentials from PBE [26,27] and PW91 [30,31] as implemented in VASP[20-23].

$Y_2Ti_2O_7$ belongs to the space group Fd-3m having the pyrochlore structure (Figure 3.2). It consists of Y, Ti, O and O' at the 16d (1/2, 1/2 , 1/2) , 16c (0, 0, 0) , 48f (x, 1/8, 1/8) and 8b (3/8, 3/8, 3/8) Wyckoff positions. The O8a (1/8, 1/8, 1/8) position is a vacant site surrounded tetrahedrally by four Ti atoms. The structural parameters (Table 3.1) and density of states (DOS)

(Figure 3.3) of the defect free $Y_2Ti_2O_7$ system have been verified with existing DFT calculations [32,33]. The experimental lattice parameter of $Y_2Ti_2O_7$ has been determined many times as 1.009 nm [34,35]. Upon full relaxation, our setup renders a lattice parameter of 1.0192 nm, in good agreement with other DFT calculations for $Y_2Ti_2O_7$ [33].

Table 3.1 Bond distances and angles for the $Y_2Ti_2O_7$ system.

Bond	Bond Distance	Bond Distance
Y - O	0.2503	0.2488
Y - O'	0.2207	0.219
Ti - O	0.1976	0.1959
O - O	0.2631	0.2613
O - O'	0.3011	0.2994
	Bond Angles	Bond Angles
O - Y - O	116.5825	116.642
O - Ti - O	83.4773	83.683
	[a]Ref. [32]	
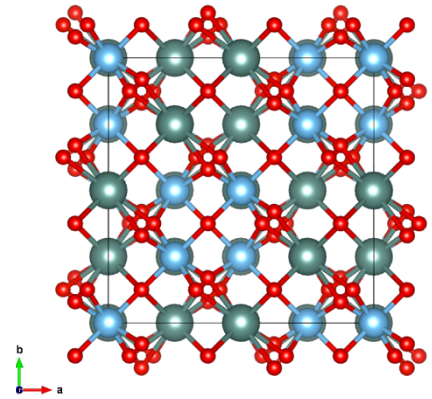
Figure 3.2 $Y_2Ti_2O_7$ crystal structure. Red, green and blue atoms are O, Y and Ti respectively
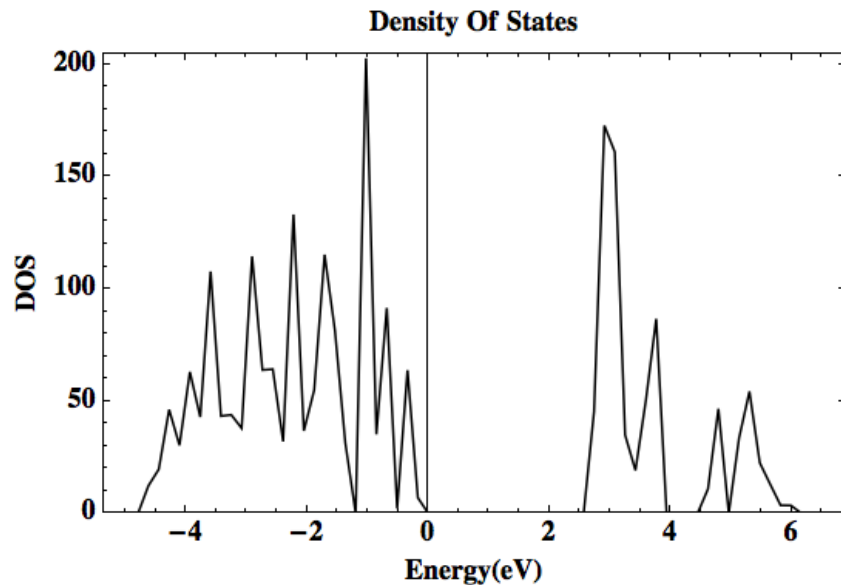
Figure 3.3 Calculated total density of states for $Y_2Ti_2O_7$.
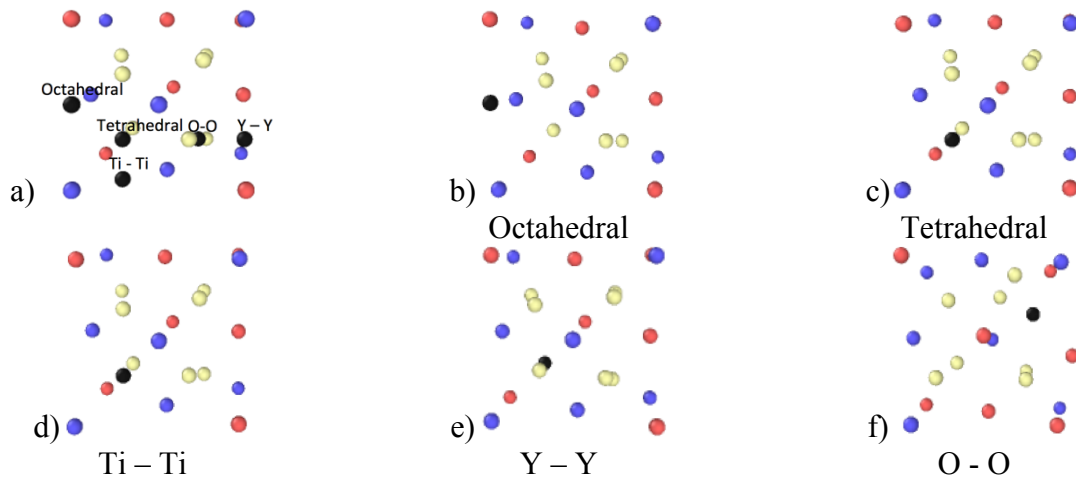
Figure 3.4(a) Bottom 1/8th corner of the Y$_2$Ti$_2$O$_7$ unit cell showing examples of the five unrelaxed interstitial He sites tested. Only the bottom 1/8th corner is shown due to the rotational symmetry of the unit cell, calculations have been performed using the full unit cell. (b-f) Bottom 1/8th corner of fully relaxed (b)octahedral, (c)tetrahedral, (d)Ti-Ti, (e)Y-Y, and (f)O-O He interstitials. Red, blue, yellow and black atoms represent Y, Ti, O and He respectively.

In the fully relaxed Y$_2$Ti$_2$O$_7$ system, the space in which a helium atom can be inserted has been calculated based on the ionic radii of the yttrium, titanium, oxygen and helium atoms and the amount of free volume at any given location in the unit cell. Performing this calculation shows two distinct sites located on the octahedral (i.e. between Y and Ti atoms in (100) directions) and tetrahedral (i.e. located on the O8a vacancy) sites. However, due to the lack of experimental or theoretical information on the radius of the helium atom and some overlap with intermediate locations in the volume calculations performed, helium interstitials have been tested at three additional sites located at the midpoint between two yttrium atoms, the midpoint between two titanium atoms and the midpoint between two oxygen atoms each in (110) directions, as can be seen in Figure 3.4. The bond angles and distances indicate that the symmetry of long range interactions throughout the unit cell for all yttrium, titanium and oxygen atoms with respect to the helium interstitial is the same. Calculations have been performed for all such sites throughout the unit cell verifying that the ground state energies are the same. Because the symmetry is the same

12

throughout the cell, only the bottom $1/8^{th}$ corner has been shown to represent the interstitial positions, although simulations have been performed using the entire 88 atom unit cell.

3.5   Results
3.5.1   *Influence of helium on the lattice and solution energies*

Upon full relaxation of the $Y_2Ti_2O_7$ unit cell containing a single helium interstitial, the surrounding atoms generally displace away from the helium interstitial, although for different configurations, the magnitude of this displacement varies. The structural changes upon full relaxation can be summarized as follows:

- The helium atom on the octahedral and tetrahedral interstitial locations displace by the least magnitudes. The structural stability of $Y_2Ti_2O_7$ in this configuration is indicated by the minimal displacement of the surrounding atoms and the low displacement of the interstitial upon full relaxation.

- The helium interstitial at the midpoint of two titanium atoms (in (110) directions) relaxes into the tetrahedral location with nearly the same energy and volume change and is treated the same as the tetrahedral interstitial.

- The helium interstitial at the midpoint of two yttrium atoms (in (110) directions) causes significant distortion to the lattice. The yttrium atoms displace in the direction opposite the helium atom. The O 48f atom neighboring the interstitial displaces to the midpoint of two titanium atoms in the direction of the O 8a vacancy.

- The helium atom at the midpoint of two oxygen atoms (in (110) directions) also causes considerable distortion to the lattice. The interstitial displaces in the direction opposite the oxygen atoms (towards a Y atom), which also have a significant displacement. The yttrium atom is displaced away from the helium atom. This position creates the largest distortion of the surrounding lattice sites.

The relative stability of each helium interstitial site tested has been evaluated by calculating the solution energy as, $E_{sol} = E_{Defect} - (E_{Perfect} + E_{He})$ where E_{Defect}, $E_{Perfect}$ and E_{He} are the ground state energies of the system with an interstitial helium atom present, the perfect lattice and an isolated helium atom respectively. The solution energies for the sites tested, the changes in volume of the unit cell and the displacement of helium atom upon full relaxation are shown in Table 3.2.

Table 3.2 Calculated ground state energy, solution energy, volume and displacement of the interstitial upon full structural relaxation of the $Y_2Ti_2O_7$ lattice.

	Ground State Energy (eV/Atom)	Solution Energy(eV)	Volume (nm^3)	He Displacement (nm)
$Y_2Ti_2O_7$	-9.0752	-	1.05885	-
Octahedral	-9.0654	0.863	1.06611	0.0237
Tetrahedral	-8.9563	1.508	1.0616	0.0099
Y - Y	-8.9553	1.593	1.06614	0.0702
Ti - Ti	-8.9565	1.492	1.06171	0.118
O - O	-8.9676	1.388	1.07378	0.0814

The octahedral interstitial site has the lowest solution energy of 0.863 eV and is the most stable helium interstitial site. The Y-Y interstitial is the least stable with a solution energy of 1.593 eV. The displacement of the helium interstitial and the change in volume upon full relaxation is noted to observe the stability of the initial site, as well as to relate the displacement of constituent atoms to the structural changes of the unit cell. The tetrahedral site has the lowest displacement upon full relaxation of .0099 nm. In all cases, the unit cell expands volumetrically with the tetrahedral site causing the smallest increase in volume and the site between two O atoms, the largest. The variation in the volume of the fully relaxed cells is caused by the difference in the displacement of constituent atoms from their equilibrium sites, resulting in changes of bond angles and distances when a helium interstitial is present.

3.5.2 *Influence of helium on electronic structure*

The interaction of helium with the oxide has been investigated using the electronic structure calculations from VASP. Bader analysis [36,37,38] (Table 3.3), the change in partial density of states (PDOS) (perfect PDOS – defect PDOS), and the charge density and electron localization function (ELF) have given valuable insight to the interaction of a helium interstitial with the oxide. The ELF ranges from 0 to 1 and coupled with the charge density can be used to interpret the bonding in the oxide. High ELF and charge density values correspond to inert cores and covalent bonds [33]. The PDOS, ELF and charge density for the pure system is shown in Figure 3.5 and shows a stronger hybridization of (Ti-3d, O-2p) than (Y-4d, O-2p) as found previously by Jiang et al [33]. Figure 3.6 (a-d) shows the change in PDOS between pure $Y_2Ti_2O_7$ and $Y_2Ti_2O_7$+He. Negative values indicate an increase, positive values indicate a decrease and zero indicates the same number of states at a given energy when compared with the pure system. While the (Ti-3d, O-2p) hybridization remains stronger than the (Y-4d, O-2p), the increased number of valence s- and d-states from Y and Ti and p-states of O indicate that changes have occurred in the Y-O and Ti-O bonds.
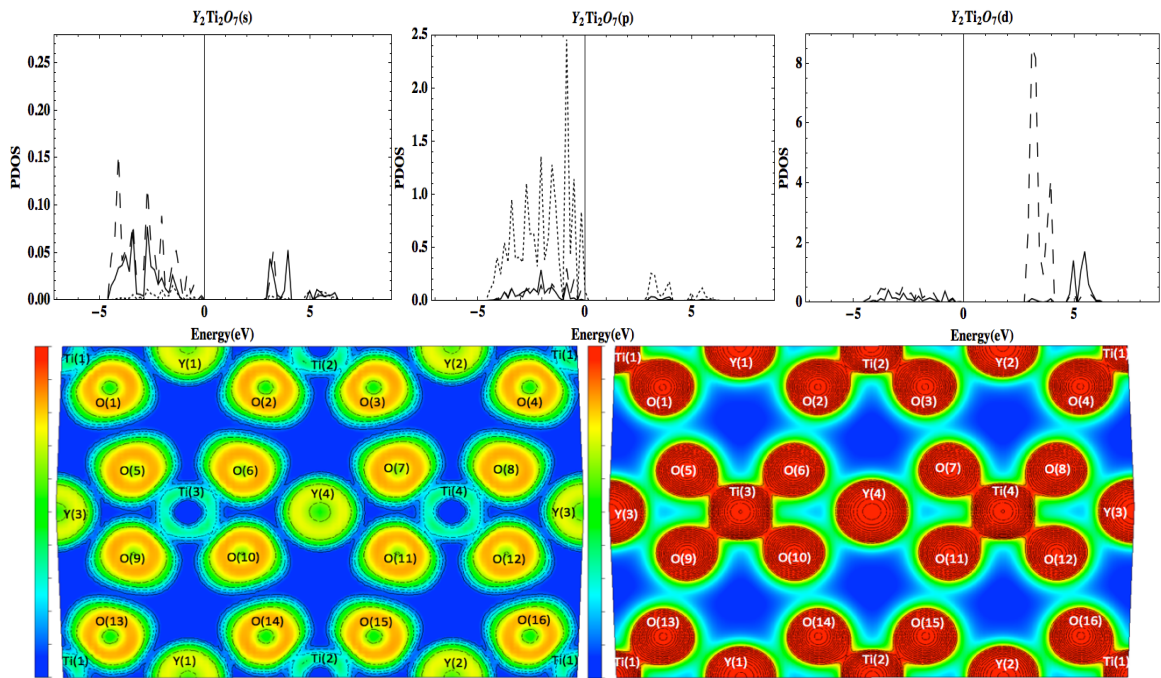
Figure 3.5 PDOS (Y – Solid, Ti – Dashed, O – Dotted), ELF (left) and charge density (Right) for pure $Y_2Ti_2O_7$.

a)

b)
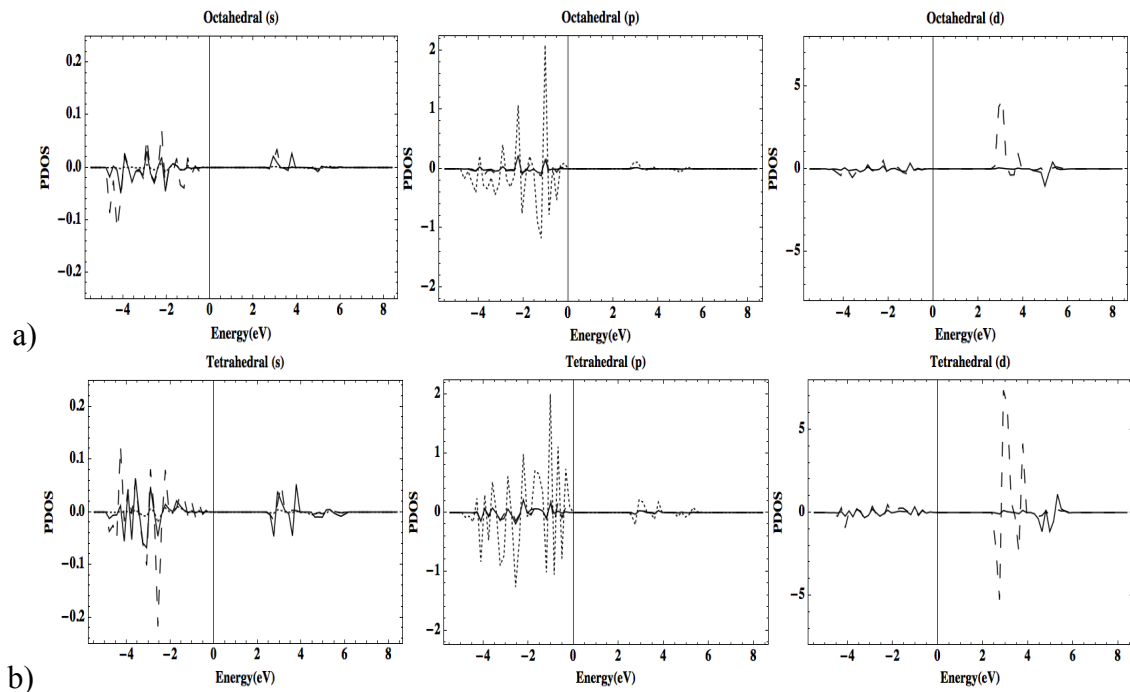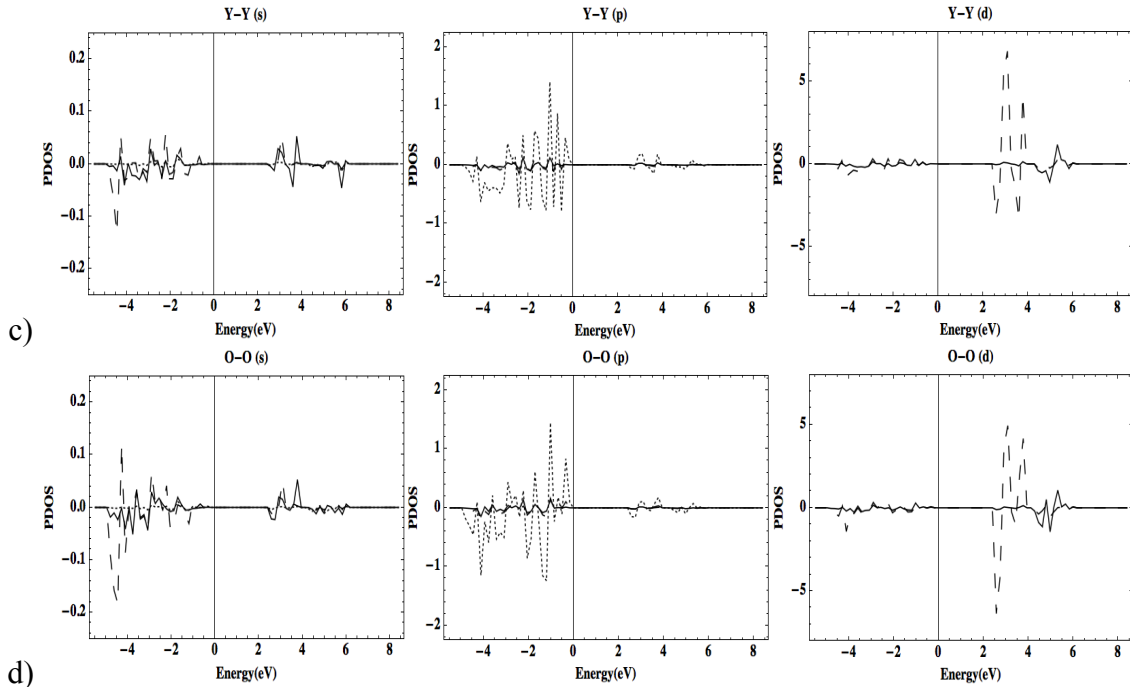
Figure 3.6 (a-d) Change in PDOS for each helium interstitial configuration (Y – Solid, Ti – Dashed, O – Dotted).

The charge density and the ELF reflect the change in bonding for each interstitial configuration. Neighboring the helium interstitial in a given configuration, the Ti-O and Y-O bonds are seen to either increase or decrease in covalency. The changes to the bonds can be largely attributed to the change in bond angles and distances resulting from the deformation of the unit cell. The distortion of the oxygen atoms in the ELF indicates that there is a direct interaction between helium and the neighboring oxygen atoms resembling electron-electron repulsion. The balance of the electron-electron repulsion between helium and surrounding oxygen atoms is responsible for the deformation of the unit cell as the helium atom reaches its lowest energy position.

17
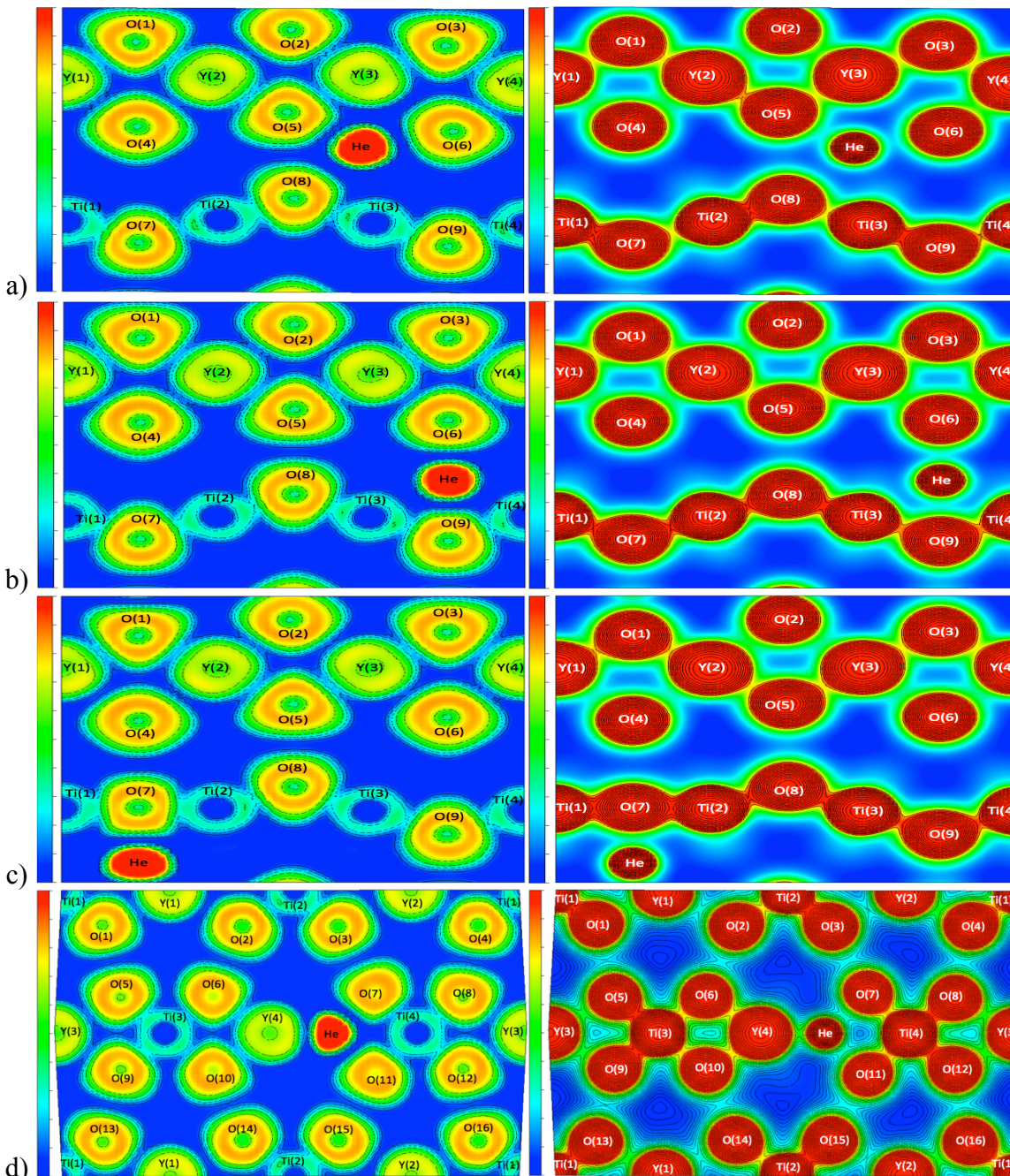
Figure 3.7 ELF (left) and charge density (right) plots for a) octahedral b) tetrahedral c) Y-Y and d) O-O interstitial locations.

Bader analysis (Table 3.3) has been used to quantitatively describe the change in the Y-O and Ti-O bonds, as well as the electron-electron repulsion between helium and oxygen. By comparing with Bader analysis performed on the pure system, an increase or decrease in the Bader charge of the Ti^{4+} and Y^{3+} cations indicates that the bond with at least one oxygen atom has become

more covalent or less covalent respectively. Alternatively, an increase or decrease of the Bader

charge of the O^{2-} anions indicates a more ionic or less ionic bond respectively. Figure 3.7b shows

a clear indication that the Ti(3)-O(9) and Ti(4)-O(9) bonds have become less covalent which is

reflected by the increase in the charge of O(9) from 7.2289 to 7.2519 and decrease of charge in

both Ti(3) and Ti(4) from 7.8173 to 7.7947. Similarly, the Bader volume of the O(9) is decreased

from 12888500 to 12625200 pm^3 providing a quantitative description of the observed interaction

between helium and oxygen. A similar result is shown in Figure 3.7c in the Ti(1)-O(7) and Ti(2)-

O(7) cases. However, in this configuration, the charge of O(7) decreases from 7.2289 to 7.0318

and the charge of Ti(1) and Ti(2) increases from 7.8173 to 7.8227 indicating a more covalent bond.

A decrease in the Bader volume of O(7) is also observed from 12888500 to 12134700 pm^3. Similar

changes in Y-O bonds have been observed with the majority of Y-O bonds increasing in covalency

based on the Bader analysis performed.

Table 3.3 Bader volumes(pm^3) and charges (# electrons)

Perfect	Y (Volume)	Y (Charge)		Ti (Volume)	Ti (Charge)		O (Volume)	O (Charge)
Y(1)	12659400	8.779	Ti(1)	7852500	7.8174	O(1)	12888500	7.2289
Y(2)	12659400	8.779	Ti(2)	7852500	7.8174	O(2)	12879400	7.2285
Y(3)	12659400	8.779	Ti(3)	7852500	7.8174	O(3)	12888500	7.2289
Y(4)	12659400	8.779	Ti(4)	7852500	7.8174	O(4)	12879400	7.2285
						O(5)	12879400	7.2285
						O(6)	12888500	7.2289
						O(7)	12879400	7.2285
						O(8)	12883900	7.2287
						O(9)	12883900	7.2287
						O(10)	12879400	7.2285
						O(11)	12888500	7.2289
						O(12)	12879400	7.2285
						O(13)	12879400	7.2285
						O(14)	12888500	7.2289
						O(15)	12879400	7.2285
						O(16)	12888500	7.2289
Octahedral								
Y(1)	12760600	8.7984	Ti(1)	7434300	7.7921	O(1)	14146300	7.4136
Y(2)	12672900	8.8068	Ti(2)	7479900	7.7967	O(2)	12737400	7.2456
Y(3)	12809500	8.8037	Ti(3)	7405200	7.7908	O(3)	14280000	7.4114
Y(4)	12841000	8.8016	Ti(4)	7662000	7.801	O(4)	13116700	7.2395
						O(5)	13219700	7.3986
						O(6)	12535000	7.2055
						O(7)	13130000	7.2328
						O(8)	13411400	7.2209
						O(9)	12894000	7.241
Tetrahedral								

Y(1)	12736100	8.7986	Ti(1)	7490100	7.7928	O(1)	14072200	7.3939
Y(2)	12736100	8.7986	Ti(2)	7487000	7.7927	O(2)	12996600	7.2315
Y(3)	12755100	8.8029	Ti(3)	7536200	7.7947	O(3)	13904300	7.3974
Y(4)	12755100	8.8029	Ti(4)	7536200	7.7947	O(4)	12915000	7.2317
						O(5)	14104100	7.3966
						O(6)	12625200	7.2519
						O(7)	12915000	7.2317
						O(8)	12875100	7.2254
						O(9)	12625200	7.2519
Y-Y								
Y(1)	12854600	8.8046	Ti(1)	7460700	7.8227	O(1)	13924400	7.41
Y(2)	12854600	8.8046	Ti(2)	7460700	7.8227	O(2)	13054500	7.2369
Y(3)	12879400	8.8031	Ti(3)	7420800	7.7884	O(3)	14121700	7.4043
Y(4)	12879400	8.8031	Ti(4)	7420800	7.7884	O(4)	13020700	7.2654
						O(5)	14145400	7.41
						O(6)	13157600	7.2324
						O(7)	12134700	7.0318
						O(8)	12745600	7.2376
						O(9)	12861400	7.2572
O-O								
Y(1)	12912900	8.7956	Ti(1)	7405600	7.7844	O(1)	13232000	7.2264
Y(2)	12783400	8.7923	Ti(2)	7366800	7.7919	O(2)	13194700	7.2259
Y(3)	12533300	8.7949	Ti(3)	7207900	7.807	O(3)	13330800	7.228
Y(4)	12341200	8.8428	Ti(4)	7261400	7.8001	O(4)	13003400	7.25
						O(5)	12876700	7.2404
						O(6)	12941000	7.2481
						O(7)	12481100	7.1553
						O(8)	12728900	7.2481
						O(9)	12876700	7.2404
						O(10)	12941000	7.2481
						O(11)	12481100	7.1553
						O(12)	12728900	7.2481
						O(13)	13232000	7.2264
						O(14)	13194700	7.2259
						O(15)	13330800	7.228
						O(16)	13003400	7.25

The most significant changes appear in the Ti-O bonds and are very quantitatively clear in the Bader analysis performed for tetrahedral and Y-Y interstitial configurations. However, in the octahedral and O-O configurations, the effects are not as symmetric. For example, in the octahedral configuration, the Ti(3)-O(8) bond decreases in covalency while the Ti(2)-O(8) bond increases in covalency as shown in the charge density in Figure 3.7a. The helium interstitial in this case has caused O(8) to displace towards Ti(2) decreasing the covalency of the Ti(3)-O(8) bond and increasing the covalency of the Ti(2)-O(8) bond. Consequently, the Bader charge of titanium and oxygen atoms is balanced between the changing of each of the Ti-O bonds. A similar case is observed in the O-O configuration shown in Figure 3.7d.

3.6   Discussion

Due to the large volume of free space and the resulting minimized interaction of the helium interstitial with the neighboring oxygen atoms, the octahedral and tetrahedral locations cause the least deformation of the unit cell. This indicates that the structural stability of the unit cell is not largely compromised by the interstitial in these locations. However, these two configurations are on opposite ends of the solution energy range. This can be attributed to both the structural and electronic properties observed. Figure 3.6 (a-d) indicates that the bonds which are most affected by the presence of the helium interstitial are the Ti-O bonds due to the significant changes in the Ti s- and d- and O p-states. The tetrahedral interstitial is neighbored by six oxygen atoms each equidistant, at right angles and bonded to titanium. It is apparent that the helium atom is able to remain in the center of the neighboring oxygen atoms, finding an equilibrium position based on the equivalent repulsion coming from each oxygen atom. The interaction of helium is equivalently distributed between the surrounding oxygen and affects the degree of covalency of the Ti-O bonds equally. Similarly, the tetrahedral interstitial is located on the O 8a vacancy which is essential at equilibrium for the stability of the $Y_2Ti_2O_7$ structure. This results in an increase of the local electronic charge density on the vacancy. An interstitial on the octahedral site is neighbored by eight oxygen atoms of varying distance and angle each of which are bonded to either titanium or yttrium. Thus, the octahedral interstitial does not as significantly affect the covalency of as many Ti-O bonds.

The much less stable Y-Y and O-O interstitials result in a large distortion of the unit cell. In each of these cases, the bond distances and angles are significantly changed by comparison to the octahedral and tetrahedral configurations. In the Y-Y case, the bond distance significantly decreases between oxygen and surrounding titanium atoms. Bader analysis and the ELF show Ti-

O bonds becoming more covalent in this case. The decreased stability of these interstitial locations can be largely attributed to the deformation of the unit cell.

It has been theorized that the minimization of the growth of helium bubbles nucleating on nanoclusters in nanostructured ferritic alloys is a result of strong interactions of helium atoms with vacancies and with vacancy – oxygen complexes associated with the nanoclusters [39]. It has been found that the helium has a significant interaction with the neighboring oxygen atoms in each configuration displayed by the ELF, charge density, and Bader analysis performed. Similarly, the tetrahedral helium interstitial displaces very little from the vacant O 8a site upon full relaxation. Although the solution energy is not the lowest in this configuration, the minimal displacement is an indication of a strong interaction of the helium atom with the vacancy.

The distinct distortion of the oxygen orbitals shown in Figure 3.7 (a-d) is proposed to result from electron – electron repulsion between the full He 1s shell and oxygen. The distortion of the oxygen atom is most significant likely because the ionic radius is the largest in $Y_2Ti_2O_7$. Consequently, in each fully relaxed case, the helium is neighbored most directly by oxygen atoms.

3.7   Conclusions

The stability of five distinct helium interstitial positions has been evaluated using density functional theory. Of the five positions tested, only four are distinct; the octahedral, tetrahedral, Y-Y and O-O. The electron localization functions, charge densities, change in partial density of states and Bader analysis have given insight to the interaction of the helium atom with the neighboring atoms in the lattice, as well as the effects of the helium interstitial on the bonding of the constituent atoms. The titanium s- and d-states and O p-states were found to be the most significantly affected by the presence of interstitial helium. This consequence arises from two apparent causes; the distortion of the oxygen orbitals resulting in changes to the Ti – O bonding characteristics, and the resulting deformation of the crystal lattice. The octahedral interstitial

location has the lowest solution energy and is the most stable and the Y-Y interstitial site is the least stable. The energetic results of this study will further the development of multi-scale models for the management of helium in nanostructured ferritic alloys.

3.8   Acknowledgements

References

[1] G.R. Odette, M.J. Alinger and B.D. Wirth, Annu. Rev. Mater. Res. **38**, 471 (2008).

[2] J.H. Schneibel, M. Heilmaier, W. Blum, G. Hasemann and T. Shanmugasundaram, Acta Mat. **59**, 1300 (2011).

[3] R.L. Klueh, P.J. Maziasz, I.S. Kim, L. Heatherly, D.T. Hoelzer, N. Hashimoto, E.A. Kenik and K. Miyahara, J. Nucl. Mater. **307-311**, 773 (2002).

[4] D.A. McClintock, D.T. Hoelzer, M.A. Sokolov and R.K. Nanstad, J. Nucl. Mater. **386-388**, 307 (2009).

[5] H. Trinkaus and B.N. Singh, J. Nucl. Mater. **323**, 229 (2003).

[6] C.C. Fu and F. Willaime, Phys. Rev. B **72**, 064117 (2005).

[7] P. Erhart, J. Appl. Phys. **111**, 113502 (2012).

[8] K. Morishita, R. Sugano, B.D. Wirth, and T. Diaz de la Rubia, Nucl. Instrum. Methods Phys. Res. B **202**, 76 (2003).

[9] T. Yamamoto, G.R. Odette, R.J.Kurtz and B.D. Wirth, Fusion Reactor Materials Program DOE/ER-0313/49, 73 (2010).

[10] H.L. Heinisch, F. Gao and R.J. Kurtz, Journal of ASTM International **4**, (2007).

[11] J.N. Al-Hajji and N.M. Ghoniem, Acta Metall. **35**, 1067 (1987).

[12] P.D. Edmondson, C.M. Parish, Y. Zhang, A. Hallen and M.K. Miller, J. Nucl. Mater. **434**, 210 (2013).

[13] T. Ishizaki, Q. Xu, T. Yoshiie, S. Nagata and T. Troev, J. Nucl. Mater. **307-311**, 961 (2002).

[14] S.M Hafez Haghighat, G. Lucas and R. Schaublin, EPL **85**, 60008 (2009).

[15] A.A. Sagues, H. Schroeder, W. Kesternich and H. Ullmaier, J. Nucl. Mater. **78**, 289 (1978).

[16] H. Trinkaus, J. Nucl. Mater. **118**, 39 (1983).

[17] D.N. Braski, H. Schroeder and H. Ullmaier, J. Nucl. Mater. **83**, 265 (1979).

[18] G.R. Odette, P. Miao, D.J. Edwards, T. Yamamoto, R.J. Kurtz and H. Tanigawa, J. Nucl. Mater. **417**, 1001 (2011).

[19] P.D. Edmondson, C.M. Parish, Y. Zhang, A. Hallen and M.K. Miller, Scripta Mat. **65**, 731 (2011).

[20] G. Kresse and J. Hafner, Phys. Rev. B **47**, 558 (1993).

[21] G. Kresse and J. Hafner, Phys. Rev. B **49**, 14251 (1994).

[22] G. Kresse and J. Furthmuller, Comput. Mat. Sci. **6**, 15 (1996).

[23] G. Kresse and J. Furthmuller, Phys. Rev. B **54**, 11169, (1996).

[24] P.E. Blochl, Phys. Rev. B **50**, 17953 (1994).

[25] G. Kresse and D. Joubert, Phys. Rev. B **59**, 1758 (1999).

[26] J.P. Perdew, K. Burke and M. Ernzerhof, Phys. Rev. Lett. **77**, 3865 (1996).

[27] J.P. Perdew, K. Burke and M. Ernzerhof, Phys. Rev. Lett. **78**, 1396 (1997).

[28] T. van Mourik and J.H. van Lenthe, J. Chem. Phys. **102**, 7479 (1995).

[29] D.M. Ceperley and H. Partridge, J. Chem. Phys. **84**, 821 (1986).

[30] J.P. Perdew, J.A. Chevary, S.H. Vosko, K.A. Jackson, M.R. Pederson, D.J. Singh, and C. Fiolhais. Phys. Rev. B, 46:6671, 1992.

[31]J.P. Perdew, J.A. Chevary, S.H. Vosko, K.A. Jackson, M.R. Pederson, D.J. Singh, and C. Fiolhais. Phys. Rev. B, 48:4978, 1993.

[32] R. Terki, G. Bertrand, H. Aourag and C. Coddet, Physica B **392**, 341 (2007).

[33] Y. Jiang, J.R. Smith and G.R. Odette, Acta Mat. **58**, 1536 (2010).

[34] M.A. Subramanian, G. Aravamudan and G.V. Subba Rao, Prog. Sol. St. Chem. **15**, 55 (1983).

[35] J. Lian, J. Chen, L.M. Wang, R.C. Ewing, J.M. Farmer, L.A. Boatner and K.B. Helean, Phys. Rev. B **68**, 134107 (2003).

[36] W. Tang, E. Sanville and G. Henkelman, Phys.: Condens. Matter **21**, 084204 (2009).

[37] E. Sanville, S. D. Kenny, R. Smith and G. Henkelman, J. Comp. Chem. **28**, 899-908 (2007).

[38] G. Henkelman, A. Arnaldsson and H. Jónsson, Comput. Mater. Sci. **36**, 254-360 (2006).

[39] P.D. Edmondson, C.M. Parish, Q. Li and M.K. Miller, J. Nucl. Mater. Accepted Manuscript (12 October 2013).

4.   First-principles investigation of helium in Y_2O_3

4.1   Abstract

Density functional theory has been used to investigate the relative stability, migration barriers and potential energy surfaces of helium in Y_2O_3 in order to provide insight to the trapping mechanisms of helium at the oxide-Fe interface in nanostructured ferritic alloys. The helium interstitial sites have been located and their relative stability in Y_2O_3 is determined from the solution energy. The interaction of helium with the oxide has been investigated using the charge density and electron localization function. The migration barriers have been calculated and further investigated using potential energy surfaces computed on various lattice planes. Helium trapping has been attributed to very large diffusion barrier energies, especially close to oxygen atoms.

4.2   Authors and Affiliations

T. Danielson[1], E. Tea[2] and C. Hin[1,2]

[1]Department of Materials Science and Engineering

[2]Department of Mechanical Engineering

Virginia Polytechnic Institute and State University, 635 Prices Fork Road, Blacksburg, VA, 24060, USA

Corresponding Author Email: thomasd1@vt.edu

4.3   Introduction

Nanostructured ferritic alloys (NFAs) are a class of oxide dispersion strengthened (ODS) alloys that have the ability to withstand high temperatures, high pressures, high neutron fluence and high concentrations of transmutation product helium, making them strong material candidates for first wall and structural components of the next generation of nuclear reactors [1-4]. The ability

to withstand the harsh reactor conditions arises from the dispersion of a high number density of complex oxide nanoclusters (NCs) evenly dispersed throughout a BCC Fe matrix. The oxide NCs are most commonly comprised of Y_2O_3, $Y_2Ti_2O_7$, Y_2TiO_5 and other non-stoichiometric Y-Ti-O compounds [1]. The NCs have been shown to have exceptional stability at elevated temperature and under large neutron doses and serve to pin dislocations that act as annihilation sites for point defects created during irradiation [1,5-7]. The NCs also act as trapping sites for helium, a phenomenon that has gained widespread interest in recent years and for which no complete theoretical understanding exists [1,8-10].

The formation of helium clusters in NFAs under irradiation is energetically favorable due to the extremely migration barriers in the BCC iron matrix, high vacancy concentrations that stabilize the clusters, and the positive binding energy of individual helium atoms to one another [11-16]. As individual atoms and small clusters diffuse through the iron matrix and along dislocation networks, they preferentially nucleate into larger bubbles on grain boundaries, dislocations and voids [14,17]. The high-operating temperature of nuclear reactors causes helium bubbles to become highly pressurized resulting in deformation to the surrounding lattice and ultimately, cracking and intergranular fracture due to helium embrittlement [18,19]. Thus, the management of helium and the prevention of pressurized bubble induced lattice deformation are of critical importance.

Nanostructured ferritic alloys offer a promising solution for managing high concentrations of helium due to the high number density of complex oxide NCs that act as trapping sites for helium [1]. Helium implanter transmission electron microscopy studies of NFAs have shown the surface of NCs nearly completely covered by helium bubbles, where greater than 50% of the bubbles in the material are located on NCs [20-22]. Similarly, trapped helium bubbles are

preferential sites for helium atoms diffusing through the matrix and consequently, the trapping of helium bubbles at NCs serves to even further reduce the number of helium atoms that can reach grain boundaries and voids. Thus, it is clear that NCs are very effective at mitigating the risk of helium embrittlement. While experimental evidence only shows the existence of bubbles at the surface of NCs, it is likely that isolated helium atoms may be located within the surface layers of the oxide NCs prior to bubble nucleation as the migration barrier of helium through iron is very low (~0.07 eV) and the formation energy of interstitial helium in BCC iron is high (> 4 eV) [11]. Likewise, studying the interactions of helium within the oxide may provide insight as to what interactions occur between the oxide and helium and ultimately, why helium bubble formation is favorable at the oxide-iron interface.

Improving the prevention of helium embrittlement in reactor environments relies on the development of multi-scale models that incorporate the thermodynamic and kinetic parameters necessary to accurately describe the transport and fate of helium in NFAs. The parameterization of these models can be achieved accurately and efficiently using first-principles calculations, simultaneously gaining insight into the quantum mechanical interaction of helium with the oxides. The focus of this study is to determine the helium interstitial sites and their relative stability in Y_2O_3, one of the most common oxide NC systems in NFAs [23]. Likewise, the effects of helium on the electronic structure of Y_2O_3 may shed light on the trapping mechanisms of the oxides. The results will be a valuable resource for the development of more complex models explaining the evolution of a material in a reactor environment and for the prevention of helium embrittlement.

In the next section, the computational setup and structural parameters are presented. Section 3 contains results obtained on the stability of helium in different locations, the electronic structure, the migration barriers and the potential energy surfaces. Finally, a discussion of the

results and the implications they may have on the trapping effects of helium bubbles at NCs is presented in section 4.

4.4   Computational Methods

DFT calculations have been performed as implemented in the Vienna *ab initio* Simulation Package (VASP) [24-27] using the projector-augmented wave (PAW) method [28,29]. The 4s and 4p, and 2s electrons have been treated as valence electrons for Y and O respectively. The generalized gradient approximation (GGA) from Perdew, Berke and Ernzerhoff (PBE) [30,31] has been used for exchange and correlation. Testing the convergence of energy with respect to K-points and plane-wave energy cutoff has shown that a 4x4x4 Monkhorst-Pack K-point mesh and a plane-wave energy cutoff of 600 eV is sufficient for calculations of the ground state properties of the defective system. For each calculation, one fully periodic 80-atom unit cell has been used, where the ions, cell volume and cell shape are each relaxed to their ground state.

Y_2O_3 belongs to the space group Ia-3 and has the bixbyite-type structure (Figure 4.1), where the Y^{3+} cations occupy the 8b (¼,¼,¼) and 24d (u,0,¼) Wyckoff positions and the O^{2-} anions occupy the 48e general positions. The structure is often related to that of the CaF_2 structure where the A^{2+} eight-fold coordination is reduced to a six-fold coordination for the A^{3+} cations in Y_2O_3 [33]. The structure of Y_2O_3 is defined by four structural parameters; one defining the position of the Y^{3+} cations occupying the 24d positions (u) and three defining the positions of the O^{2-} cations (x_o, y_o, z_o) . Table 4.1 shows the structural parameters of the current work compared to existing DFT and experimental calculations and excellent agreement is found.

Table 4.1 Structural parameters for bulk Y_2O_3 in Angstroms

	GGA	GGA[a]	Expt.[b]
$a(\mathring{A})$	10.709	10.7	10.602
u	-0.0327	-0.0327	-0.0327
x_o	0.3908	0.3908	0.3907
y_o	0.1516	0.1516	0.152
z_o	0.3819	0.3799	0.3804

[a]Ref. [32]
[b]Ref. [33]
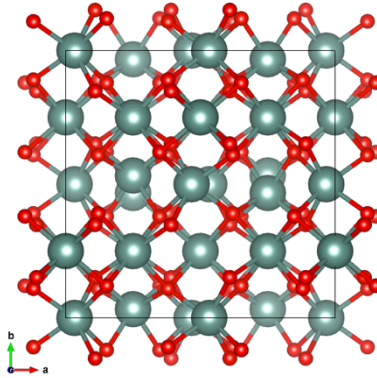
Figure 4.1 Y_2O_3 bixbyite structure. Red and green atoms are O and Y respectively.

The positions in the fully relaxed Y_2O_3 unit cell in which helium interstitials can exist have been localized by performing a calculation of the amount of free volume in the unit cell based on the ionic radii of yttrium, oxygen and helium. Performing this calculation shows that the extent of the free volume in the Y_2O_3 unit cell is quite large and helium interstitials can fit between all oxygen atoms (i.e. between two oxygen atoms in (110) directions) and all yttrium atoms (i.e. between two yttrium atoms in (110) directions). In the Y_2O_3 unit cell, there exists three unique types of distorted octahedra in which a helium interstitial can be located. The first (Oct Y1) is located at the center of four Y 8b sites and two Y 24d sites, the second (Oct Y2) is between six Y 24d sites and the third (Oct O) is at the center of six O 48e sites. These octahedra represent the largest volume of free space in the unit cell. Thus, ground state calculations have been performed for each octahedron (Figure 4.2) and in between all Y pairs and O pairs in the unit cell. Full

relaxation of the structure will ensure that the helium interstitial is relaxed to its most stable position.
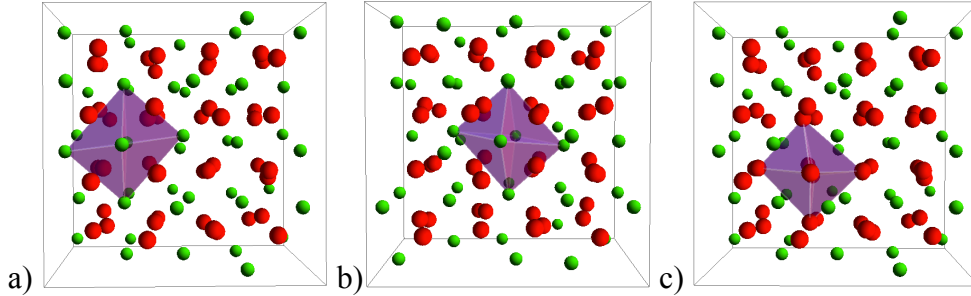
Figure 4.2 Three distinct distorted octahedra in the Y_2O_3 unit cell: a) Oct Y1, b) Oct Y2 and c) Oct O. Red and green atoms are oxygen and yttrium respectively.

4.5   Results

4.5.1   Relative stability of interstitial sites

Upon full relaxation of the Y_2O_3+He system, the helium interstitial relaxes to the nearest octahedron shown in Figure 4.2. The distortion of the lattice is minimal in each case indicating that the Y_2O_3 system is reasonably stable containing a helium interstitial. The relative stability of each interstitial location has been evaluated by calculating the solution energy as,

$$E_{Sol} = E_{Defect} - (E_{Perfect} + E_{He}) \tag{1}$$

where, E_{Defect}, $E_{Perfect}$ and E_{He} are the ground state energies of Y_2O_3+He, pure Y_2O_3 and an isolated helium atom respectively. The results for the solution energy and the volume change upon relaxation are shown in Table 4.2.

Table 4.2 Calculated solution energies and volume change for each fully relaxed interstitial configuration.

	Solution Energy (eV)	Volume Change (%)
Oct Y1	0.895	0.18
Oct Y2	0.620	0.13
Oct O	0.482	0.11

Oct O is the most stable interstitial position with a solution energy of 0.482 eV and Oct Y1 is the least stable interstitial with a solution energy of 0.895 eV. Each of these positions has the lowest and highest change in volume respectively. The solution energy varies positively with the

31

volume change, suggesting that bond stretching in the host matrix largely affects the interstitial stability.

4.5.2   Influence of helium interstitials on the electronic structure

The electronic structure of the pure and defect systems have been investigated using the charge density, differential charge density and electron localization function (ELF) High values for the ELF and charge density indicate inert cores and covalent bonds. The ELF and charge density for Y_2O_3 are shown in Figure 4.3. The Y-O bonds are shown to be mostly ionic which is consistent with previous studies of Y_2O_3 [37,38].
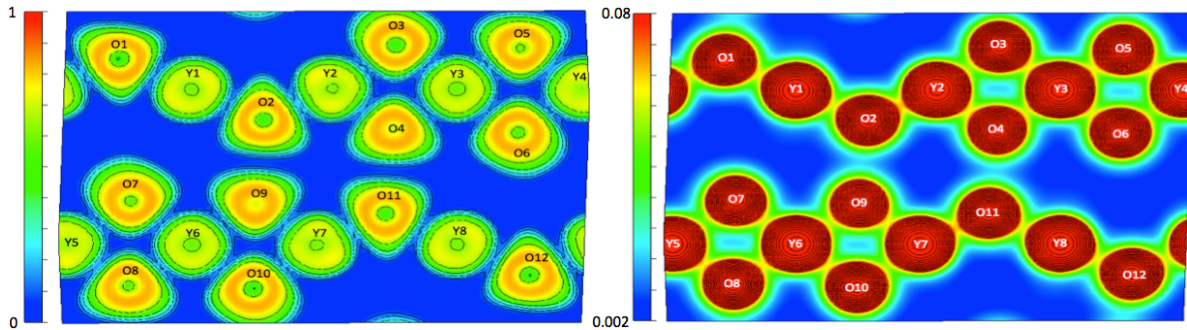
Figure 4.3 ELF (left) and charge density (right) in the (101) plane of pure Y_2O_3.

The differential charge density has been calculated as:

$$\rho^{Diff} = \rho^{Defect} - \rho^{Perfect} - \rho^{He} \tag{2}$$

Where, ρ^{Defect}, $\rho^{Perfect}$ and ρ^{He} are the charge densities of the defect cell, the defect cell with the helium atom removed and the helium atom with the Y_2O_3 lattice removed. The charge density and differential charge density have been compared on the same scale in Figure 4.4. The differential charge density has been investigated on a scale that relates to the amount of charge redistribution that results from Y-O bond formation within the Y_2O_3 lattice. This charge redistribution has been determined by calculating the differential charge density for Y and O vacancies within the Y_2O_3 lattice. This provides a benchmark for the scale on which to investigate the nature of electronic interaction between helium and the neighboring O atoms. It is shown that

32

no charge transfer occurs which is expected due to the inert nature of the helium interstitial. This clearly shows that no chemical interaction is occurring between the neighboring atoms and the helium interstitial. Moreover, analysis of the Projected Density of States reveals that the helium states are dispersionless in reciprocal space, showing their localized nature.
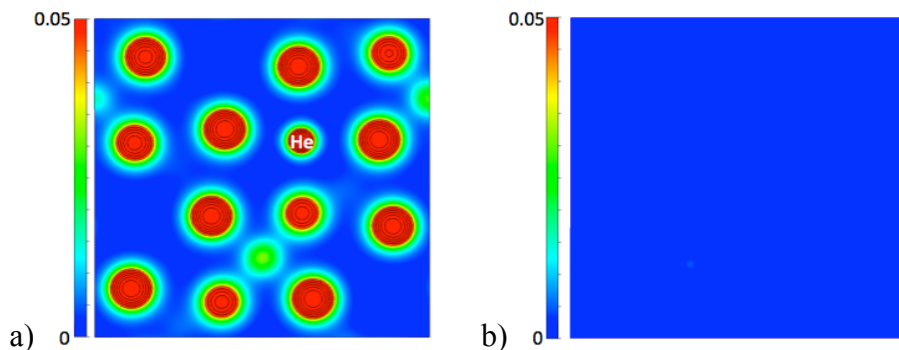
Figure 4.4 a) Charge Density and b) Differential Charge Density of Y_2O_3 with a single helium atom located on the Oct O site shown in the (100) plane.

Figure 4.5 compares the electron localization function of the pure Y_2O_3 system and Y_2O_3 with a single helium interstitial located on the Oct O site. The neighboring oxygen electron clouds are shown to flatten in the presence of the helium interstitial. This interaction is indicative of electron – electron repulsion between the inert helium atom and the neighboring O atoms. A similar result is found for each interstitial location.
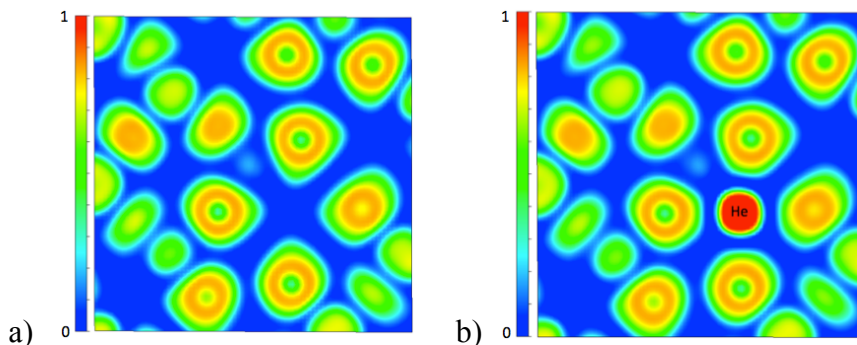
Figure 4.5 Electron localization function for a) pure Y_2O_3 and b) Y_2O_3 with a single helium interstitial located on the Oct O position. Electron localization functions are shown in a (100) plane.

4.5.3   Migration Barriers and Potential Energy Surfaces

The energy barrier for migration of helium between each of the interstitial positions has

been calculated using the Nudged Elastic Band method [34-36].   Migration paths between

interstitial locations have been tested using a sequence of ten images where the initial and final

interstitial locations can be reached without passing through any other interstitial location. The

lowest diffusion barrier is found to be on the path from the Oct Y2 to the Oct O position with a

barrier of 0.227 eV (Figure 4.6). Migration barriers from Oct Y1 to Oct O and Oct Y1 to Oct Y2

have also been tested and are 0.429 eV and 2.465 eV respectively. Along each migration path, it

is necessary for the helium interstitial to displace the nearest neighboring oxygen atom in order to

migrate from the initial to final location. This effect is most dramatically seen in the case where

helium migrates from Oct Y1 to Oct Y2, hence the very large energy barrier.
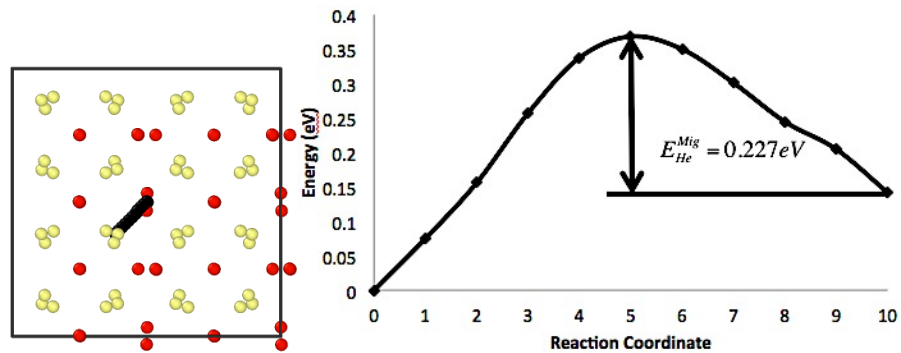
Figure 4.6 Migration path and barrier from Oct O to Oct Y2 (red, yellow and black spheres represent Y, O and He respectively).

In order to further investigate helium migration in Y_2O_3, helium potential energy surfaces

have been computed by calculating the potential energy surfaces, centered on the most stable He

octahedral site, i.e., the Oct O sites. Helium potential energy surfaces have been calculated by

relaxing the positions of the nearest neighbor atoms of the host matrix while keeping the helium

atom position fixed. The nearest neighbor atoms are defined as those remaining in the sphere of a

half unit cell radius, centered on the fixed helium position. Consequently, He atoms are not allowed

to drift back to their stable octahedral position while atoms of the host matrix shift. By repeating this calculation for all helium positions on a regular 2D mesh, different lattice planes have been mapped, including (110), (111), and (001) planes at different elevations z in reduced coordinates. This allow us to exhibit the diffusion barriers of all stable sites.

Potential energy surfaces are shown in Figure 4.7 where the Oct O helium interstitial has been used as the scale reference. Mapping of the (110) and (111) planes reveal the hollow nature of Y_2O_3, and confirm the NEB lowest diffusion energy path from Oct Y2 to Oct O sites. Mapping of the (001) planes centered on the different interstitial sites (Oct O for z=0.35, Oct Y2 for z=0.50) displays high energy barriers (>2eV) irrespective of the diffusion direction. Overall, the helium potential energy surfaces exhibit deep wells at the different stable interstitial sites, demonstrating the trapping ability of Y_2O_3.

A deeper analysis of the potential energy surfaces shows that the diffusion barrier spatial width correlates with the host atoms atomic radii. The spatially larger barriers around Y atoms are shown in the (001) plane at z=0.50. The spatially thinner barriers around O atoms are shown in the (001) plane at z=0.35. Barriers originating from O atoms exhibit higher peak energies, suggesting that the oxygen sub lattice is more rigid than the yttrium one. The potential energy is relatively small in the free volume region containing and connecting the different stable interstitial sites, as seen on the (110) and (111) planes. This depicts the steric nature of helium diffusion in Y_2O_3.
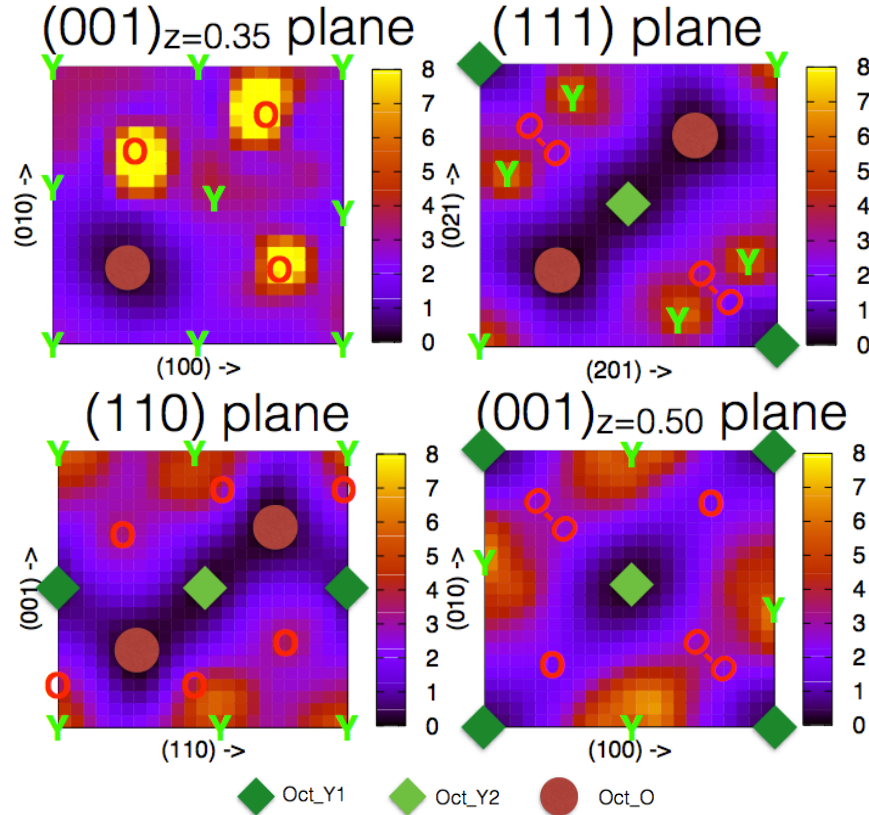
Figure 4.7 Potential energy surfaces drawn on different planes of the Y_2O_3 lattice. Atoms close to or on the investigated planes are indicated as well as stable interstitial positions.

4.6   Discussion

A recent study has indicated that the interaction between helium and the constituent oxygen atoms of the oxide nanoclusters is chemical in nature. However, based on our results showing localization of He electrons, and confirmed by no qualitative electron delocalization in projected density of states, no chemical interaction is found in the current work and the He electrons are shown to be highly localized in all interstitial configurations [40] The interaction between the inert helium interstitial and the constituent oxygen atoms is electron-electron repulsion, thus the stability of the interstitial increases with increasing interstitial volume. No significant changes were observed in the bonds between atoms within the oxide, indicating that the stability of the helium interstitial depends on the bond stretching as volumetric expansion occurs, and not on new bond formation. Compared to helium interstitial in $Y_2Ti_2O_7$, displacement of the constituent atoms in

Y_2O_3 is quite negligible, yielding more stability for helium interstitials in Y_2O_3, thanks to the large amount of free volume in the unit cell [41]. The trapping of helium at oxide nanoclusters is attributed to: (i) the higher stability of interstitials in the oxide than in iron and, (ii) the very large diffusion barriers (especially close to the constituent oxygen atoms) preventing diffusion through the oxide towards the iron host. The correlation between the barriers spatial extent, host atomic radii, and free volume spaces, indicate that helium diffusion in Y_2O_3 is purely steric. The migration barrier of helium through BCC iron (~0.07 eV [11]) is much lower than that in the oxide, thus as the migration path of helium intersects with an oxide nanocluster, it may be more energetically favorable for helium to remain trapped at the surface of the nanocluster and nucleate into a bubble preventing its eventual migration to grain boundaries.

The overall consequence of the free volume contained in the Y_2O_3 unit cell is that the relative stability of helium interstitials in Y_2O_3 is higher than that of BCC iron [11] and $Y_2Ti_2O_7$ [40,41]. Since the solution energies are lower for helium interstitials in Y_2O_3 it may be a reasonable assumption that an increase in the number density of Y_2O_3 oxide nanoclusters in NFAs could potentially lead to an increase in helium trapping, thus reducing the risk of embrittlement.

4.7   Conclusions

Helium interstitials have been localized to three distorted octahedral positions in the Y_2O_3 lattice. The interstitial position located between six 48e oxygen sites is the most stable interstitial site with a solution energy of 0.48 eV because it results in the least volumetric expansion. The relative stability of the helium interstitials has been largely attributed to the minimal stretching of the bonds that occurs upon its introduction. The lower solution energies of helium interstitials in Y_2O_3 indicate that the trapping may be higher in this oxide system than in $Y_2Ti_2O_7$. The electronic structure of the oxide containing helium was investigated and it was found that no charge transfer occurs. Only electron – electron repulsion occurs between the inert helium atom and the

37

constituent oxygen atoms. Helium interstitials are more energetically stable in the oxide than in iron and have a much higher migration barrier through the oxide, thus trapping at the oxide surface is energetically favorable and aids in the prevention of helium embrittlement.

4.8   Acknowledgements

References
[1] G.R. Odette, M.J. Alinger and B.D. Wirth, Annu. Rev. Mater. Res. **38**, 471 (2008).

[2] J.H. Schneibel, M. Heilmaier, W. Blum, G. Hasemann and T. Shanmugasundaram, Acta Mat. **59**, 1300 (2011).

[3] R.L. Klueh, P.J. Maziasz, I.S. Kim, L. Heatherly, D.T. Hoelzer, N. Hashimoto, E.A. Kenik and K. Miyahara, J. Nucl. Mater. **307-311**, 773 (2002).

[4] D.A. McClintock, D.T. Hoelzer, M.A. Sokolov and R.K. Nanstad, J. Nucl. Mater. **386-388**, 307 (2009).

[5] P. Miao, G.R. Odette, T. Yamamoto, M. Alinger and D. Klingensmith, J. Nucl. Mater. **377**, 59-64 (2008).

[6] S. Yamashita, K. Oka, S. Ohnuki, N. Akasaka and S. Ukai, J. Nucl. Mater. **307-311**, 283-288 (2002).

[7] P. Pareige, M.K. Miller, R.E. Stoller, D.T. Hoelzer, E. Cadel and B. Radiguet, J. Nucl. Mater. **360**, 136-142 (2007).

[8] T. Yamamoto, G.R. Odette, P. Miao, D.T. Hoelzer, J. Bentley, N. Hashimoto, H. Tanigawa and R.J. Kurtz, J. Nucl. Mater. **367-370**, 399-410 (2007).

[9] G.R. Odette and D.T. Hoelzer, J. Mater. **62**, 84-92 (2010).

[10] G.R. Odette, P. Miao, D.J. Edwards, T. Yamamoto, R.J. Kurtz and H. Tanigawa, J. Nucl. Mater. **417**, 1001 (2011).

[11] C.C. Fu and F. Willaime, Phys. Rev. B **72**, 064117 (2005).

[12] H. Trinkaus and B.N. Singh, J. Nucl. Mater. **323**, 229 (2003).

[13] P. Erhart, J. Appl. Phys. **111**, 113502 (2012).

[14] T. Yamamoto, G.R. Odette, R.J.Kurtz and B.D. Wirth, Fusion Reactor Materials Program DOE/ER-0313/49, 73 (2010).

[15] K. Morishita, R. Sugano, B.D. Wirth, and T. Diaz de la Rubia, Nucl. Instrum. Methods Phys. Res. B **202**, 76 (2003).

[16] G. Lucas and R. Schaublin, J. Nucl. Mater. **386-388**, 360-362 (2009).

[17] P.D. Edmondson, C.M. Parish, Y. Zhang, A. Hallen and M.K. Miller, J. Nucl. Ma7er. **434**, 210 (2013).

[18] J.N. Al-Hajji and N.M. Ghoniem, Acta Metall. **35**, 1067 (1987).

[19] S.M Hafez Haghighat, G. Lucas and R. Schaublin, EPL **85**, 60008 (2009).

[20] P.D. Edmondson, C.M. Parish, Y. Zhang, A. Hallen and M.K. Miller, J. Nucl. Mater. **434**, 210 (2013).

[21] G.R. Odette, P. Miao, D.J. Edwards, T. Yamamoto, R.J. Kurtz and H. Tanigawa, J. Nucl. Mater. **417**, 1001 (2011).

[22] P.D. Edmondson, C.M. Parish, Y. Zhang, A. Hallen and M.K. Miller, Scripta Mat. **65**, 731 (2011).

[23] L. Barnard, G.R. Odette, I. Szlufarska and D. Morgan, Acta Mat. **60**, 935-947 (2012).

[24] G. Kresse and J. Hafner, Phys. Rev. B **47**, 558 (1993).

[25] G. Kresse and J. Hafner, Phys. Rev. B **49**, 14251 (1994).

[26] G. Kresse and J. Furthmuller, Comput. Mat. Sci. **6**, 15 (1996).

[27] G. Kresse and J. Furthmuller, Phys. Rev. B **54**, 11169, (1996).

[28] P.E. Blochl, Phys. Rev. B **50**, 17953 (1994).

[29] G. Kresse and D. Joubert, Phys. Rev. B **59**, 1758 (1999).

[30] J.P. Perdew, K. Burke and M. Ernzerhof, Phys. Rev. Lett. **77**, 3865 (1996).

[31] J.P. Perdew, K. Burke and M. Ernzerhof, Phys. Rev. Lett. **78**, 1396 (1997).

[32] L. Marsella and V. Fiorentini, Phys. Rev. B **69**, 172103 (2004).

[33] F. Hanic, M. Hartmanová, G. G. Knab, A. A. Urusovskaya and K. S. Bagdasarov, Acta. Cryst. **B40**, 76-82 (1984).

[34] W. Tang, E. Sanville and G. Henkelman, Phys.: Condens. Matter **21**, 084204 (2009).

[35] E. Sanville, S.D. Kenny, R. Smith and G. Henkelman, J. Comp. Chem. **28**, 899-908 (2007).

[36] G. Henkelman, A. Arnaldsson and H. Jonsson, Comput. Mater. Sci. **36**, 254-360 (2006).

[38] J.X. Zheng, G. Ceder, T. Maxisch, W.K. Chim and W.K. Choi, Phys. Rev. B **73**, 104101 (2006).

[39] P.D. Edmondson, C.M. Parish, Q. Li and M.K. Miller, J. Nucl. Mater. **445**, 84-90 (2014).

[40] L. Yang, Y. Jiang, G. R. Odette, T. Yamamoto, Z. Liu and Y. Liu, J. Appl. Phys. **115**, 143508 (2014).

[41] T. Danielson and C. Hin, J. Nucl. Mater. **452**, 189-196 (2014).

5. Ab Initio Investigation of Helium in $Y_2Ti_2O_7$: Mobility and Effects on Mechanical Properties

5.1 Abstract

Oxide nanoclusters (NCs) in nanostructured ferritic alloys (NFAs) are known to be efficient for He accumulations at the cluster/matrix interfaces and can change the mechanical properties. In this study, the migration barriers and potential energy surfaces of helium in $Y_2Ti_2O_7$ are presented to explain the mobility of helium through oxide NCs and shed light on the accumulation of helium and the trapping mechanisms of the oxides. A complex tunnel-like potential energy surface is identified and gives rise to relatively large migration barriers. Subsequently, the effect of helium accumulation on the mechanical properties of $Y_2Ti_2O_7$ oxide nanoclusters is investigated. The bulk modulus was shown to decrease by 22% in the most extreme case of three helium interstitials on the most stable interstitial sites.

5.2 Authors and Affiliations

T. Danielson[1], E. Tea[2] and C. Hin[1,2]

Corresponding Author: Thomas Danielson

[1]Department of Materials Science and Engineering

[2]Department of Mechanical Engineering

Virginia Polytechnic Institute and State University, 635 Prices Fork Road, Blacksburg, VA, 24060, USA

Corresponding Author Email: thomasd1@vt.edu

5.3 Introduction

Nanostructured ferritic alloys (NFAs) are a subset of oxide dispersion strengthened steels that have shown significant promise in the development of materials for the next generation of fission and future fusion reactors. NFAs are characterized by the high number density of complex oxide nanoclusters (NCs) dispersed throughout the matrix. The NCs play a critical role in the alloy's ability to withstand the harsh challenges presented in the reactor environment including;

41

high temperatures, high pressures, neutron irradiation and especially, the accumulation of high concentrations of transmutation product helium [1-4].

The accumulation of helium in NFAs has gained widespread interest in recent years both experimentally and computationally in order to understand the decreased susceptibility of the alloys to helium embrittlement. The investigation has collectively shown evidence that the oxide NCs play a key role in trapping helium, preventing its eventual delivery to grain boundaries and the formation of larger bubbles. However, no complete theoretical explanation exists for the trapping of helium at the oxide NCs, or for how the presence of helium affects the structure and mechanical properties of the oxide NCs. Both of these explanations are key components in the development of more thorough and intricate models, such as kinetic Monte Carlo simulations [5-13], to explain the time evolution of the alloys in reactor environments, as reactor experiments can take decades for relevant reactor-lifetime doses.

Previous first-principles calculations have shown the migration barrier for helium in BCC iron to be extremely low (~0.06 - 0.08 eV) [14,15]. Likewise, the binding energy of individual helium interstitials in BCC iron has been found to be attractive and clusters are further stabilized by the addition of vacancies [14]. Thus, as helium accumulates in the Fe matrix, the low migration barrier in iron and attractive binding energy between He atoms make cluster formation favorable and eventually lead to the coalescence of larger bubbles. Large helium bubbles can become highly pressurized at elevated temperatures and cause swelling and catastrophic cracking. Helium implanter transmission electron microscopy experiments show direct evidence of oxide NCs acting as trapping sites for helium bubbles preventing a significant portion of the bubbles' eventual delivery to grain boundaries where nucleation would otherwise be preferential in BCC Fe [1,16,17]. While He cluster formation is favorable in the BCC iron matrix, first-principles

calculations have shown that this is not the case in the oxide NCs. In the oxides, single helium interstitials occupying separate interstitial sites is the more energetically favorable configuration [19]. The mobility of helium in various oxides has been reported by Erhart [19] to be significantly lower than that in BCC Fe, but no specific path or energy barriers have been given thus far for the $Y_2Ti_2O_7$ system.

The high number density of complex oxide NCs play a crucial role in providing the high creep strength and high yield strength characteristic of NFAs, as well as maintaining the mechanical properties of the bulk alloy under irradiation. The NCs serve to stabilize the grains and prevent grain boundary sliding under tensile stresses at the elevated temperatures and pressures of a reactor environment, resulting in increased creep strength [20-23]. Consequently, dislocation glide has been found to be the dominant deformation mechanism in NFAs [20]. The NCs serve to pin dislocations through Orowan looping processes, preventing glide, which ultimately leads to the increased strength of the alloys. Likewise, maintaining a high dislocation density is crucial for maintaining high creep strength as dislocations serve as annihilation sites for point defect damage from incident radiation.

To this point, no theoretical studies exist describing the effects of helium interstitials on the mechanical properties of the oxide NCs, however, it is critical that the NCs maintain their mechanical properties as helium accumulates. If the mechanical properties of the NCs degrade significantly, pinned dislocations may be more likely to shear the precipitates due to the elastic field interaction of the precipitate and dislocation. Each time the precipitate is sheared, its resistance to dislocation motion is again reduced, which can ultimately result in regions of plastic flow [24]. Thus, degradation of oxide mechanical properties may potentially lead to changes in the bulk mechanical properties.

By investigating the mobility of helium in $Y_2Ti_2O_7$, as well as the mechanical properties of the oxide containing helium, we can gain insight into the trapping mechanisms of helium at the oxide-Fe interface in NFAs, as well as the likelihood and degree to which the mechanical properties may degrade as helium accumulates in a reactor environment. This provides valuable insight, not only theoretically for prevention of helium embrittlement in reactor materials, but also for building complex reactor lifetime scale models. In the next section, the computational methods and interstitial locations are described. In Section 3, results on the bulk moduli, mobility of helium and the potential energy landscape of a helium atom in $Y_2Ti_2O_7$ are presented. Finally, a discussion of the results and their implications for NFAs is presented.

5.4 Computational Methods

The ground state energy of $Y_2Ti_2O_7$ has been evaluated using density functional theory (DFT) in order to determine the migration barriers, potential energy landscape and bulk moduli of the $Y_2Ti_2O_7$ + He system. DFT calculations have been performed as implemented in the VASP code [25-28] using the projector-augmented wave method [29,30]. The 4s and 4p, 3p and 2s electrons are considered as valence electrons for Y, Ti and O respectively. The generalized gradient approximation (GGA) from Perdew, Berke and Ernzerhoff (PBE) [31,32] has been shown to most accurately describe the behavior of helium [33] and thus, has been used to describe the exchange-correlation functional of the valence electrons. For each calculation, one fully periodic $Y_2Ti_2O_7$ unit cell has been used where the Brillouin zone is sampled using a 4x4x4 k-point mesh and a plane-wave energy cutoff of 600 eV. During structural relaxation, the total energy is converged to 10^{-6} eV.

The mechanical properties of the crystal can be derived from its cubic symmetry. Upon introduction of helium interstitials to the crystal structure, slight distortions occur along the axes if relaxation of the cell shape is performed. Thus, full relaxation of the pure system is performed

prior to introducing any interstitials to ensure the symmetry of the crystal is maintained. Following

introduction of helium interstitials, subsequent relaxation of the ions is performed with the cell

shape and volume fixed. The bulk moduli are determined based on an energy-volume relationship

obtained by applying volumetric strain. The helium interstitial positions and their relative

stabilities have been previously investigated using first-principles for the $Y_2Ti_2O_7$ pyrochlore

structure and are shown in Figure 5.1 [33].

Y$_2$Ti$_2$O$_7$
Interstitial
Configurations

Octahedral	Tetrahedral	O - O	Y - Y
$E_{Sol} = 0.86$ eV	$E_{Sol} = 1.51$ eV	$E_{Sol} = 1.39$ eV	$E_{Sol} = 1.59$ eV
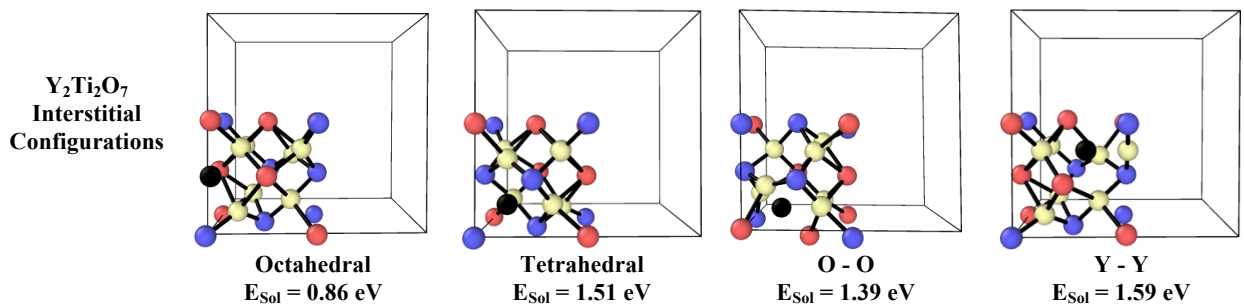
Figure 5.1 Interstitial configurations and calculated solution energies for $Y_2Ti_2O_7$ [33] where the black sphere represents the helium interstitial. Only the bottom 1/8th of the cell is shown as this is the smallest repeating unit of the cell.

5.5   Results

In order to understand how the accumulation of helium at oxide nanoclusters will

potentially affect the mechanical properties of the bulk NFA, the migration barriers, potential

energy landscape and the mechanical properties of the oxide containing helium have been

investigated. The migration barriers have been investigated using the climbing image nudged

elastic band method and give insight to how readily helium interstitials can diffuse between

interstitial locations upon implantation and arrival at an oxide NC. From this, we can learn how

favorable it is for the He atom to either remain trapped at the oxide-Fe interface, or diffuse through

the oxide and what path would be the most favorable. The potential energy landscape sheds light

on the migration barriers and gives a more physical interpretation of the ability for helium to

diffuse, as well as the reasons that the interface between oxide NCs and BCC iron are efficient

trapping sites for helium. Finally, investigation of the bulk moduli of the oxide containing helium

provides insight to how the mechanical properties of the alloy will be altered as helium accumulates at the oxide-Fe interface.

5.5.1 *Migration barriers of helium in $Y_2Ti_2O_7$*

In order to gain insight to the likelihood of degradation of the mechanical properties of the oxide NC when helium is present, the mobility of helium between interstitial locations has been investigated. In addition, the migration barriers provide a valuable comparison between the mobility of helium in BCC iron having a low energetic barrier (0.07 eV) [23,24] and the mobility of helium in the oxide. The migration barriers of helium through a $Y_2Ti_2O_7$ oxide nanocluster has been investigated using the climbing image nudged elastic band [34-36]. The climbing image nudged elastic band connects a sequence of images with a spring of constant, *k*, in a geometrically interpolated path between the initial and final state. From this, a force projection scheme is used where potential forces act perpendicular to the band and spring forces act parallel to the band to relax each image to its ground state. The spring forces keep the images evenly separated on the reaction coordinate axis, while all images undergo successive constrained atomic relaxations. The image with the highest energy climbs up the potential energy surface and locates the saddle point.

As a result, a reversible migration energy and path can be extracted for helium through the host matrix. The higher energy interstitial location is assumed to be the initial state, and the lowest energy interstitial location is always assumed to be the final state, e.g. in our case the octahedral interstitial position. However, when the octahedral site is the initial and final state as shown in Figures 5.2a and 5.3, the helium atom must travel through one of the stable interstitial positions in order to reach an adjacent octahedral site. From each of these interstitial positions to the nearest octahedral interstitial position, the most likely energetic pathway for a helium atom to diffuse through the oxide can be determined by investigating the barrier. The three distinct migration paths investigated are:

- Octahedral interstitial location to an adjacent octahedral interstitial location via a neighboring tetrahedral interstitial location (Figure 5.2a)

- Y-Y interstitial location to an adjacent octahedral interstitial location (Figure 5.2b)

- O-O interstitial location to an adjacent octahedral interstitial location (Figure 5.3)

In each case, the neighboring oxygen atoms must be significantly displaced in order for the helium interstitial to migrate from the initial to final location. Similarly, helium interstitials occupying the Y-Y or O-O interstitial configurations cause significant displacement of atoms from equilibrium lattice sites. Thus, when a helium atom migrates from these sites to either an octahedral location (a configuration that causes significantly less disorder to the cell), significant relaxation of the neighboring atoms towards their equilibrium sites occurs.

The local minimum in the barrier for migration from octahedral to octahedral location is representative of the helium atom passing through the tetrahedral location. The tetrahedral location is a vacant oxygen site through which the neighboring oxygen atoms force the helium interstitial to migrate when moving between two octahedral locations. In a similar fashion, all octahedral interstitial locations are directly neighbored by one of the other three interstitial sites. Thus, in order to leave an octahedral position, the path must go through another interstitial site before either: 1) returning to the original octahedral site or 2) migrating to an adjacent octahedral site. The calculated (NEB) migration barrier for moving from O-O to an adjacent octahedral location is 0.014 eV showing that this interstitial position is only quasi-stable. Thus, the helium interstitial will migrate from this location nearly athermally. This low migration barrier is also indicative that the O-O site is the transition state between octahedral locations when moving in the direction of an O-O site. Consequently, the path shown in Figure 5.3, where the helium interstitial travels from octahedral to a neighboring octahedral through the O-O position, is the most favorable

path for helium to diffuse with a barrier of 0.544 eV. This value is directly deduced from the difference in energy of octahedral and O-O, O-O being the transition state.
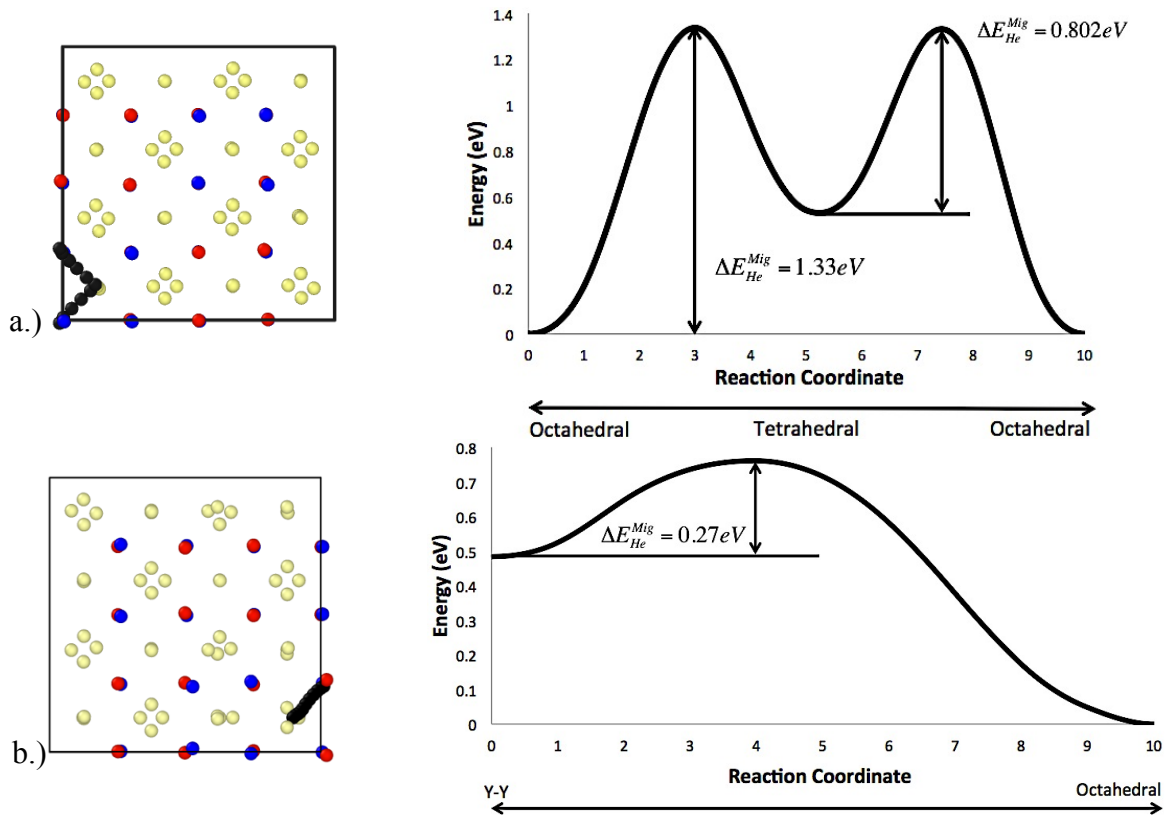
Figure 5.2 The migration path and barrier for a) migration from an octahedral location to an adjacent octahedral location and b) from a Y-Y location to an adjacent octahedral location.
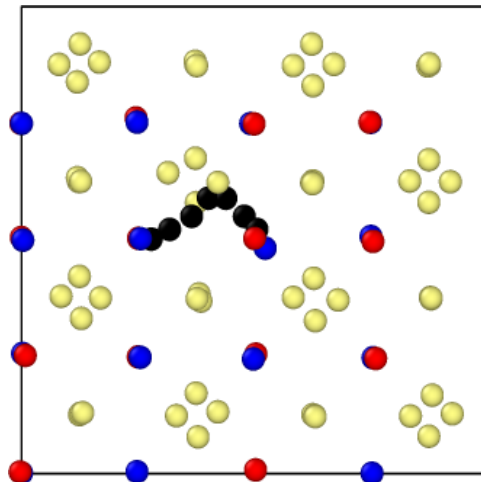
Figure 5.3 The complete, lowest energy path for helium to travel from octahedral to O-O to octahedral interstitial positions.

5.5.2 *Potential energy landscape for helium in $Y_2Ti_2O_7$*

The potential energy landscape for a helium atom in $Y_2Ti_2O_7$ has been investigated by calculating the total energies of $Y_2Ti_2O_7$ matrices containing a helium atom placed at different locations. For each helium atom location, the nearest neighbor atoms of the $Y_2Ti_2O_7$ matrix are relaxed while the helium position is fixed, so that the helium atom is not allowed to drift to a nearby stable interstitial position. The different helium atom positions map a 8x8x8 regular mesh of the $Y_2Ti_2O_7$ matrix in order to reveal regions of the crystal with high and low potential energies where helium migration would come at a high or low energetic cost, respectively. The helium potential energy landscape is shown in Figure 5.4 in (100), (110) and (111) crystallographic planes.
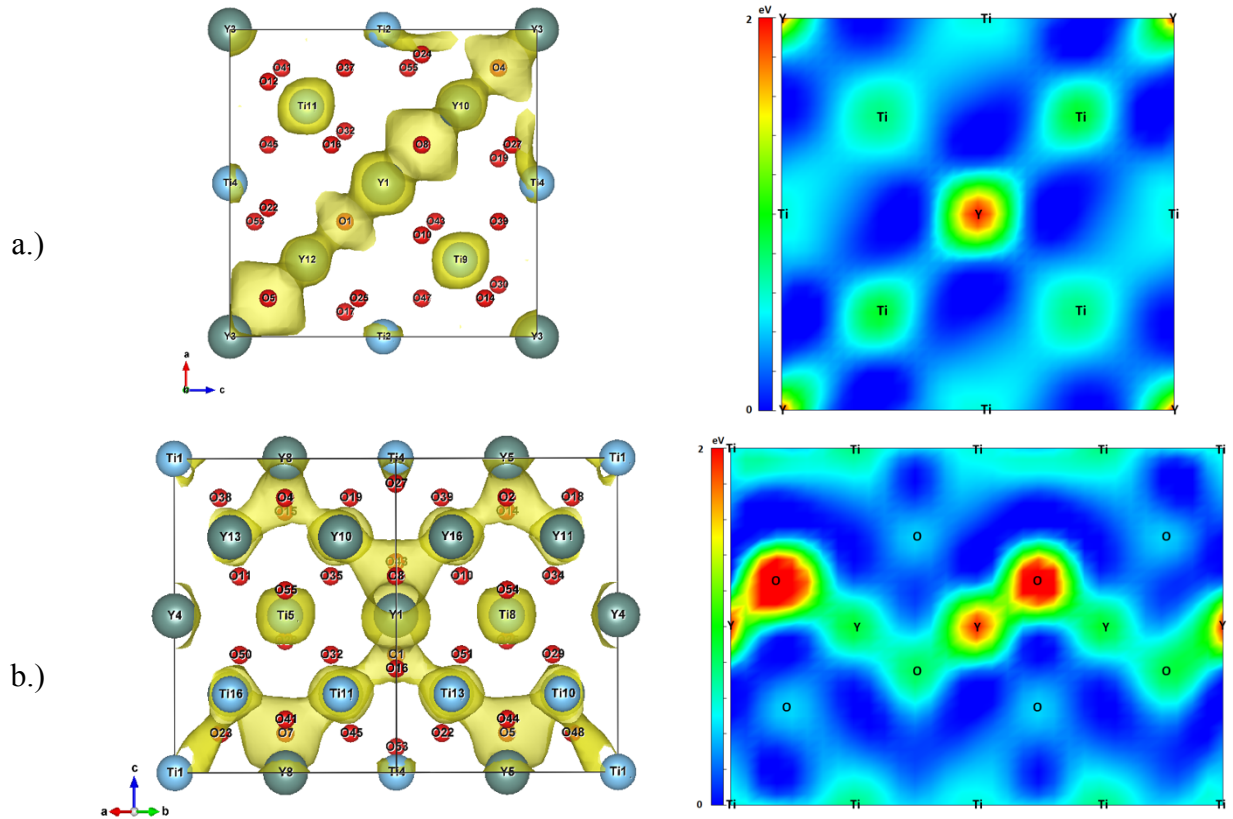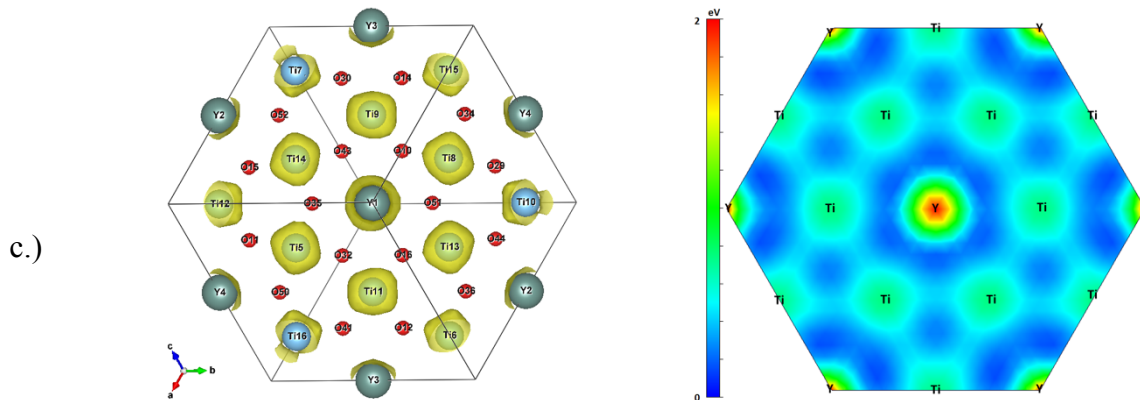
Figure 5.4 Isosurfaces and mapping of helium potential energy surfaces in the a.) (100) plane, b.) (110) plane and c.) (111) plane of the $Y_2Ti_2O_7$ crystal.

The largest diffusion barriers in $Y_2Ti_2O_7$ occur near O atoms, which are tetrahedrally coordinated by four Y atoms. The potential energy near O atoms that are tetrahedrally coordinated by two Y and two Ti atoms is smaller, but still gives rise to rather high barriers (>0.4 eV). The minimum energy path is clearly shown in Figure 5.4b (shown in a perpendicular (110) direction to the mapping for perspective) where there is a network of octahedral to O-O to octahedral sites. The PES agrees well with the calculated migration barrier of ~0.5eV.

The small amount of free volume is evident in the $Y_2Ti_2O_7$ unit cell and it is clearly shown, particularly in the (111) plane. The free volume in the crystal for helium diffusion is composed of a network of crossed tunnels, which corresponds to low potential energy regions in a high potential energy matrix. Even if the potential energy in the tunnels is low compared to the potential energy close to an O atom coordinated by four Y atoms, helium atoms cannot diffuse through these tunnels easily because of diffusion barriers within the 1-2 eV range. Potential energy minima exist at the octahedral sites and thus, when a helium atom reaches an octahedral site, it is unable to migrate without significant energetic cost.

5.5.3   *Mechanical properties of $Y_2Ti_2O_7$ containing helium interstitials*

The bulk modulus of $Y_2Ti_2O_7$ containing helium on the distinct interstitial sites has been investigated in order to understand how the mechanical properties of the bulk alloy may be affected

50

as helium concentration within the alloy increases and significant helium trapping at oxide NCs occurs. The bulk modulus has been calculated by applying volumetric strain in the range of +/- 5%, however, care has been taken to ensure that only the elastic regime is considered. The ground state energy at each of these strains is then fit to a second order polynomial and the bulk modulus is calculated as:

$$B = V_o \frac{d^2E(V)}{dV^2} \tag{1}$$

where, V_o is the equilibrium volume. The bulk modulus of pure $Y_2Ti_2O_7$ has been calculated and verified with existing DFT calculations [37] as 183.031 GPa and the corresponding energy-volume curve is shown in Figure 5.5.
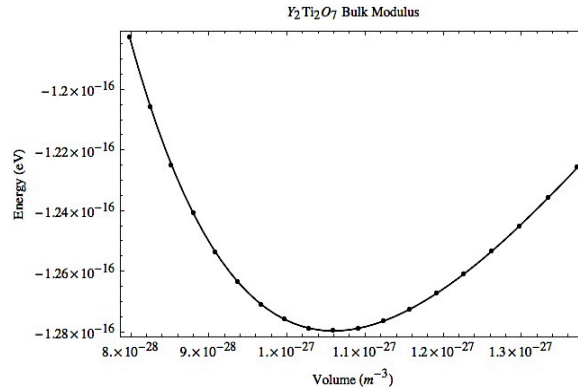
Figure 5.5 Energy-volume relationship for pure $Y_2Ti_2O_7$ straining in the range of +/- 5% volumetrically.

Helium interstitials have been added to each interstitial site and up to three helium interstitials have been placed within the cell on separate octahedral sites in the most stable configurations as calculated by [33,37]. The calculated bulk moduli are shown in Table 5.1. The bulk moduli are dependent upon the symmetry of the cell, thus in all cases except for the tetrahedral interstitial configuration, the bulk modulus decreases as a result of the decreased symmetry. The more displacement of atoms from their equilibrium lattice sites, the more significant the decrease in the bulk modulus.

51

Table 5.1 Bulk moduli for the $Y_2Ti_2O_7$ + He system containing up to 3 helium interstitials.

	Bulk Modulus (GPa)
Pure $Y_2Ti_2O_7$	183
Octahedral	167.4
Tetrahedral	182.9
Y-Y	163.8
O-O	159.1
2 He Oct I	160.1
2 He Oct II	151.3
3 He Oct	142.2

5.6   Discussion

The trapping mechanisms of helium at the oxide nanoclusters can be well understood based on the potential energy landscape calculations performed. Oxygen atoms tetrahedrally coordinated by four Y atoms create large potential energy barriers and a complex crossed tunnel-like potential energy surface. Thus, many separate potential energy minima exist at the octahedral interstitial locations and the mobility of helium out of one of these locations is highly limited by large barriers surrounding the energy minimum. The migration barriers of helium in BCC Fe are very low (one order of magnitude lower than in the oxide) and the solution energies for helium interstitials are high relative to the oxide [14]. Thus, as helium diffuses through the iron matrix and reaches the complex potential energy landscape of the oxide NC, it becomes more energetically favorable to remain trapped at the oxide-Fe interface than to diffuse through the oxide or return to the matrix. The exact interfacial structure between the oxide NCs in NFAs is not currently known, but the complex potential energy landscape provides a reasonable explanation for the trapping of helium at the oxide-Fe interface. Further investigations of the oxide-Fe interface are undergone to be certain that more complex trapping mechanisms are not being overlooked.

The minimum energy path for helium to diffuse was found to be: octahedral location to O-O location back to an octahedral location. The symmetry of the $Y_2Ti_2O_7$ unit cell is such that many different O-O interstitial positions exist. Consequently, many different pathways that lead from an initial octahedral position to an adjacent octahedral position via O-O exist. Due to the computational expense of the NEB, each of these pathways has not been investigated separately, but based on the symmetry and the investigation of the potential energy surface, it is reasonable to assume that the barriers would be very close to the reported 0.544 eV. The migration barriers and potential energy landscape of $Y_2Ti_2O_7$ are comparable to those of Y_2O_3. However, the $Y_2Ti_2O_7$ complex oxide structure has a more intricate atomic structure due to the mixture of oxygen atoms tetrahedrally coordinated by 4 Y, or 2 Y and 2 Ti. Compared to the octahedrally coordinated O in Y_2O_3, the tetrahedrally coordinated O in $Y_2Ti_2O_7$ results in less free volume in the cell and create a more intricate potential energy landscape. Ultimately, the rugged potential energy landscape leads to more difficult migration paths between the most stable sites and as a result, $Y_2Ti_2O_7$ oxide NCs may contain more efficient helium trapping sites than Y_2O_3.

Significant degradation of the mechanical properties of the oxide NCs in NFAs as helium accumulates could have significant implications for the degradation of the overall bulk mechanical properties of the alloy. Helium implanter TEM investigations have shown the surface of oxide NCs nearly completely covered by helium bubbles [16,17]. In addition, helium bubbles act as trapping sites for additional helium atoms. When the surface of the oxide NC is completely covered by bubbles and the continual growth of the bubbles occurs, the pressure of the bubbles continues to increase. The resulting pressure increase imposes a growing amount of strain on the matrix/oxide interface. If the pressure of the bubble becomes high enough, the strain energy could be released by causing either the matrix or the oxide to deform plastically. If there is a significant

decrease to the bulk modulus of the oxide, any resulting plastic deformation caused by the pressurized bubble will occur within the oxide and the overall stability of the NC could become further compromised. Investigation of the bulk modulus of $Y_2Ti_2O_7$ reveals how compliant the oxide NC is likely to become with increasing helium concentrations. When the oxide contained up to three helium interstitials (~3 at% in the oxide) in the most energetically stable configurations, the bulk modulus decreased by about 22%. However, while this decrease may be significant, the potential energy surface and migration barrier calculations performed indicate that the helium atoms will be deeply trapped at the octahedral sites and further diffusion through the oxide will be energetically unfavorable for implanted helium. Thus, so long as an available octahedral site (or other stable location along the interface's potential energy surface) exists near the Fe-$Y_2Ti_2O_7$ interface, the helium atom will likely remain trapped at this site where a bubble can form along the interface instead of having significant accumulation of helium within the oxide itself and the oxide NCs will likely maintain their overall mechanical properties reasonably well.

5.7   Conclusions

The bulk modulus of $Y_2Ti_2O_7$ containing helium interstitials on each of the previously located sites was calculated and shown to decrease by approximately 22% for the most extreme case of three helium interstitials on the octahedral sites. The potential energy landscape was also calculated and indicates that the helium will remain deeply trapped at the octahedral sites that correspond to deep potential energy wells. The complex potential energy landscape and spatially large potential energy maxima surrounding Y-O tetrahedra makes diffusion energetically unfavorable and provides an explanation for the trapping mechanisms of helium at oxide nanoclusters.

5.8   Acknowledgements

References

[1] G.R. Odette, M.J. Alinger, B.D. Wirth, Annu. Rev. Mater. Res. **38**, 471 (2008).

[2] J.H. Schneibel, M. Heilmaier, W. Blum, G. Hasemann, T. Shanmugasundaram, Acta Mat. **59**, 1300 (2011).

[3] R.L. Klueh, P.J. Maziasz, I.S. Kim, L. Heatherly, D.T. Hoelzer, N. Hashimoto, E.A. Kenik, K. Miyahara, J. Nucl. Mater. **307-311**, 773 (2002).

[4] D.A. McClintock, D.T. Hoelzer, M.A. Sokolov, R.K. Nanstad, J. Nucl. Mater. **386-388**, 307 (2009).

[5] C. Hin. Adv. Funct. Mater. **21(13)**, 2477 (2011).

[6] C. Hin. B.D. Wirth. Mater. Sci. Eng. A. **528(4-5)**, 2056 (2011).

[7] C. Hin. M. Dresselhaus, G. Chen. Appl. Phys. Lett. **97**, 251909 (2010).

[8] C. Hin. B.D. Wirth. J. Nucl. Mat. **402**, 30 (2010).

[9] C. Hin. B.D. Wirth, J.B. Neaton. Phys. Rev. B. **80**, 134118 (2009).

[10] C. Hin. J. Phys. D: App. Phys. **42**, 225309 (2009).

[11] C. Hin. Y. Bréchet, P. Maugis, F. Soisson.   Acta Mat. **56**, 5653 (2008).

[12] C. Hin. Y. Bréchet, P. Maugis, F. Soisson. Acta Materialia. **56**, 5535 (2008).

[13] C. Hin. Y. Bréchet, P. Maugis, F. Soisson. Phil. Mag. **88(10)**, 1555 (2008).

[14] C.C. Fu and F. Willaime, Phys. Rev. B **72**, 064117 (2005).

[15] T. Yamamoto, G.R. Odette, R.J.Kurtz, B.D. Wirth, Fusion Reactor Materials Program DOE/ER-0313/49, **73** (2010).

[16] P.D. Edmondson, C.M. Parish, Y. Zhang, A. Hallen, M.K. Miller, J. Nucl. Mater. **434**, 210 (2013).

[17] G.R. Odette, P. Miao, D.J. Edwards, T. Yamamoto, R.J. Kurtz, H. Tanigawa, J. Nucl. Mater. **417**, 1001 (2011).

[18] P.D. Edmondson, C.M. Parish, Y. Zhang, A. Hallen, M.K. Miller, Scripta Mat. **65**, 731 (2011).

[19] P. Erhart, J. Appl. Phys. **111**, 113502 (2012).

[20] M.C. Brandes, L. Kovarik, M.K. Miller, G.S. Daehn, M.J. Mills, Acta Mat. **60**, 1827-1839 (2012).

[21] J.H. Schneibel, C.T. Liu, M.K. Miller, M.J. Mills, P. Sarosi, M. Heilmaier, D. Sturm, Scripta Mat. **61**, 793-796 (2009).

[22] R.L. Klueh, P.J. Maziasz, I.S. Kim, L. Heatherly, D.T. Hoelzer, N. Hashimoto, E.A. Kenik, K. Miyahara, J. Nucl. Mat. **307-311**, 773-777 (2002).

[23] T. Hayashi, P.M. Sarosi, J.H. Schneibel, M.J. Mills, Acta Mat. **56**, 1407-1416 (2008).

[24] A. Takahashi, N.M. Ghoniem, J. Mech. Phys. Sol. **56**, 1534-1553 (2008).

[25] G. Kresse, J. Hafner, Phys. Rev. B **47**, 558 (1993).

[26] G. Kresse, J. Hafner, Phys. Rev. B **49**, 14251 (1994).

[27] G. Kresse, J. Furthmuller, Comput. Mat. Sci. **6**, 15 (1996).

[28] G. Kresse, J. Furthmuller, Phys. Rev. B **54**, 11169 (1996).

[29] P.E. Blochl, Phys. Rev. B **50**, 17953 (1994).

[30] G. Kresse, D. Joubert, Phys. Rev. B **59**, 1758 (1999).

[31] J.P. Perdew, K. Burke, M. Ernzerhof, Phys. Rev. Lett. **77**, 3865 (1996).

[32] J.P. Perdew, K. Burke, M. Ernzerhof, Phys. Rev. Lett. **78**, 1396 (1997).

[33] T. Danielson, C. Hin, J. Nucl. Mater. **452**, 189-196 (2014).

[34] H. Jonsson, G. Mills, K.W. Jacobsen, Nudged Elastic Band Method for Finding Minimum Energy Paths of Transitions. B. J. Berne, G. Ciccotti and D. F. Coker, editors. In: Classical and Quantum Dynamics in Condensed Phase Simulations. World Scientific. 1998.

[35] G. Henkelman, H. Jónsson, J. Chem. Phys. **113**, 9901-9904 (2000).

[36] G. Henkelman, H. Jónsson, J. Chem. Phys. **113**, 9978-9985 (2000).

[37] Jiang Y, Smith JR, Odette GR. Acta Mat. **58**, (2010) 1536.

6. Investigation of Helium at a $Y_2Ti_2O_7$ Nanocluster Embedded in a BCC Fe Matrix

6.1 Abstract

Nanostructured ferritic alloys (NFAs) are prime candidates for structural and first wall components of fission and fusion reactors and a primary reason for this is their ability to effectively withstand high concentrations of transmutation product helium. A high number density of oxide nanoclusters dispersed throughout a BCC Fe matrix act as trapping sites for helium and prevent its eventual delivery to high risk nucleation sites. The current study uses density functional theory to investigate the helium trapping mechanisms of $Y_2Ti_2O_7$; a common stoichiometry of the oxide nanoclusters in NFAs. The investigation is carried out on a structure matched oxide nanocluster that is embedded within a BCC Fe supercell. Investigation of the electronic structure and a mapping of the potential energy landscape reveals that the localized iono-covalent bonds present within the oxides create a potential energy-well within the metallically bonded BCC Fe matrix.

6.2 Authors and Affiliations

Thomas Danielson[1*], Eric Tea[2] and Celine Hin[1,2]

[1]Department of Materials Science and Engineering, Virginia Polytechnic Institute and State University, USA

[2]Department of Mechanical Engineering, Virginia Polytechnic Institute and State University, USA

[*]Corresponding Author: thomasd1@vt.edu

6.3 Introduction

The potential risk of embrittlement of structural components of nuclear reactor materials is posed by the persistent production of nuclear transmutation products, such as helium. High temperatures exacerbate this risk by allowing such an inert species to readily diffuse through alloy materials where its eventual delivery to microstructural defects, such as grain boundaries and voids, can lead to nucleation of highly pressurized helium bubbles [1, 2]. The pressure within

these bubbles poses the catastrophic threat of crack formation, growth, and potential failure of the material. From this has grown a primary interest to develop materials that are capable of mitigating the risks of embrittlement. One such class of materials is an oxide dispersion strengthened steel called nanostructured ferritic alloys (NFAs). The prime candidacy of NFAs for the application of nuclear reactor materials stems from their remarkable ability to withstand, not only high concentrations of helium, but the accompanying high temperatures, pressures and neutron fluxes of the reactor environment[3-8].

The ability of NFAs to withstand harsh nuclear reactor conditions arises from microstructural features produced by highly non-equilibrium mechanical alloying, hot consolidation and post-processing heat treatments [3, 7, 9]. Such microstructural features are: highly refined elongated grains, high dislocation densities, and a high number density of Y-Ti-O oxide nanoclusters (NCs) dispersed throughout the BCC Fe matrix [7, 10-12]. The oxide NC phases exist in varying stoichiometric compositions such as Y_2O_3, Y_2TiO_5 and $Y_2Ti_2O_7$, and are formed during hot consolidation and post-processing heat treatments following dissolution of Y_2O_3 powder into the Fe alloy matrix powder [11]. NCs have exceptional thermal stability and serve to pin dislocations, providing a high yield strength, high creep strength and the maintenance of a large number of annihilation sites for radiation induced accumulation of point defect damage [5, 6, 13-16]. In addition, oxide NCs within NFAs act as trapping sites for helium, where experimental studies have shown that greater than 50% of bubbles within the material are associated with an oxide NC [17-20].

Various first-principles calculations have been performed in order to investigate the confinement of helium to the oxide NCs, but primarily, these have taken place in either the oxide bulk or bulk BCC Fe [21-26]. Results from these investigations have shown that the formation

energy associated with creating a helium interstitial is significantly higher in BCC Fe (~4.5 eV) [26] than in the oxides (~1-1.5 eV) [21-26]. Additionally, the investigations have revealed that the migration barrier of helium in the Fe matrix is extremely low (0.07 eV) [26] compared to the oxides (0.5-1.5 eV) [22, 24], where the constituent oxygen atoms of the oxides play a key role in prohibiting helium migration. A recent investigation of the $Y_2Ti_2O_7$ / Fe interface found that there are low vacancy formation energies and similar helium defect formation energetics to the bulk oxides which promotes the sequestration of helium from the matrix to the interface [27]. In addition, Yang et al. concluded that subsequently formed helium bubbles acted as point defect sinks for radiation induced defect damage [27].

Although the interface has been investigated with a particular highly strained orientation relationship, thus far, no investigations of the interaction of helium with an oxide NC embedded in the matrix exist within the literature, but the associated energetic landscape can help to shed additional light on the helium trapping mechanisms of oxide NCs in NFAs. In the current work, a first-principles investigation is performed on a $Y_2Ti_2O_7$ oxide NC embedded in Fe using a structure-matched computational setup that has been previously used to investigate the formation of Y-Ti-O NCs in NFAs [28, 29]. The primary result is a mapping of the potential energy landscape that shows that localized iono-covalent bonding within the oxide NCs plays a key role in providing a high number density of potential energy wells for helium trapping throughout the BCC Fe matrix.

6.4 Simulation Setup

Density functional theory as implemented by VASP [30-33] has been utilized to investigate the structure and energetics of an oxide nanocluster embedded in an iron matrix with and without helium. Pseudopotentials generated within the projector augmented wave [34, 35] formalism from the generalized gradient approximation of Perdew, Burke and Ernzerhoff [36, 37], describe the

interaction between atomic species. The following electrons are considered as interacting valence electrons amongst the constituent atomic species: $Y - 4s$, $4p$, $5s$ and $4d$; $Ti - 3d$ and $4s$; $O - 2s$ and $2p$; $Fe - 3d$ and $4s$; $He - 1s$. A 4 x 4 x 4 Monkhorst-Pack K-point mesh and a plane-wave energy cutoff of of 400 eV have been used. For each simulation, the cell shape and volume have been fixed, but the atomic positions and the electronic structure have been relaxed until the total energy has converged to 1 meV/atom.

The problem of investigating the interface between an oxide NC and the Fe matrix using density functional theory is complicated by the complexity of the semi-coherent $Y_2Ti_2O_7 - Fe$ interface. Various energetically favorable orientation relationships have been experimentally investigated, one of which is $\{100\}$ Fe // $\{100\}$ $Y_2Ti_2O_7$ and $\langle 100 \rangle$ Fe // $\langle 100 \rangle$ $Y_2Ti_2O_7$ as shown by Ribis and de Carlan [38]. The associated lattice mismatch with this orientation is about 12.6% and thus, a misfit dislocation exists every 8 $\{110\}$ Fe planes and every 9 $\{440\}$ $Y_2Ti_2O_7$ planes. In order to implement this structure using DFT, an extremely large supercell would be required as the number of planes in the x, y and z directions must be substantial to implement a misfit dislocation while maintaining the proper periodicity. Without such microstructural features present, significant strain must be applied to either Fe or $Y_2Ti_2O_7$, or both, and significant contributions to the overall energetics would result from this associated strain. Thus, based on the simulation setup requirements for such an interface calculation, a more computationally feasible approach is the case of the structure matched embedded oxide nanocluster as implemented by Barnard et al [28] shown in Figure 6.1. For all simulations, the NC is embedded in a matrix of iron that corresponds to 4 x 4 x 4 BCC unit cells. In the current setup, the oxide nanocluster corresponds to the bottom $1/8^{th}$ of the $Y_2Ti_2O_7$ unit cell with the metal atoms along the (100) edges of the oxide unit cell replaced by Fe. The width of the oxide NC at its widest point is 0.49 nm.

Thus, the size of the oxide NC with the current setup would correspond to the smallest of $Y_2Ti_2O_7$ oxide NCs in NFAs. However, while the size of the oxide NC is small, experiments have shown that the smallest precipitates within NFAs correspond to the $Y_2Ti_2O_7$ pyrochlore structure [11] and thus, the methods used in the current investigation can provide insight for the trapping mechanisms of helium at oxide NCs of any potentially size in NFAs.
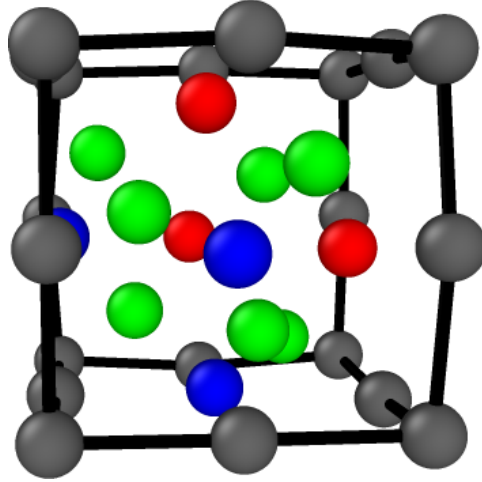
Figure 6.1 Structure matched $Y_2Ti_2O_7$ oxide nanocluster embedded in Fe. Red, blue, green and silver atoms represent Y, Ti, O and Fe respectively.

In order to validate the current computational setup, the formation energy of the oxide NC has been calculated and compared to previous calculations. The formation energy has been calculated as:

$$\Delta E_F = E(w_{Fe}, x_Y, y_{Ti}, z_O) - (w\mu_{Fe} + x\mu_Y + y\mu_{Ti} + z\mu_O) \tag{1}$$

where, $E(w_{Fe}, x_Y, y_{Ti}, z_O)$ is the total energy of the embedded oxide in Fe, and $w\mu_{Fe}$ is the number of Fe atoms multiplied by the energy of the reference state (similar meanings for $x\mu_Y$, $y\mu_{Ti}$, and $z\mu_O$). The reference states for each species are as follows: Fe – the energy per Fe atom in a BCC cell; Y – the energy of a substitutional Y atom in BCC Fe; Ti – the energy of a substitutional Ti atom in BCC Fe; O – the energy of an O as an octahedral interstitial in BCC Fe. With this formalism, the energy required to form the oxide NC is -6.45 eV/metal atom and is in

good agreement with previous calculations on the formation of oxide NCs of this composition in

BCC Fe [28].

6.5   Results
6.5.1   *Helium at the Oxide-Fe Interface*

The formation energy of helium has been calculated along the symmetry equivalent

locations of the oxide-Fe interface, and inside the oxide, in order to make a comparison between

the relative stability of helium at the interface and in Fe. In order to ensure that all sites along the

interface are investigated, a helium atom has been placed in each of the eight corners of the of the

Fe cube encompassing the oxide octahedron. In addition, an octahedral interstitial site (the most

stable He interstitial location in the bulk oxide) exists at the center of the oxide and an interstitial

He atom has been placed on this site as well. Relaxation of the helium atom from its initial position

reveals four stable symmetry equivalent locations around the interface and one stable location at

the center of the cell on the octahedral interstitial location, shown in Figure 6.2.
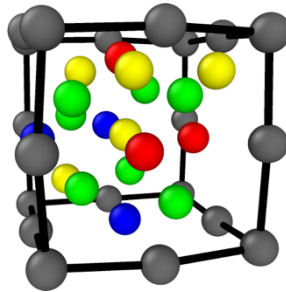
Figure 6.2 Four distinct interstitial configurations at the oxide-Fe interface and one interstitial location within the oxide at the octahedral location. Red, blue, green, yellow and grey atoms are Y, Ti, O, He and Fe, respectively.

The interstitial locations exist along the faces and the edges of the octahedrally shaped oxide.

The stable helium locations along the faces are described with respect to the oxide's metallic

species that are located at the vertices of the octahedron and are described as follows:

- He coordinated by two Ti atoms and one Y atom

- He coordinated by three Ti atoms (this corresponds to the tetrahedral interstitial position in the bulk oxide)

- He coordinated by three Y atoms

The stable helium location along the edges is described with respect to the oxide's metallic species located at the corresponding vertices of the octahedron as:

- He coordinated by two Y atoms

The formation energy of each stable helium location is calculated as:

$$E_{He}^{For} = E(Fe, Y, Ti, O, He) - (E(Fe, Y, Ti, O) + E(He)) \tag{2}$$

where, $E(Fe, Y, Ti, O, He)$ is the energy of the supercell containing a helium atom associated with the oxide NC embedded in Fe, $E(Fe, Y, Ti, O)$ is the total energy of the supercell containing the oxide NC embedded in Fe, and $E(He)$ is the total energy of an isolated helium atom. Each of the interstitial positions in their relaxed configurations and the respective formation energy are shown in Figure 6.3 (a-e). Each of the helium defect formation energies for positions located at the oxide-Fe interface are within ~0.1 eV showing that the stability of helium at the interface in different positions is roughly equivalent. The most stable helium location is at the octahedral interstitial position of the oxide, which is incidentally where the distance between helium and Fe is maximized. In addition, previous investigations of the bulk oxide have shown that the surrounding oxygen atoms play a key role in deeply trapping the interstitial helium at the octahedral sites [21-23].

$E_{He}^{For} = 2.31\ eV$ $E_{He}^{For} = 2.34\ eV$ $E_{He}^{For} = 2.19\ eV$ $E_{He}^{For} = 2.26\ eV$ $E_{He}^{For} = 1.85\ eV$
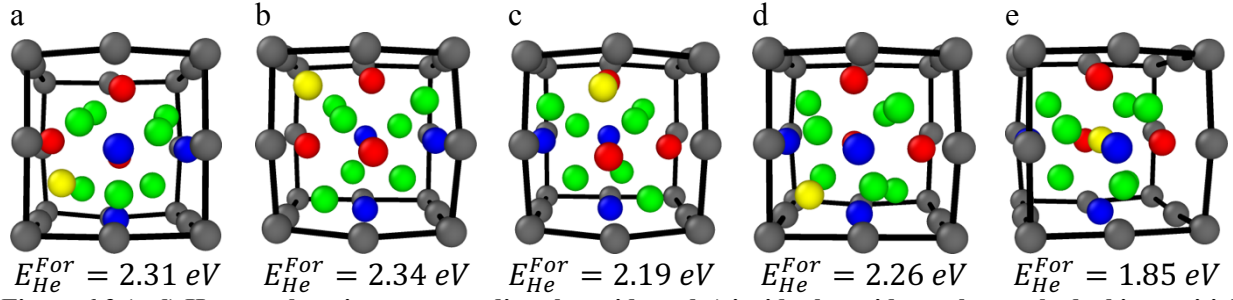
Figure 6.3 (a-d) He atom locations surrounding the oxide and e) inside the oxide on the octahedral interstitial location.

The most stable helium interstitial location in BCC Fe has been previously calculated by Fu et al. as the tetrahedral interstitial location with a formation energy of 4.38 eV [26]. The formation energy of a helium interstitial, placed at a tetrahedral interstitial location at the farthest point from the embedded NC, was investigated within the supercell for comparison and the formation energy is 4.67 eV confirming that helium is significantly more stable in the oxide NC and at the interface.

To investigate an accumulation of helium on the most stable interstitial location, two helium interstitials (~1.5 at %) have been initially centered on the octahedral interstitial position and relaxed to their stable positions. The relaxed structure is shown in Figure 6.4 and shows that an oxygen atom is ejected from the center of the oxide NC and becomes an interstitial located at the octahedral position in Fe, which is the most stable interstitial position for O in Fe. In addition, one helium atom remains at the central octahedral location, while the other finds its lowest energy position at the facet of the oxide. The associated formation energy is 4.1 eV.
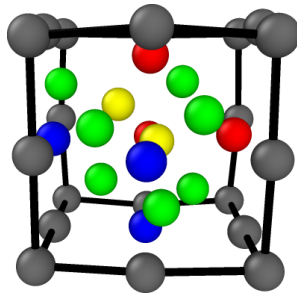
Figure 6.4 The fully relaxed structure of the embedded oxide NC with two helium interstitials initially centered around the oxide's octahedral interstitial location.

The charge density and ELF are shown in Figure 6.5 and provide insight to the electronic structure of the oxide NC embedded in Fe. The localized maxima in the charge density correspond to atomic nuclei and core electrons. The ELF quantifies the probability of finding two electrons in close proximity to one another and thus, low values of the ELF correspond to low electron localization (or possibly no charge) and high values of the ELF correspond to highly localized regions of charge. In regions corresponding to the Fe matrix, there exists a highly homologous charge density and low electron localization, consistent with a metallically bonded crystal. By comparison, the region of the charge density corresponding to the oxide NC contains spatially expansive regions of very low charge density and coupled with the electron localization, it is clear that little to no charge is present in the intermediate regions of the crystal where no Metal/oxygen bonding is occurring. This is highly representative of the more localized bonding arising from the iono-covalent Y-O and Ti-O bonds present in the oxide NC.
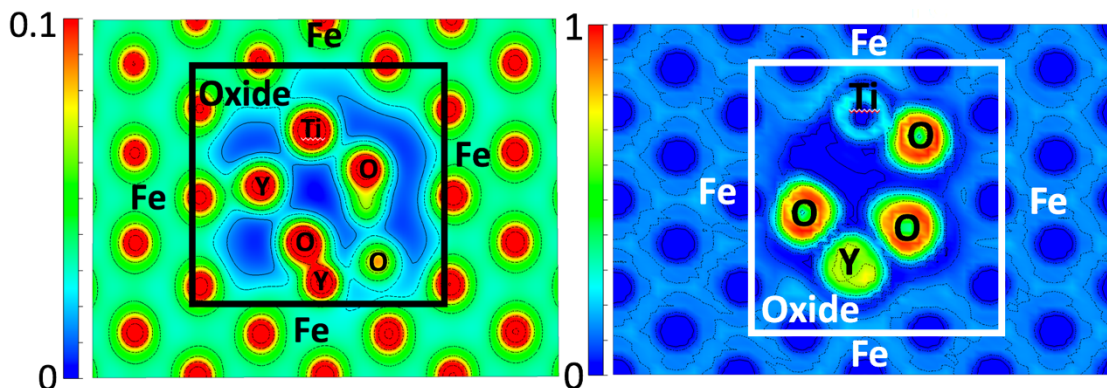
Figure 6.5 Charge density and ELF in the (1 -1 0) plane of the supercell.

The charge density and ELF when helium is located at the interface and at the octahedral interstitial location of the oxide NC are shown in Figure 6.6. In both cases, the helium interstitial is occupying the region of very low charge density that was found in Figure 6.5 that corresponds to the same region as the location of the oxide. Similar behavior is seen compared to what was shown in a previous DFT study [21] of helium in the bulk oxide, where the effects of the interaction

66

at the octahedral interstitial location are electron-electron repulsion between He and the constituent O atoms of the oxide, as shown by the ELF. At the tetrahedral location, there is an apparent balancing between the electron-electron repulsions of the He and the electron gas of the metallically bonded Fe and the valance shells of the nearby neighboring O atoms of the oxide. Thus, the tetrahedral interstitial location of the oxide (which is a vacant site in the pyrochlore structure) offers a significant amount of free volume for helium to exist. Similar results are seen for each of the interstitial locations surrounding the oxide where interstitial formation is relatively favorable (compared to Fe) due to the free space at each of the locations.
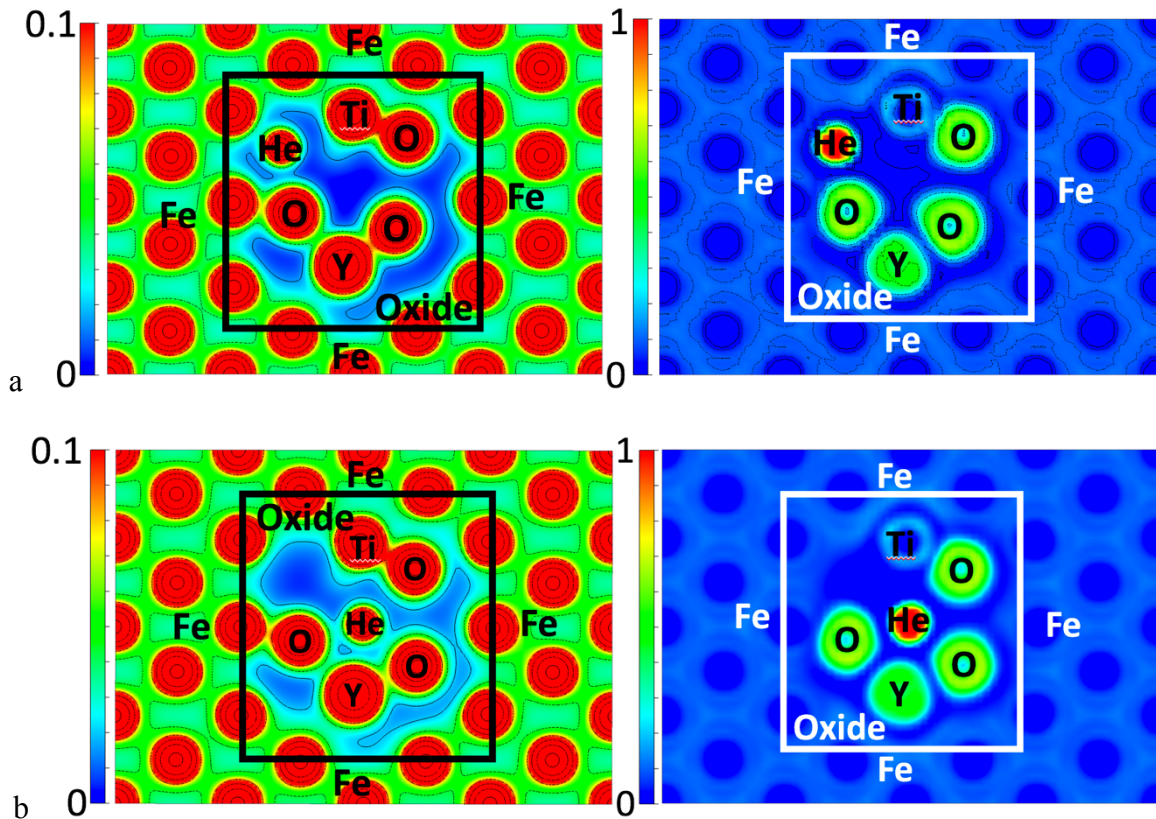
Figure 6.6 Charge density an ELF with helium located at a) the tetrahedral interstitial location of the interface and b) the octahedral interstitial location of the oxide NC

6.5.2   *Mapping of the Helium Potential Energy Landscape*

In order to further investigate the root cause of helium trapping at the $Y_2Ti_2O_7 -$ Fe interface, a mapping of the potential energy landscape has been created and compared to the charge

density and electron localization function (ELF) shown in Figure 6.5. The potential energy landscape has been calculated along the (1 -1 0) plane using an 8 x 8 mesh where the corners and edges of the mesh are defined by the oxide-Fe interface as shown in Figure 6.2. The mesh along this plane is largely symmetrically representative of the energy landscape of the interface where regions of significant free volume exist (i.e. presumably favorable helium nucleation sites). A helium atom is placed along each point of the 8 x 8 mesh and the nearest neighbor metal or oxygen atoms to the mesh-point are fully relaxed while the helium atom position is fixed. By subtracting the total energy of the system at the current mesh point from the reference energy of the helium-free oxide-Fe setup shown in Figure 6.1, the potential energy landscape was created with a spline interpolation of the energies along the 8 x 8 mesh. The same method was used for calculating the potential energy landscape in BCC Fe so that the extrema of the potential energy landscapes could be compared.
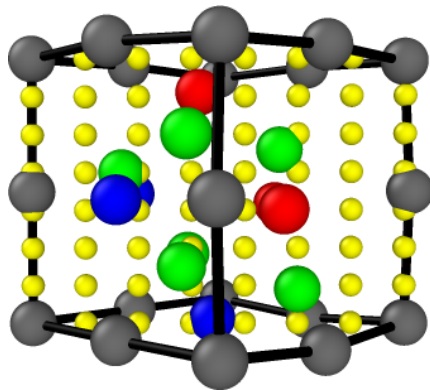
Figure 6.7 8 x 8 mesh used for the calculation of the potential energy landscape in the (1 -1 0) plane. The mesh of helium atoms is represented by the Yellow spheres.

The potential energy landscape for the (1 -1 0) plane of the oxide NC embedded in Fe, as well as the potential energy landscape along the (1 0 0) plane of BCC Fe are shown in Figure 6.3 (the (1 0 0) plane of Fe is used because this is the orientation at the Oxide NC). By comparing the extrema of the potential energy landscape calculations, it is shown that the potential energy maxima are larger in the oxide NC than in Fe, but the potential energy minima are lower than in

Fe. The maxima are localized to atomic positions corresponding to Y and O atoms, with Y and Fe being the most extreme. The potential energy minima that exist within BCC Fe are located at the tetrahedral interstitial locations, which has been previously calculated as the most stable He interstitial position in BCC Fe [26]. Although the potential energy maxima are higher in the Oxide NC, regions exist where there are potential energy-wells whose spatial extent is significantly larger than those present in BCC Fe. In addition, the well depths are approximately 4 eV lower than the well depths in Fe. The large spatial extent and increased well depth in the oxide makes the oxide a highly energetically favorable location for helium to accumulate.
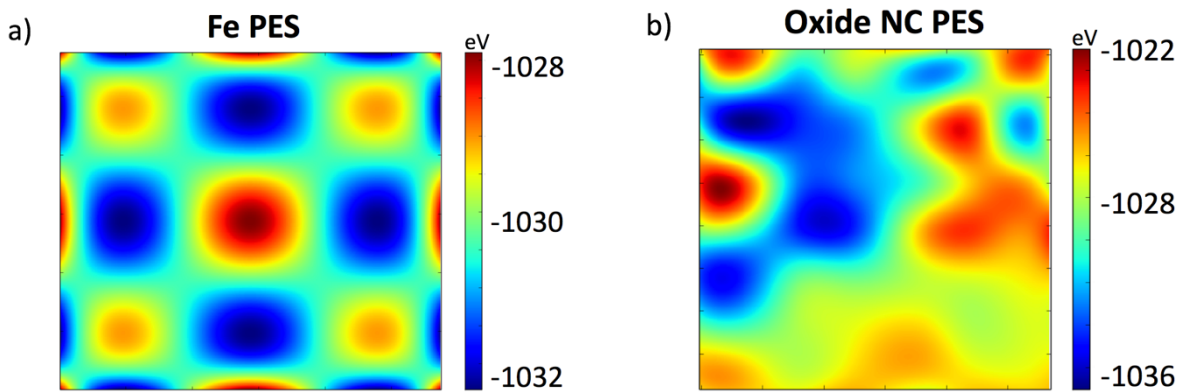
Figure 6.8 Potential energy landscape in the a) (100) plane of BCC Fe and b) (1-10) plane of the oxide NC embedded in BCC Fe.

6.6   Discussion

The formation energetics of helium interstitials and interfacial defects were found to be higher than those in a previous investigation [21, 23]. In addition, by comparison to an investigation of the $Y_2Ti_2O_7$/Fe interface [27] that found that the formation energetics of interfacial He defects were similar to those in the bulk oxide, the formation energies reported here are also higher. The potential reasons for this are that in the current work, a full relaxation of the supercell volume and shape was not performed in order to prevent significant distortion of the cell and to simulate the structural conditions as they would exist within the bulk alloy. Thus, there may be

strain effects that are coming into play that were not present when calculations were performed on the bulk oxide since the supercell volume is not allowed to change. Likewise, the stoichiometry of the oxide NC is not exactly $Y_2Ti_2O_7$, though the structure matches and thus, the energies can not be exactly compared between this study and the bulk oxide investigations. However, the energetics are still important in that they are significantly lower than helium formation energies in the Fe (far removed from the oxide NC) and since the reference energies for these calculations are the same, the conclusions are valid.

The favorability of $Y_2Ti_2O_7$ NCs as a helium trapping site in NFAs has become clear by investigating the potential energy landscape, the charge density, and the ELF. Upon implantation of He into the BCC Fe matrix, interstitial formation is highly energetically unfavorable (~4.5 eV) and the implanted species is capable of migrating with a very low energy barrier of 0.07 eV [26]. The inert helium atom's high solution energy in BCC Fe stems from the small spatial extent of the potential energy minima that exist within the electron gas of the metallically bonded BCC Fe. Thus, since no bonding occurs between the inert He atom and the bulk matrix, it can be inferred that the helium atom is repelled along the potential energy landscape of the BCC Fe matrix until it reaches a location in which there exists a potential energy-well. Examination of the potential energy landscape, and relating it to the charge density, shows that regions within the alloy with a low charge density correspond to potential energy-wells. Such regions of low charge density within NFAs could be comprised of vacancies or vacancy clsuters, voids, grain-boundaries, or, investigated in the current work, oxide nanoclusters. The localized ionic bonding present within the oxide NCs creates a region within the bulk that serves as a spatially expansive potential energy-well located within the Fe matrix making the oxide a highly favorable trapping site for helium.

NFAs contain a high number density of oxide NCs of varying compositions, such as Y_2O_3, Y_2TiO_5 and other Y-Ti-O non-stoichiometric compounds. Previous DFT investigations of helium in bulk Y_2O_3 and Y_2TiO_5 exhibit remarkably similar behavior to that of helium in $Y_2Ti_2O_7$ and would presumably have a potential energy landscape within Fe of a similar nature. Thus, the high number density of oxide nanoclusters within the alloy creates a high number density of potential energy-wells that prevent helium from reaching grain boundaries and voids and ultimately, the threat of swelling, cracking and embrittlement is significantly reduced. Localized iono-covalent bonding is characteristic of oxides and thus, it can be inferred that this trapping behavior would be exhibited by a wide array of oxide compositions. The key component to preventing helium from reaching grain boundaries is to have a secondary phase that provides a spatially expansive potential energy minimum as exhibited by the high number densities of oxide nanoclusters in NFAs. Knowing that the the substantial difference in the electronic structure of the oxide and Fe creates a high number density of potential energy-wells within the alloy opens the door for the investigation of alternative precipitate phases that may aid in addressing the challenges still posed by NFAs, such as the formability of large-scale reactor components.

6.7   Conclusions

The formation energetics and potential energy landscape of helium at a structure matched $Y_2Ti_2O_7$ oxide nanocluster embedded in BCC Fe was investigated using DFT. The investigation revealed that a potential energy landscape in the oxide that has a spatially extensive potential energy-well that makes helium trapping favorable. The potential energy-well arises due to localized iono-covalent bonding between the metal and oxygen atoms within the oxide. From this, the pronounced ability of oxide NCs within NFAs to act as trapping sites for helium is attributed to a high number density of potential energy-wells such as that found in this investigation.

6.8   Acknowledgements

References

[1] H. Trinkaus, B.N. Singh, Journal of Nuclear Materials, 323 (2003) 229-242.

[2] M.R. Gilbert, S.L. Dudarev, D. Nguyen-Manh, S. Zheng, L.W. Packer, J.C. Sublet, Journal of Nuclear Materials, 442 (2013) S755-S760.

[3] M.J. Alinger, G.R. Odette, D.T. Hoelzer, Journal of Nuclear Materials, 329–333, Part A (2004) 382-386.

[4] R.L. Klueh, P.J. Maziasz, I.S. Kim, L. Heatherly, D.T. Hoelzer, N. Hashimoto, E.A. Kenik, K. Miyahara, Journal of Nuclear Materials, 307–311, Part 1 (2002) 773-777.

[5] D.A. McClintock, D.T. Hoelzer, M.A. Sokolov, R.K. Nanstad, Journal of Nuclear Materials, 386–388 (2009) 307-311.

[6] P. Miao, G. Odette, T. Yamamoto, M. Alinger, D. Klingensmith, Journal of Nuclear Materials, 377 (2008) 59-64.

[7] G.R. Odette, M.J. Alinger, B.D. Wirth, Annual Review of Materials Research, 38 (2008) 471-503.

[8] J.H. Schneibel, M. Heilmaier, W. Blum, G. Hasemann, T. Shanmugasundaram, Acta Materialia, 59 (2011) 1300-1308.

[9] S. Ukai, T. Nishida, H. Okada, T. Okuda, M. Fujiwara, K. Asabe, Journal of Nuclear Science and Technology, 34 (1997) 256-263.

[10] M.K. Miller, K.F. Russell, D.T. Hoelzer, Journal of Nuclear Materials, 351 (2006) 261-268.

[11] Y. Wu, E.M. Haney, N.J. Cunningham, G.R. Odette, Acta Materialia, 60 (2012) 3456-3468.

[12] H. Kishimoto, M.J. Alinger, G.R. Odette, T. Yamamoto, Journal of Nuclear Materials, 329–333, Part A (2004) 369-371.

[13] S. Yamashita, K. Oka, S. Ohnuki, N. Akasaka, S. Ukai, Journal of Nuclear Materials, 307–311, Part 1 (2002) 283-288.

[14] M.C. Brandes, L. Kovarik, M.K. Miller, G.S. Daehn, M.J. Mills, Acta Materialia, 60 (2012) 1827-1839.

[15] T. Hayashi, P.M. Sarosi, J.H. Schneibel, M.J. Mills, Acta Materialia, 56 (2008) 1407-1416.

[16] J.H. Schneibel, C.T. Liu, M.K. Miller, M.J. Mills, P. Sarosi, M. Heilmaier, D. Sturm, Scripta Materialia, 61 (2009) 793-796.

[17] Q. Li, C.M. Parish, K.A. Powers, M.K. Miller, Journal of Nuclear Materials, 445 (2014) 165-174.

[18] P.D. Edmondson, C.M. Parish, Y. Zhang, A. Hallén, M.K. Miller, Scripta Materialia, 65 (2011) 731-734.

[19] P.D. Edmondson, C.M. Parish, Y. Zhang, A. Hallén, M.K. Miller, Journal of Nuclear Materials, 434 (2013) 210-216.

[20] G.R. Odette, P. Miao, D.J. Edwards, T. Yamamoto, R.J. Kurtz, H. Tanigawa, Journal of Nuclear Materials, 417 (2011) 1001-1004.

[21] T. Danielson, C. Hin, Journal of Nuclear Materials, 452 (2014) 189-196.

[22] T. Danielson, E. Tea, C. Hin, Journal of Physics D: Applied Physics, 49 (2016) 065301.

[23] L. Yang, Y. Jiang, G. Robert Odette, T. Yamamoto, Z. Liu, Y. Liu, Journal of Applied Physics, 115 (2014) 143508.

[24] P. Erhart, Journal of Applied Physics, 111 (2012) 113502.

[25] Y. Jin, Y. Jiang, L. Yang, G. Lan, G. Robert Odette, T. Yamamoto, J. Shang, Y. Dang, Journal of Applied Physics, 116 (2014) 143501.

[26] C.-C. Fu, F. Willaime, Physical Review B, 72 (2005) 064117.

[27] L. Yang, Y. Jiang, Y. Wu, G.R. Odette, Z. Zhou, Z. Lu, Acta Materialia, 103 (2016) 474-482.

[28] L. Barnard, G.R. Odette, I. Szlufarska, D. Morgan, Acta Materialia, 60 (2012) 935-947.

[29] C.L. Fu, M. Krčmar, G.S. Painter, X.-Q. Chen, Physical Review Letters, 99 (2007) 225502.

[30] G. Kresse, J. Hafner, Physical Review B, 47 (1993) 558-561.

[31] G. Kresse, J. Hafner, Physical Review B, 49 (1994) 14251-14269.

[32] G. Kresse, J. Furthmüller, Computational Materials Science, 6 (1996) 15-50.

[33] G. Kresse, J. Furthmüller, Physical Review B, 54 (1996) 11169-11186.

[34] P.E. Blöchl, Physical Review B, 50 (1994) 17953-17979.

[35] G. Kresse, D. Joubert, Physical Review B, 59 (1999) 1758-1775.

[36] J.P. Perdew, K. Burke, M. Ernzerhof, Physical Review Letters, 77 (1996) 3865-3868.

[37] J.P. Perdew, K. Burke, M. Ernzerhof, Physical Review Letters, 78 (1997) 1396-1396.

[38] J. Ribis, Y. de Carlan, Acta Materialia, 60 (2012) 238-252.

PART II - Addressing Challenges Associated with Kinetic Monte Carlo Simulation of Complex Chemical Reaction Networks

7.   Introduction

Accurate predictive multi-scale modelling of chemical reaction networks is a critical tool for the development of novel catalysts. One promising approach for predictive modelling, particularly for the case of a gas flow reactor experiment, is the coupling of density functional theory (DFT), kinetic Monte Carlo (KMC), and computational fluid dynamics (CFD) simulations. DFT provides accurate parameterization of kinetic parameters and is fed to KMC simulations. KMC is then used to simulate localized surface or crystal kinetics for millions of conditions of interest and serves as input to CFD simulations. CFD serves as the final link in the scales of simulation to reach the macro-scale output flux of product gases. When performed accurately and rigorously, this type of multi-scale modelling method is capable of reproducing experimental conditions with high accuracy and can not only serve to save laboratory time and materials, but also aid in the prediction of novel catalysts of interest. However, for complex chemical reaction networks, the overall computational cost of developing rigorous multi-scale models can become intractable, where a significant portion of this computational expense arises in the KMC step. The two main culprits for the computational expense of KMC simulations are the potential for small time steps (relative to the simulation time scale of interest) and the need for simulation of millions of input conditions to reproduce macro-scale behavior.

Stochastic Kinetic Monte Carlo simulations are capable of simulating chemical reaction networks with high accuracy due to the fact that the simulations are governed by the reaction rate constants of different reaction processes. Thus, the statistical sampling of chemical reaction processes within the simulations matches the statistical occurrence of reactions in reality. However, while the kinetics of the system are nearly perfectly reflective of reality, they also serve as a hurdle in large chemical reaction networks where large disparities between the fastest and

slowest processes' rate constants exist. When the difference between the rate of occurrence of the fastest and slowest process of a chemical reaction network spans many orders of magnitude, the simulation is prone to spending an excessive amount of time in a quasi-equilibrium state with time steps that are only a small fraction of the time scale of interest (where the time scale of interest is the time it takes to reach a true steady-state). When the steady-state behavior of the system is the primary interest, these large disparities in the reaction rate constants serve as a major hurdle for KMC simulation of complex chemical reaction networks and consequently, the coupling between DFT and CFD.

Additionally, the statistical accuracy of a KMC simulation is dependent upon not only the accurate parameterization of the model, but also the simulation size. Simulations of a macro-scale sized sample would be capable of perfectly reproducing experimental conditions, but would be computationally infeasible, and thus, simulations are typically on the order of hundreds to millions of sample unit cells, depending on the crystal system of interest. As a result of the limitations on simulation size, millions of simulation input (gas pressures, temperatures, initial surface coverage, etc.) conditions are required to provide the necessary output data for CFD simulations. For each set of input conditions, the system's steady-state will be reached at a different time. In some cases, the necessary simulation time for two different sets of input conditions may be quite similar and in others, drastically different, but there is no efficient way to predict this *a priori*. Thus, in order to efficiently simulate the array of input conditions to produce a macro-scale model, an efficient on-the-fly method for detecting steady-state is necessary. In addition, strict criteria are required so that steady-state is not triggered by a quasi-steady-state. Detection of steady-state on-the-fly removes the necessity for the simulator to confirm steady-state or predict the required number of

simulation steps, while also allowing one simulation to finish and immediately begin the next set of input conditions.

In the following chapters, the KMOS KMC algorithm utilized in the current work, as well as a thorough description of two algorithms developed for the treatment of large disparities in reaction rate constants and on-the-fly detection of steady-state, will be provided. The algorithm for the treatment of large disparities in rate-constants has been developed in a versatile way and thus, it can be applied not only to KMC simulations of chemical reaction networks, but any KMC simulation where large disparities in probabilities of occurrence exist. Likewise, the on-the-fly window-based steady-steady state detection algorithm is applicable to essentially all scenarios where accurate detection of steady-state is necessary. Along the way, it was found that another technique could be offered to the experimental and computational chemical kinetics community for determining adsorption isotherms in a generalized way that is only dependent upon the geometry of the surface and the adsorption process. From this, an additional study has been performed to develop a functional form for adsorption isotherms on two distinct surface geometries: the (111) fluorite surface and the (100) perovskite surface. The method used here provides many advantages over analytically determining the surface coverage at a given isotherm, and provides a simple explanation of the technique so that it can be duplicated for any surface geometry, independent of species.

8. SQERTSS: Dynamic Rank Based Throttling of Transition Probabilities in Kinetic Monte Carlo Simulations

The following manuscript has been submitted to Computer Physics Communications and is

currently under review.

8.1 Abstract

Lattice based Kinetic Monte Carlo (KMC) simulations offer a powerful simulation technique for investigating large reaction networks while retaining spatial configuration information, unlike ordinary differential equations. However, large chemical reaction networks can contain reaction processes with rates spanning several orders of magnitude. This can lead to problems similar to stiffness during KMC simulations, where the computational expense has the potential to be overwhelmed by relatively short time steps with the simulation spending an inordinate amount of steps/cpu-time simulating fast frivolous processes (FFP) without progressing the system (reaction network). In order to achieve simulation times that are experimentally relevant, a dynamic throttling algorithm involving separation of the processes into speed ranks based on event frequencies has been designed and implemented with the intent of decreasing the probability of occurrence of FFPs, and increasing the probability of occurrence of slow processes, allowing slower occurring events to become more likely. This Staggered Quasi-Equilibrium Rank-based Throttling for Steady State KMC simulations (SQERTSS-KMC) is designed for use in achieving and simulating steady state conditions. As shown in this work, the SQERTSS-KMC algorithm also works for transient conditions: the correct configuration space and final state will still be achieved if the required assumptions are not violated, with the caveat that the time dependent behavior may be distorted for transient conditions.

8.2 Authors and Affiliations

Thomas Danielson[1], Celine Hin[1,2], Aditya Savara[3]

Corresponding Author: Aditya Savara, savaraa@ornl.gov

[1]Department of Materials Science and Engineering, Virginia Polytechnic Institute and State University, Blacksburg, VA, USA

[2]Department of Mechanical Engineering, Virginia Polytechnic Institute and State University, Blacksburg, VA, USA

[3]Chemical Sciences Division, Oak Ridge National Laboratory, Oak Ridge, TN, USA

8.3   Introduction

Lattice based kinetic Monte Carlo (KMC) serves as a powerful and widely used computational technique for investigating the stochastic spatio-temporal evolution of atomic and molecular systems, e.g. catalytic chemical reactions on crystalline surfaces [1-11]. The technique transitions a system from an initial configuration to a subsequent configuration, where the subsequent configuration is selected using a random number and a probability weighted by the available transition probabilities (e.g. the reaction rate constants, in the case of a chemical reaction network). By comparison to solutions of ordinary differential equations, KMC provides the advantage of being able to obtain localized, site-specific reaction information. However, the computational expense of lattice based KMC has the potential to become intractable when the event frequencies of the different reaction events (e.g. diffusion, dissociation, association, adsorption, desorption, etc.) span many orders of magnitude such that the time steps are dominated by the fastest processes. As a result, using KMC to simulate experimentally relevant simulation times ($\sim 10^4$ s) for complex chemical reaction networks poses a challenge as the network is prone to spending many steps simulating fast frivolous processes (FFP) with very small time increments (i.e. similar to stiffness in ODEs). A FFP is defined here as rapid process which does not significantly progress the reaction network towards its steady-state (e.g.H^+ hopping back and forth between neighboring O^{2-} atoms). The FFPs that are mediated in this work are a subset of the quasi-equilibrated (QE) processes: we call a process QE when the forward and reverse rates are equal or

approximately equal and may not be reflective of a Boltzmann distribution across the states present in the system (we do not attempt to identify whether a QE process is actually at equilibrium, so what we refer to as QE processes may include equilibrium processes as well). Additionally, various processes have significantly lower transition probabilities making them rarely occurring events. These rare events may be important for transitioning the reaction network to its steady-state, however, the occurrence of rare events takes a substantial number of KMC steps to reach even a single occurrence when FFPs are present.

Various formulations have been developed to address the issue of simulating long time scales, relative to the processes being simulated, using KMC. Many methods treat the occurrence of a FFP as a localized energy basin [12-17]. The probabilities of the system evolving to a state outside of the basin, and the respective escape time for different paths out of the energy basin, are calculated. The most probable state becomes the current configuration and the time is progressed based on the mean escape time. In many cases, such an approach is considered to be exact in preserving the underlying kinetics of the system. An alternative approach is the τ-leap method [18-23]. Within the τ-leap approach, reactions are executed several times and the simulation time is advanced by coarser time increments than the standard microscopic time step. While these approaches are suitable for simple systems (e.g. diffusion of point defects), its utility for investigating a complex chemical reaction network on a lattice is limited by the ability to predict the configurations (especially rare configurations) which may be the most probable state outside of the energy basin. It is not possible to predict which of these configurations would be accessible *a priori*. Likewise, the computational expense of the basin hopping formulations scales increasingly with the number of processes and possible outcomes. Thus, for simulations containing many reaction processes and many possible configurations, an alternative method is needed, and

must be able to simulate long time scales in an efficient manner. The approach we use below is chosen specifically for addressing this problem in the context of complex chemical reaction networks with FFPs, though it may be applicable to other systems where basin hopping is not feasible for the same reasons.

We use an alternative approach, Staggered Quasi-Equilibrium Rank-based Throttling for Steady State KMC (SQERTSS-KMC), which circumvents the complication of FFPs, rare events and rare configurations by dynamically throttling the transition probabilities of reaction processes based on the KMC output of the reaction rates. In this context, throttling refers to speeding up or slowing down a particular process (in the context of KMC, this means as a function of the event frequency). The dynamic throttling of transition probabilities is similar to solving stiff ODEs by combining the Quasi Steady-State Approximation [24-26] and dynamic time-step methods[27] which assume a separation of time scales (classified by speed ranking), here in the context of an asymptotic approach to steady-state for various reactions on the time-scale of interest. Within the SQERTSS approach, FFPs will become less likely to occur and slower events will become more likely to occur resulting in a faster approach to the steady-state of the reaction network while maintaining kinetically appropriate ratios between transition probabilities when computationally feasible. This approach also enables appropriate timescales to be simulated once steady-state is reached, with the accuracy that is ultimately achieved based on the computational resources available. A similar method is net event KMC, [28] in which fast reversible processes are lumped together as one and the net rate is determined by the difference in the forward and reverse process. While net event KMC successfully improves the computational expense of KMC simulations while maintaining the relative probabilities of occurrence between forward and reverse processes, it does not maintain the staggering of the event frequencies between processes of different speed

ranks (described in sections 3 and 4), which can affect the paths accessed and consequently the chemical selectivity in complex reaction networks. The methodology we used is designed to retain the chemical selectivity even for complex chemical reaction networks, even for many cases where net event KMC would not.

After describing the methodology we used, we present results where the dynamic throttling algorithm has been applied to sample reaction networks with physically realistic parameters. We find that this algorithm behaves as anticipated, and is practical.

8.4   Computational Methods

The reaction network has been investigated using the lattice Kinetic Monte Carlo (KMC) framework as implemented in the program KMOS, which was developed by Hoffman and Reuter as a general purpose code for lattice kinetic Monte Carlo simulations encompassing multiple chemical reactions [29]. The current section will outline the Lattice KMC framework that has been used to investigate the reaction network, the simplified reaction network that has been implemented for testing, the dynamic throttling algorithm and an exhaustive list of the assumptions and approximations made by throttling.

8.4.1   Lattice kMC formulation

The KMC formulation discussed here will be in the context of a catalytic chemical reaction on a crystal surface where there exists a set of well-defined unique reaction sites (e.g. atomic surface sites or intermediate reaction surface sites) and associated reaction processes that can occur. The crystal surface can be repeated through space with the use of periodic boundary conditions and each surface site has the potential of becoming occupied by some species with an associated probability defined by the reaction rate constant for a particular reaction process. The surface, and the associated species on the surface, define a configuration at a particular point in

time. Kinetically, the stochastic evolution of the surface configuration through time follows a Markovian master equation:

$$\dot{\rho}_u(t) = \sum_v (w_{uv}\, \rho_v(t) - w_{vu}\rho_u(t)) \tag{1}$$

where, $\rho_u(t)$ is the probability for the system to be in configuration u at time t, and w_{vu} is the transition rate that configuration u transitions to configuration v. In order to compensate for the computational expense of solving the Markovian master equation, the KMC algorithm generates an ensemble of trajectories in order to propagate the surface configurations through time such that, the average over the entire ensemble of trajectories yields the probability densities of the underlying Markovian master equation.

The way in which time is propagated in KMC simulations can vary based on the computational needs. Within the current work, the variable step-size method (VSSM) has been used. The VSSM emerges from the basis that the waiting times for n uncorrelated events that occur with transition rate, k, follow a Poisson distribution as:

$$p_n(k, \Delta t) = \frac{(k\Delta t)^n e^{-k\Delta t}}{n!} \tag{2}$$

From this, the waiting time between two events is given by the case that no events occur:

$$p_o(k, \Delta t) = e^{-k\Delta t} \tag{3}$$

Using a uniform random number, $r \in (0,1]$:

$$\Delta t = \frac{-\ln(r)}{k_{total}} \tag{4}$$

Where, k_{total} is the sum of all rate constants for all processes that can occur within the current configuration (For a more rigorous derivation of the VSSM see refs [29-33]). Thus, the step-size is variable due to the fact that the number of processes available to occur in each configuration is variable. Within the VSSM, the event which occurs in a given instant is selected using a random number and the sum of all available process transition rates as:

83

$$\sum_v^{j-1} k_{vu} < r k_{tot,u} \leq \sum_v^j k_{vu} \tag{5}$$

The most relevant KMC output when investigating the occurrence of various reaction events at any given step in the simulation is the turnover frequency. Within the KMC framework, the turnover frequency (i.e. the number of times an event happens per unit cell per second) for a given process can be calculated across a given time interval as:

$$TOF_a = \frac{M}{\Delta t} \tag{6}$$

Where, M is the number of times process a has occurred during the time interval Δt (for example, this could correspond to the number of times a molecule is produced for a particular species such as CO or CH$_3$OH).

To summarize, the KMC algorithm can stated as follows:

1. Initialize lattice at $t = 0$

2. Update list of available processes and their associated transition rates to calculate $k_{total} = \sum k$

3. Draw two random numbers on the interval $(0,1]$

4. Select an event that satisfies equation 5

5. Update lattice configuration according to the event which occurs

6. Update time according to equation 4

8.4.2 *Chemical reactions*

The following section will outline the simplified reaction network that has been simulated using KMC in order to test the dynamic throttling algorithm. The reaction network is a simplified reaction network that begins with methanol adsorption on a CeO$_2$ (111) surface and results in output fluxes of formaldehyde, H$_2$ and methanol through various reaction processes.

8.4.3 *Methanol adsorption on CeO₂ (111)*

The simplified reaction network imposes an initial input flux of methanol gas on a defect free CeO$_2$ (111) surface. The CeO$_2$ (111) surface has three distinct site types: Ce, O and an intermediate bridge site for methanol adsorption processes. This simulates methanol being continuously exposed to the surface at a pressure of 1 bar, although the pressure simply serves as a parameter for the adsorption rate constant and no gas phase is explicitly present. Since the surface is initially uncovered by any species and methanol is the only input gas, the first process to occur in this simulation is methanol adsorption. The transition probabilities for adsorption processes can be defined as:

$$k_{Ads} = \frac{P}{\sqrt{2\pi k_B T M}} e^{\frac{-E_A}{RT}} \tag{9}$$

where, P is the input pressure of the gas, k_B is the Boltzmann constant, T is the temperature, M is the molecular mass, E_A is the activation energy for adsorption and R is the gas constant.

The reaction pathway has been tailored to result in output fluxes of methanol, H$_2$ and formaldehyde. Reaction processes within the simplified reaction network include: adsorption, desorption, association and ionic dissociation as outlined in Table 8.1. The transition probabilities for desorption, associative and dissociative processes can be defined as:

$$k = A e^{\frac{-E_A}{RT}} \tag{10}$$

Where, A is the pre-exponential factor, E_A is the activation energy for the reaction process, R is the gas constant and T is the temperature.

Table 8.1 Reaction processes within the sample reaction network. Reactions containing a "↔" indicate that there is both a forward and reverse reaction process listed and transition probabilties are listed in the same order. Reactions containing a "→" indicate that only one direction exists.

Reaction Number	Reaction Name	Chemical Equation	Forward Rate Constant (s^{-1})	Reverse Rate Constant (s^{-1})
1	H_2 Production	$2(H^* -- Ce^{4+} -- O^{2-}) \rightarrow$ $H_2(g) + 2\ Ce^{4+} -- O^{2-}$	1.28×10^{11}	-
2	H* production/reduction	$Ce^{3+} -- O^{2-} -- H^+ \leftrightarrow$ $H^* -- Ce^{4+} -- O^{2-}$	3.62×10^{11}	8.534×10^{14}
3	H^+ Hopping between Ce^{3+} and Ce^{4+}	$Ce^{4+} -- O^{2-} -- H^+ + Ce^{3+} -- O^{2-} \leftrightarrow$ $Ce^{4+} -- O^{2-} + Ce^{3+} -- O^{2-} -- H^+$	4.53×10^{12}	2.05×10^{12}
4	H_2O Molecular Desorption	$H_2O -- Ce^{4+} -- O^{2-} \rightarrow$ $H_2O + Ce^{4+} -- O^{2-}$	3.9×10^{10}	-
5	H_2O ionic association/dissociation	$H_2O -- Ce^{4+} -- O^{2-} + Ce^{4+} -- O^{2-} \leftrightarrow$ $OH^- -- Ce^{4+} -- O^{2-} + Ce^{4+} -- O^{2-} -- H^+$	4.53×10^{12}	1.28×10^8
6	OH^- hopping in/out of vacancy	$OH^- -- Ce^{4+} -- O^{2-} + Ce^{3+} -- []^0 \leftrightarrow$ $Ce^{4+} -- O^{2-} + Ce^{3+} -- O^{2-} -- H^+$	4.53×10^{12}	1.95×10^6
7	H_2O hopping in/out of vacancy	$H_2O -- Ce^{4+} -- O^{2-} + Ce^{3+} -- []^0 \leftrightarrow$ $H_2O -- Ce^{3+} -- []^0 + Ce^{4+} -- O^{2-}$	4.53×10^{12}	6.25×10^{11}
8	Methanol Adsorption/Desorption	$CH_3OH(g) + 2\ Ce^{4+} -- O^{2-} \leftrightarrow$ $Ce^{4+} -- O^{2-} -- CH_3OH -- Ce^{4+} -- O^{2-}$	8.03×10^6	2.30×10^{11}
9	CH_3OH ionic dissociation/association	$Ce^{4+} -- O^{2-} -- CH_3OH -- Ce^{4+} -- O^{2-} \leftrightarrow$ $CH_3O^- -- Ce^{4+} -- O^{2-} + Ce^{4+} -- O^{2-} -- H^+$	2.30×10^{11}	1.23×10^8
10	H abstraction from ionic CH_3O	$CH_3O^- -- Ce^{4+} -- O^{2-} + 2\ Ce^{4+} -- O^{2-} \rightarrow$ $CH_2O -- Ce^{4+} -- O^{2-} + Ce^{3+} -- O^{2-} + H^* -- Ce^{4+}$ $-- O^{2-}$	4.53×10^9	-
11	H abstraction from ionic CH_3O on a vacancy	$(CH_3O^-) - Ce^{3+} -- [\ ]^0 + 2\ Ce^{4+} -- O^{2-} \rightarrow$ $(CH_2O) -- Ce^{3+} -- [\ ]^0 + H^* -- Ce^{4+} -- O^{2-} +$ $Ce^{3+} -- O^{2-}$	4.53×10^9	-
12	Ionic CH_3O migration	$Ce^{4+} -- O^{2-} + (CH_3O^-) -- Ce^{3+} -- [\ ]^0 \leftrightarrow$ $CH_3O^- -- Ce^{4+} -- O^{2-} + Ce^{3+} -- [\ ]^0$	6.89×10^7	9.28×10^{11}
13	CH_2O Desorption	$Ce^{4+} -- O^{2-} -- CH_2O \rightarrow$ $CH_2O + Ce^{4+} -- O^{2-}$	7.39×10^9	-
14	CH_2O Desorption from Vacancy	$CH_2O - Ce^{3+} -- [\ ]^0 \rightarrow$ $CH_2O + Ce^{3+} -- [\ ]^0$	5.88×10^7	-

The activation energies and pre-exponential factors for the transition probabilities have been carefully selected from existing density functional theory and experimental literature.[34]

The simulation size consists of 400 unit cells, corresponding to a surface with dimensions of 38.25 x 66.26 Angstroms. Simulations have been run until a steady-state TOF has been reached.

8.5   Throttling Algorithm

The dynamic throttling algorithm is designed to decrease the occurrence of fast frivolous processes and increase the occurrence of slower processes by using the classifications of FFPs (QE processes), non-QE processes and the fastest rate-limiting process (FRP). In doing so, the intention is to compress the simulation time scale in order to reach the reaction network's steady-state, achieving experimentally relevant simulation times, with increased computational efficiency and without significantly altering the underlying kinetics. Within this framework, more compression will imply higher levels of approximation and thus, decreased accuracy of the kinetics. The main assumption here is that the occurrence of FFPs, such as H^+ hopping back and forth between two adjacent O^{2-} atoms, does not significantly affect the local reaction kinetics nor progress the system towards steady-state.

We first define a FFP as any reaction process whose forward and reverse reactions (e.g. H^+ hopping in one direction and hopping in the opposite direction or adsorption and desorption) have the same event frequency (measured in **events $*$ s^{-1} $*$ #unit cells^{-1}**). In order to decrease the occurrence of the FFPs, a throttling factor that is less than or equal to one is determined with respect to the other event frequencies within a particular KMC snapshot (a snapshot is a grouping of sequential KMC steps which returns the average event frequency for each process) and applied to the transition probability (the KMC process rate constant, in this case). The benchmark for throttling is chosen as the FRP. By using the FRP, the distortion of the time steps within the VSSM is limited, whereas if the slowest rate limiting process was used, there would be large distortions to the KMC time, where the time steps would become significantly larger. In a similar fashion, the slower processes can be throttled up (e.g. a throttling factor greater than or equal to 1) towards the

FRP. However, in order to minimize the distortion to the underlying kinetics, the FFPs are always throttled down before any of the slow processes are throttled up.

Since the goal is to increase the computational efficiency of achieving KMC simulation times that have experimental relevance (on the order of hours, in this case), different scales of throttling have been implemented, which represent different extents of throttling. As mentioned previously, the FFPs are always throttled before any of the slow processes. Once the FFPs have been throttled, the range of orders of magnitude for the event frequencies of relevant processes is calculated in order to determine whether or not the slowest process would be likely to occur at least one time in a computationally feasible number of steps. If this criterion is not met, the slow processes are throttled as well. Thus, the scale of throttling is not necessarily the same between the FFPs and the slow processes. For the KMC simulations in this study, it was determined that if the slowest process occurred on the order of once per one million configuration steps, that detecting significant changes in the system would be computationally feasible.

The throttling here depends on categorizing and sorting the different types of processes according to their speed ranking. There are two forms of ranking that we use. In paired ranking, scaling and throttling are applied in such a way that the ratios between the forward and reverse processes are maintained (i.e., the rank consists of a pair of forward and reverse processes), then the process rank can be defined as the next fastest (or slowest) reaction pair. In unpaired ranking, scaling and throttling are applied in such a way that the relative staggering between all processes is maintained, the process rank is defined as the next fastest (or slowest) process. The concept of the rank is further illustrated in Figure 8.1.
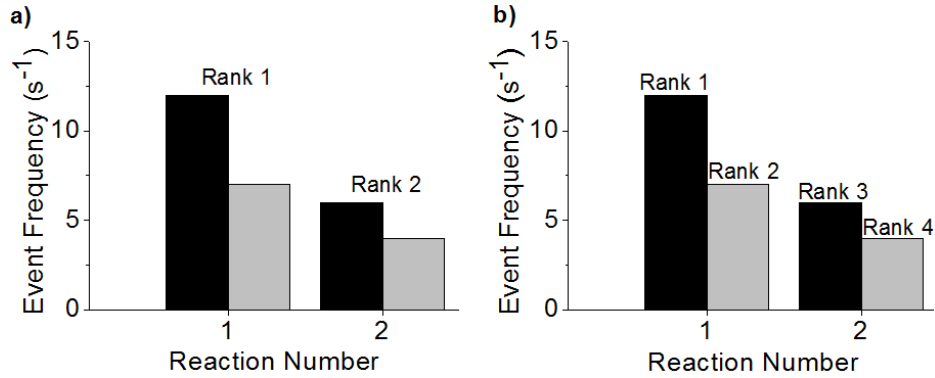
Figure 8.1 Process ranks for a) paired and b) unpaired throttling. Forward and reverse processes are shown in black and grey respectively.

Another important concept for this algorithm is the "event frequency range", which is defined as the event frequency of the fastest speed rank divided by the event frequency of the lowest speed rank. Given speed ranks, the event frequency range can be expressed in a general form as $N_{Sites} * C^P$, where P is the process rank. The size of the event frequency range for each of the scalings used in the current study are defined as follows for increasing extent of compression:

1. N_{Sites}^{P+1}

2. $N_{Sites} * C^P$

3. $N_{Sites} * 1.1^P$

where N_{Sites} is the number of sites in the simulation, P is the number of process ranks and C (10 in the current work for scale 2) is a user defined constant that allows for increased compression compared to the N_{Sites}^{P+1} scaling. In the current study, three orders of compression were used: N_{Sites}, 10, and 1.1. Assuming that every process has an event frequency greater than N_{Sites} x EF^i, where EF^i is the next slowest process event frequency. For example, if the same scaling is applied to the FFPs and the slow processes, the three different scalings would have the following structure (further illustrated in an example in Figure 8.2):

- N_{Sites}^{P+1} – A staggering of the process event frequencies from slow to fast, where each process rank is separated by a factor of N_{Sites}.

- $N_{Sites} * C^P$ - A staggering of the process event frequencies from slow to fast, where each process rank is separated by a factor of C.

- N_{Sites} - A staggering of the process event frequencies from slow to fast, where each process rank is separated by a factor of *1.1*.

Scale 1, 2 and 3 can be applied in two different ways: by preserving the ratio between the forward and reverse process (paired ranking) or by preserving the relative staggering between all fast and slow processes (unpaired ranking). The method that gives the highest accuracy and meets the required compression criteria is used.

The following approximations and assumptions have been made which must be fulfilled or distortions of the system behavior will occur. All of these approximations and assumptions will usually be valid, enabling this algorithm to be quite general:

- The minimum factor of throttling is chosen to be N_{Sites} , where N_{Sites} is the number of sites present in the slab on which a reaction can occur, such that scaling a process to within N_{Sites} beyond the next fastest rank leaves the opportunity for the faster of the processes to take place on each of the sites at least once before processes of the next fastest rank (i.e., process rank 1 has the opportunity to completely change the nature of the surface between each execution of anything from process rank 2).

- Throttling is performed with respect to the FRP in order to maintain the least amount of distortion to the variable time steps; this is because the FRP determines the rate of production of the major product in a steady-state system. If we throttled with respect to

any of the slower RPs, we would more significantly distort the time steps and the rate of production of the major product.

- Slow processes are always throttled with the most accurate possible method. This is because the slow reactions' forward and reverse process are generally not in QE with one another and thus, systemic changes are still being driven by these processes. The fast processes, on the other hand, rapidly achieve a quasi-pre-equilibrium and thus, no significant changes in the reaction system are driven by the processes *provided* that the FFP retain QE by having rates approximately equal to each other (this requirement is preserved in our algorithm).

- Only slow processes are unthrottled after a given number of steps. All throttling factors for FFPs are applied all the way through the simulation. This algorithm is valid under the assumption that any change in rate of a QE FFP is only marginal in a given time step -- such that any departure from QE is gradual and also that any changes in the staggering are gradual. What is marginal can be defined.

    If we have departure from QE for the rates of forward and reverse process of reaction *i* between two time steps (snapshots) *t* and *t+1* we can express the change in rate as:

$$\Delta R_i = R_i^t - R_i^{t+1}$$

    And similarly, the staggering S_i^t can be defined as the *ratio* of two adjacent processes ranks (*i* and *i+1)* at a given time step *t,* when ordered from least to greatest. So the change in the staggering between two snapshots can be expressed as:

$$\Delta S_i = S_i^t - S_i^{t+1}$$

From the above definitions, we see that the marginal change assumption is fulfilled when $\Delta R_i \ll \Delta S_i$ between any two snapshots. For this reason, it is recommended that when implementing a dynamic throttling code to use scaling that has a minimum value of C no lower than 1.1 because this implies that only changes greater than ten percent of the rate in a given snapshot would risk violating the assumption of marginal change.

- If a given process rank occurs less than N_{Sites} times in maximum relevant simulation time (MRST), which is 10 hours in the test case presented here, no throttling is applied to that process rank at the current step. These processes are considered "negligibly slow" because these processes are so slow that they could not drive significant change of the system at the current time nor be significant participants in the primary reaction pathway. In addition, if extremely slow poisoning processes happen to be autocatalytic, the risk of poisoning the surface would increase by making the reactions occur more frequently. The choice of maximum relevant simulation time is based upon the reactor timescales that are relevant to the system of study, and the choice for will thus be system specific.

When the KMC simulation gets in to a metastable state where only QE processes exist, there are two possible ways that it can exit that state: 1) by the configuration entering into a rare configuration for a non QE process to occur and 2) having a rare non QE process occur. We do not have a way of predicting which exit path the simulation will take to have a non QE process occur. In such a state, the configuration space that the simulation is traversing remains the same, regardless of the transition probabilities (because we have only QE processes). Thus, it becomes necessary to decrease the QE transition probabilities in order to increase the relative likelihood of a rare process occurring in order to exit the current state. However, if we decrease the transition

probabilities significantly, the time steps can become highly distorted (due to use of the VSSM), and as a result, the event frequencies become distorted (i.e. we will have the same number of events occurring, but the time steps will be significantly different). Thus, we implement a floor value for the throttling of QE processes of 10^6 s^{-1} and once the slowest QE process transition probability reaches this limit, we do not throttle further until a rate limiting process exists.

The SQERTSS algorithm has been applied to a set of event frequencies that span 35 orders of magnitude shown in Figure 8.2. It is clearly shown that the compression increases from scale 1 to scale 3. In all cases the ratios of the forward and reverse process are maintained. In some cases, such as process number 3, there is no change in the event frequency. This is applied when the event frequency is not a factor of N_{Sites} less than the FRP. Although these event frequencies are not realistic for a chemical reaction network, it clearly illustrates how the algorithm is applied to the event frequencies and the resulting compression from applying the algorithm.
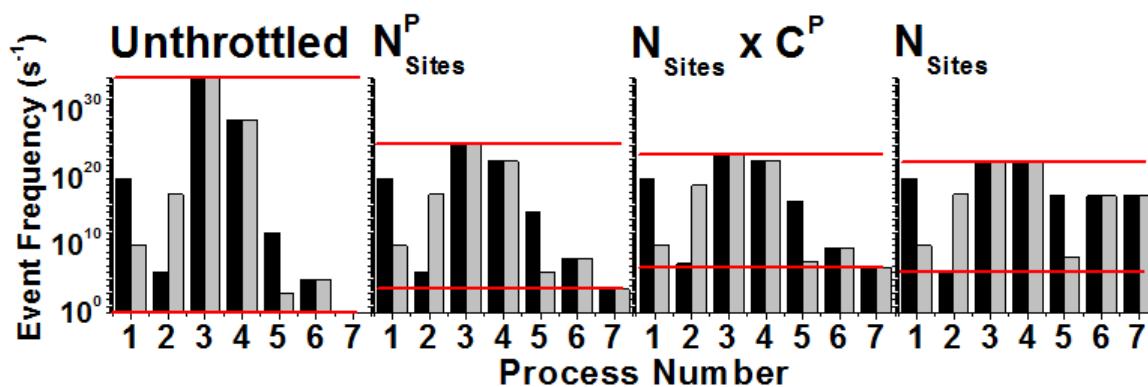
Figure 8.2 Throttling scales applied to sample event frequencies. Black and grey bars represent forward and reverse processes respectively. The throttling scale used is indicated above each chart. The red horizontal lines are used to illustrate the difference in compression between the different scalings.

The complete throttling algorithm, in its dynamic form, takes the following structure:

1. Run an initial KMC snapshot with no throttling applied

2. Gather process event frequencies from initial snapshot. At this step and every subsequent step, the event frequencies are checked to be above the threshold of being

negligibly slow. For any given snapshot, any process with an event frequency that is below the threshold of being negligibly slow is not throttled and is not included in the calculation of the throttling factors.

3. Check the separation in orders of magnitude of the fastest and slowest event frequency

    a. If QE and non QE process event frequencies exist

        i. If the event frequency range is small enough such that all processes are likely to occur at least once within a computationally feasible number of steps, run another unthrottled snapshot

        ii. Else, identify FRP, for i in range(1,3), throttle FFPs with Scale i, leave process ranks slower than the FRP unthrottled while throttling FFPs until event frequency range is small enough such that all processes are likely to occur at least once within a given number of steps, or until i = 3.

            1. If i = 3 and range is not small enough for all processes to occur at least once within a computationally feasible number of steps, for i in range(1,3), for j in range(1,3) (i.e. iterating in the order (i, j) = "(1,1), (1,2), (1,3), (2,1),…, (3,3)" based on the third assumption)

                a. Throttle down FFPs (process ranks faster than FRP) with scale j, throttle up slow processes (process ranks slower than FRP) with scale i until range is small enough such that all processes are likely to occur at least once within a given number of steps.

94

      b. Apply throttling factor to rate constants, run another snapshot.

  b. If only QE process event frequencies exist

    i. If slowest non QE process transition probability is greater than 10^6 s^{-1}, throttling factor = 0.1 for all QE processes (a 10 percent throttling factor is used in this situation to reduce the risk of violating the marginal change assumption).

    ii. If slowest non QE process transition probability is less than or equal to the floor (in this case 10^6 s^{-1}), set the throttling factor = 1 for all QE processes, then run another snapshot.

  c. If only non QE process event frequencies exist

    i. If range is small enough such that all processes are likely to occur at least once within a computationally feasible number of steps, run another unthrottled snapshot

    ii. Else, identify FRP, for i in range(1,3), throttle slow processes (process ranks slower than FRP) with Scale i, until range is small enough such that all processes are likely to occur at least once within a given number of steps, run another snapshot.

4. Repeat Step 3 for M snapshots

5. At snapshot M+1, unthrottle slow rate constants and run 1 unthrottled snapshot

6. Repeat Step 2

Within this algorithm, Step 3 shows that all possible throttling combinations are explored until the compression is sufficient to allow all slow process ranks to occur at least once within a

computationally feasible number of steps (excluding negligibly slow process ranks). Step 5 is performed 1/M times as a means to relax the system, but within this step, it is reasonable to assume that mostly FFPs will occur.

8.6   Results

The SQERTSS dynamic throttling algorithm has been applied to the sample reaction network outlined in Table 8.1. The reaction network has been implemented with the intent of reaching formaldehyde production through desorption. The only input gas is methanol, meaning the first process to occur will be methanol adsorption. Subsequently, dissociation of H from the methanol molecule can occur via process number 9. Various processes with low activation barriers occur when H^+ is accumulated on the surface such as reaction number 3 and, assuming Ce^{3+} exists on the surface, reaction number 2. These low activation processes are responsible for the small time steps in an unthrottled reaction mechanism and the problem that the throttling algorithm is attempting to address. The current section will describe the effectiveness, and relative differences, between each of the throttling scales, investigated separately. Additionally, the full throttling algorithm has been applied to the reaction network and compared with the unthrottled reaction network in order to see the effects of throttling on both the transient and steady-state outcome of the KMC simulation. These comparisons will be mainly focused around formaldehyde desorption events. All simulations have been performed on a Linux virtual machine using an Intel Core 2 Duo CPU with a processing speed of 2.33 GHz and 4 GB of RAM.

In order to ensure that each of the throttling scales will result in a similar outcome, each scale has been applied to the sample reaction network separately. The formaldehyde desorption event frequency with each of the throttling scales applied separately, as well as the full algorithm, is shown in Figure 8.3a and b for the same span of time. Each of the scales is in good agreement

with each other, as well as with the dynamic throttling algorithm, giving confidence that even as compression of the time scales increases, the system is still progressing along the same trajectory.

a)

Event Frequency (s^{-1})

5000
4000
3000
2000
1000

- ■ - All Scales
- ● - N$_{Sites}^{P}$ Fast + Unthrottled Slow
- ▲ - N$_{Sites}^{P+1}$ Fast + N$_{Sites}^{P+1}$ Slow
- ▼ - N$_{Sites}$ x 10^P Fast + N$_{Sites}$ x 10^P Slow
- ◆ - N$_{Sites}$ x 1.1 Fast + N$_{Sites}$ x 1.1 Slow

0.00   0.01   0.02
Time (s)

b)

Event Frequency (s^{-1})

5000
4000
3000
2000
1000
0

0.00   0.01   0.02
Time (s)
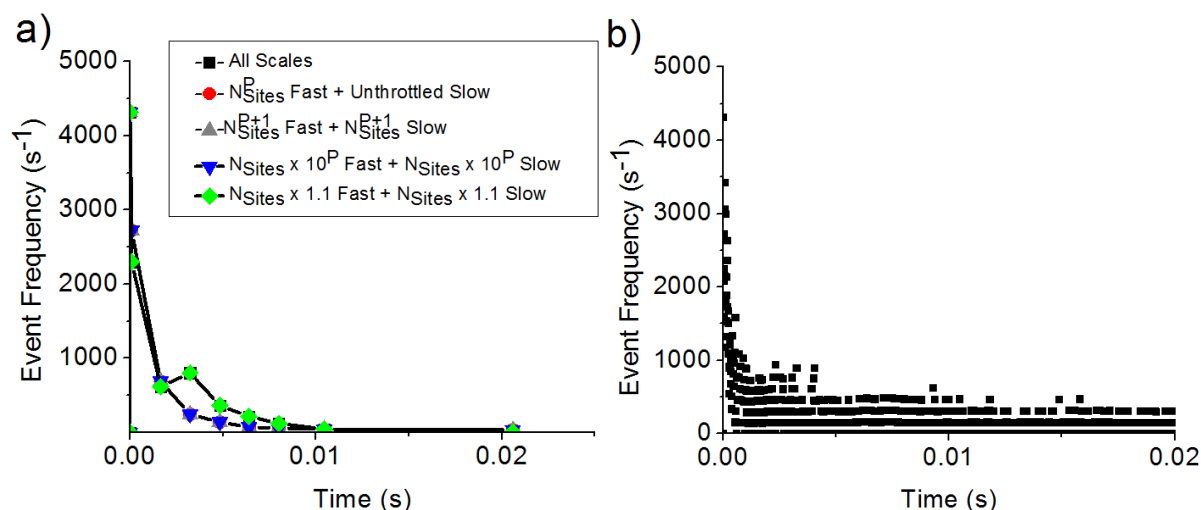
Figure 8.3 a) Comparison of all throttling scales and the full algorithm for formaldehyde production when applied to the simplified reaction mechanism. b) Unthrottled formaldehyde production from the simplified reaction mechanism. The scales have been made equal between these graphs to show the good agreement between throttled and unthrottled simulations. As shown in figure 8.4 the throttled simulations were able to run for much longer time scales. In Figure 8.3a, there is much overlap between the series plotted.

In addition, each throttling scale shown in Figure 8.3a is following the same reaction trajectory as the unthrottled reaction network shown in Figure 8.3b. In the unthrottled case, there are many points where the event frequency is zero due to the fact that the reaction mechanism is largely dominated by FFPs during this time period. To further illustrate that the throttled reaction network gives the same output of formaldehyde production, the throttled reaction network, the unthrottled reaction network and the moving average of the unthrottled formaldehyde production event frequency have been plotted together in Figure 8.3 and good agreement is found between the moving average and the throttled reaction network. The throttled reaction network was capable of reaching times significantly greater than the unthrottled reaction network. Figure 8.4 shows an order of magnitude greater in time between the throttled and unthrottled reaction network, where the throttled data has been truncated and actually reached times on the order of 10^4 seconds.
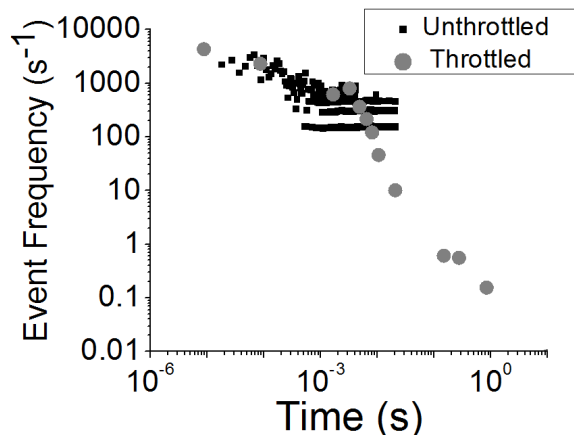
Figure 8.4 Comparison of throttled and unthrottled simulations of the formaldehyde production event frequency. The throttled simulation overlaps with the unthrottled simulation, but is able to achieve orders of magnitude higher timescales in the same computational time.

The full reaction network shown in Figures 8.3 and 8.4 reaches a steady-state formaldehyde production of 0 molecules/s due to a poisoning of the surface. Thus, a subset of these reactions has been used to produce a non-zero steady-state output of formaldehyde. This subset of reactions consists of reactions 1, 2, 3, 8, 9, 10 and 13. The throttling algorithm was applied until steady-state was reached and the steady-state surface configuration at 300 seconds (KMC time) was exported. The steady-state surface configuration was then imported to an unthrottled KMC simulation in order to see the effect of the throttling algorithm. The formaldehyde production from the throttled KMC simulation and the steady-state surface configuration are shown in Figure 8.5 a and b. When the surface configuration was input to the unthrottled simulation, the simulation was dominated by H hopping and electron transfer events. In this configuration, the throttled simulation snapshots were about 1/3 s each. In the unthrottled simulation, the snapshots were on the order of 10^{-6} s, showing the effectiveness of the throttling algorithm at decreasing the occurrence of FFPs. After 1500 snapshots (10^8 KMC steps and 0.01 s) only two snapshots resulted in formaldehyde production.
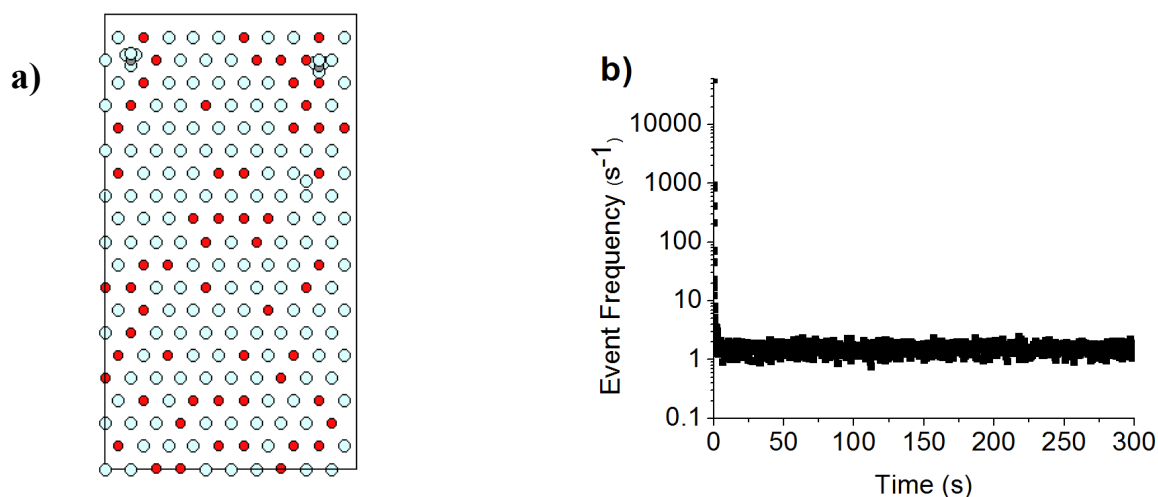
Figure 8.5 a) Steady-state surface configuration (light blue and red atoms represent H and O respectively. The two molecular species present are both methanol) and b) Formaldehyde production from throttled simplified reaction network.

8.7 Discussion

Figures 8.3 and 8.4 demonstrate the similarity between the three throttling scales providing confidence that none of the throttling scales produce significant distortion of the reaction mechanism by comparison to another. Likewise, it is shown that the transient behavior of this particular reaction network is strongly reproduced by the throttled reaction network. In this example, the transient behavior was correctly reproduced for this reaction network (i.e., even the time dependence matched that of the unthrottled simulation). The fact that such good agreement was found even for the transient time dependence of this case example can be regarded as fortuitous. In general, this algorithm is likely to reproduce the same system configuration trajectory for transient behavior, but not the same time-scale. However, if there is a unique steady-state for a given reaction network, the throttling algorithm will drive the system toward that state provided that none of the required assumptions have been violated. Thus, for systems that may not otherwise be computationally tractable, this algorithm enables simulating the configuration trajectory towards steady state as well as (perhaps more importantly) simulating the steady-state itself.

As mentioned in section 2, there are two possible ways in which the SQERTSS throttling algorithm can be applied: either where the ratios of the forward and reverse process are maintained

(paired ranking) or where the relative staggering between processes is maintained (unpaired ranking). Maintaining the relative staggering of the processes is, in general, more accurate for chemical reaction networks which operate in series. Maintaining the ratios of forward and reverse processes is, in general, more accurate for chemical reaction networks that operate in parallel. However, complex chemical reaction networks can be a mixture of parallel and series reactions so we cannot make a general statement about which of these two methods is more accurate. We can, however, state that maintaining the ratios of the forward and reverse processes results in increased compression. Thus, whichever of the two methods meets the compression criteria is chosen in the current work. An additional point regarding compression is that the current algorithm uses three different scalings all with the form N_{Sites} x C^P. In the current work, C takes a values of N_{Sites}, 10 or 1.1. The factor of C could, in principle, be implemented dynamically in order to meet the desired compression and maximum accuracy. As shown in Figure 8.3a, none of the scalings used here introduced significant inaccuracies into the simulation in Figure 8.3b and each of the throttling scales correctly simulated the same trajectory towards the final state.

Within the throttling algorithm, only slow processes are unthrottled after M snapshots. In this study, periodic unthrottling occurred after every M=10 snapshots. This allows for a partial relaxation of the surface to occur by slowing down the slow processes to their normal rates for a single snapshot. Thus, during these snapshots, gas production events would be less likely and faster reversible events such as hopping between sites would be more likely to occur. As the simulation progresses towards steady-state, the FFPs such as H hopping remain throttled. Once the simulation has reached steady-state, the throttling factors (relative to the previous M snapshots) for slow processes progress towards 1, meaning they are left unthrottled (relative to the previous M snapshots). This indicates that there exists a unique set of rate constants that represent the steady-

state behavior of the system. In other words, once the FFPs are sufficiently slow to meet the computational needs, no further throttling of rate constants is required. This set of rate constants could be throttled up or down and the steady-state output fluxes would be the same provided that none of the assumptions are violated. All of this is a consequence of the throttling algorithm allowing for the FFPs to occur, but not allowing them to dominate the calculations performed as they typically would.

A floor value for the transition probability of QE processes was implemented when only QE processes exist for multiple sequential snapshots. This was necessary to retain the marginal assumption. When only QE processes are present, the system is a metastable state which can be exited either due to accessing a rare configuration *or* accessing a long enough time-scale for a rare process. As described above, we do not have a way of predicting which exit path the simulation will take to have a non QE process occur. Slowing down the QE processes will increase the probability of a rare process occurring without distorting the configuration space that is explored. However, if the processes are throttled too far the simulation time may be significantly distorted when a rare configuration is one of the exit paths. We must make a compromise for how far we are willing to throttle the transition probabilities of the QE processes in order to encourage the likelihood of a rare process occurring (keeping in mind that it may instead be a rare configuration that exits the simulation from the state). As an approximation, we have calculated a floor value for how far the QE transition probabilities can be throttled to minimize the distortion of the times associated with the snapshots based on the characteristic timescale of the slowest QE process. The characteristic timescale is often given by the half-life of the process, and for a first order process the solution is:

$$t_{1/2} = ln(2)/k$$

If we want the time steps to be no larger than 10^{-6} s then the floor of k takes an approximate value of 10^6 s^{-1}. This implies that if the system enters a state in which only QE processes exist and remains there for many steps, that the minimum QE rate constant (transition probability) will be throttled no further than 10^6 s^{-1} and that the time steps will be on the order of 10^{-6} s. Once a non QE process enters in to the realm of possibility, the time steps will then become larger, depending on the available process rate constants (transition probabilities) and the metastable state will naturally be exited. If we can afford simulating 10^6 configurations to get out of a metastable state, then we are capable of capturing the exit from any metastable state that lasts 1 second or less. Additionally, the above choices imply that the time distortion will be insignificant provided that the RFP is significantly slower than 10^{-6} s during steady state. These two time-related limits are the ones that become affected by the choice of the floor. The effect of increasing the floor value for the rate constant was investigated for our reaction network by changing the floor from to 10^6 s^{-1} and 10^8 s^{-1}. The simulations were identical, which is an indication that the floor value of 10^6 s^{-1} did not distort the time steps.

The implemented throttling algorithm is effective at identifying QE FFPs that move in a back and forth direction (e.g. A $\leftrightarrow$ B), where QE behavior is identified by investigating the ratio of the occurrence of the forward and reverse processes. When this ratio reflects that the forward and reverse processes are close to equal, a QE is identified. A current limitation of the SQERTSS algorithm is that it is unable to identify non-QE FFPs such as loops (e.g. A $\rightarrow$ B $\rightarrow$ C $\rightarrow$ A).

The throttling algorithm was shown to be effective at slowing down QE FFPs (and speeding up slow processes) sufficiently to allow for a steady-state production of gas products H_2 and formaldehyde in the reaction system studied, where both gas production processes had steady-state event frequencies on the order of ~1-3 molecules/s. In contrast, the unthrottled simulation

resulted in primarily H hopping events and other QE FFPs *even* if a steady state configuration found by the throttled simulation was fed as a starting point into the unthrottled simulation. The time steps in the unthrottled simulation were approximately six orders of magnitude smaller. As a consequence, the unthrottled simulation would need to perform ~10^6 snapshots in order to see a countable number of gas production events (which would still not be enough to accurately capture the statistics). Likewise, within the scope of the investigation of this particular chemical reaction network, the maximum relevant simulation time is on the order of 10h. With the throttling algorithm simulation, this 10h time is computationally feasible in a matter of hours of CPU time and requires on the order of 10^4 snapshots. Without throttling, the computational time is significantly increased and would require an estimated 10^{11} snapshots to achieve which would require on the order of 10^7 hours.

8.8   Conclusions

A dynamic throttling algorithm based on identification of quasi-equilibrium fast frivolous processes, SQERTSS, has been developed and implemented for use in lattice KMC simulations. The algorithm has been applied to a chemical reaction network containing 14 reaction processes. By identifying and dynamically throttling the QE FFPs and slow processes according to the process ranks and the FRP, steady-state conditions have been achieved with a significant improvement in the computational efficiency of the KMC. For the reaction network simulated, simulation times >10^4 s are easily within the computational reach of the throttled algorithm, whereas in the unthrottled case, simulation times on the order of 1 s carry significant computational expense. The dynamic throttling algorithm was shown to produce the same transient and steady-state output as the unthrottled simulation.

8.9 Acknowledgments

References

[1] D. Mei, J. Du, M. Neurock, Ind. Eng. Chem. Res., 49 (2010) 10364-103737.

[2] M. Stamatakis, D.G. Vlachos, ACS Catalysis, 2 (2012) 2648-2663.

[3] E.W. Hansen, M. Neurock, Journal of Catalysis, 196 (2000) 241-252.

[4] A. Farkas, F. Hess, H. Over, The Journal of Physical Chemistry C, 116 (2012) 581-591.

[5] A.P.J. Jansen, J.J. Lukkien, Catalysis Today, 53 (1999) 259-271.

[6] O. Deutschmann, Modeling and Simulation of Heterogeneous Catalytic Reactions: From the

Molecular Process to the Technical System, Wiley2013.

[7] A.P.J. Jansen, An Introduction to Kinetic Monte Carlo Simulations of Surface Reactions,

Springer Berlin Heidelberg2012.

[8] B. Temel, H. Meskine, K. Reuter, M. Scheffler, H. Metiu, The Journal of Chemical Physics,

126 (2007) 204711.

[9] K. Reuter, D. Frenkel, M. Scheffler, Physical Review Letters, 93 (2004) 116105.

[10] R.M. Nieminen, A.P.J. Jansen, Applied Catalysis A: General, 160 (1997) 99-123.

[11] C. Wu, D.J. Schmidt, C. Wolverton, W.F. Schneider, Journal of Catalysis, 286 (2012) 88-

94.

[12] S.A. Trygubenko, D.J. Wales, J Chem Phys, 124 (2006) 234110.

[13] C.S. Deo, D.J. Srolovitz, Modelling Simul. Mater. Sci. Eng., 10 (2002) 581-596.

[14] C.D. VanSiclen, J Phys Condens Matter, 19 (2007) 072201.

[15] B. Puchala, M.L. Falk, K. Garikipati, J Chem Phys, 132 (2010) 134104.

[16] M.A. Novotny, Phys Rev Lett, 74 (1995) 1-5.

[17] D.R. Mason, R.E. Rudd, A.P. Sutton, Computer Physics Communications, 160 (2004) 140-157.

[18] D.G. Vlachos, Phys Rev E Stat Nonlin Soft Matter Phys, 78 (2008) 046713.

[19] A. Chatterjee, D.G. Vlachos, Journal of Computational Physics, 211 (2006) 596-615.

[20] D.T. Gillespie, Journal of Chemical Physics, 115 (2001) 1716-1733.

[21] A. Chatterjee, K. Mayawala, J.S. Edwards, D.G. Vlachos, Bioinformatics, 21 (2005) 2136-2137.

[22] A. Chatterjee, D.G. Vlachos, M.A. Katsoulakis, The journal of Chemical Physics, 122 (2005) 024112.

[23] Z. Zheng, R.M. Stephens, R.D. Braatz, R.C. Alkire, L.R. Petzold, Journal of Computational Physics, 227 (2008) 5184-5199.

[24] C.V. Rao, A.P. Arkin, The Journal of Chemical Physics, 118 (2003) 4999.

[25] V.G. Gorskii, M.Z. Zeinaloc, Theoretical Foundations of Chemical Engineering, 37 (2003) 184-190.

[26] A. Agarwal, R. Adams, G.C. Castellani, H.Z. Shouval, J Chem Phys, 137 (2012) 044105.

[27] T.R. Young, J.P. Boris, The Journal of Physical Chemistry, 81 (1977) 2424-2427.

[28] M.A. Snyder, A. Chatterjee, D.G. Vlachos, Computers & Chemical Engineering, 29 (2005) 701-712.

[29] M.J. Hoffmann, S. Matera, K. Reuter, Computer Physics Communications, 185 (2014) 2138-2150.

[30] K.A. Fichthorn, W.H. Weinberg, The Journal of Chemical Physics, 95 (1991) 1090.

[31] D.T. Gillespie, The journal of Chemical Physics, 81 (1977) 2340-2361.

[32] D.T. Gillespie, Journal of Computational Physics, 22 (1976) 403-434.

[33] A.B. Bortz, M.H. Kalos, J.L. Lebowitz, Journal of Computational Physics, 17 (1975) 10-18.

[34] A. Savara, Journal of Physical Chemistry C, Submitted (2016).

9. A Window Based Steady-State Detection Technique for Application to Kinetic Monte Carlo Simulations

9.1 Abstract

A window-based steady-state detection algorithm has been developed for application to kinetic Monte Carlo simulation data. The algorithm applies an f-test and a t-test to accurately exit any existent warm-up period and automatically determine the appropriate window size based on the data trend. A statistical extrapolation test, based on the slope, is performed to ensure that no significant change is predicted. The algorithm is applied to a variety of data sets that correspond to trends that can be produced by kinetic Monte Carlo simulation data and is shown to successfully detect, or reject, steady-state in the appropriate cases with high effectiveness and efficiency.

9.2 Authors and Affiliations

Thomas Danielson[1], Aditya Savara[2*], Celine Hin[1,3]

*Corresponding Author: savaraa@ornl.gov

[1]Department of Materials Science and Engineering, Virginia Polytechnic Institute and State University, Blacksburg, VA, USA

[2]Chemical Sciences Division, Oak Ridge National Laboratory, Oak Ridge, TN, USA

[3]Department of Mechanical Engineering, Virginia Polytechnic Institute and State University, Blacksburg, VA, USA

9.3 Introduction

Lattice Kinetic Monte Carlo (KMC) simulation is a stochastic simulation technique that is highly suitable for the simulation of complex chemical reaction networks on crystalline surfaces[1-5]. Assuming accurate parameterization of the model, the technique is capable of reproducing experimental conditions with high accuracy. This is derived from the fact that the occurrence of the simulation reaction processes is typically defined by real kinetic parameters that describe the chemical reaction. However, the computational expense of the simulation increases with the simulation size, which makes accounting for temperature or concentration gradients along the

107

macro-surface difficult. Thus, in many cases, on the order of millions of KMC simulations, each representing a different set of spatially relevant input conditions, can become necessary in order to fully reproduce the macroscopic behavior. In many cases, such as catalysis, it is the steady-state conditions that are of interest, but with a vast array of input conditions, it is difficult (and often impossible) to predict the number of simulation steps/time necessary to reach steady-state *a priori*. The range of KMC steps/time can span a large range when millions of input conditions are present. As a result, computational time may be wasted, or the simulation may terminate prematurely, if too many, or too few, simulation steps are run. In addition, a rigorous determination is necessary in order to ensure that the system is at a true steady-state and not a quasi-equilibrated state that is slowly progressing through time. Thus, accurately and efficiently simulating macro-scale conditions using KMC requires a mathematical formulation for steady-state detection (SSD).

Steady-state detection plays an important role in a variety of fields such as systems processes monitoring, data analysis, and atomistic simulation. As such, the problem has been investigated and treated with various formulations. A primitive, but direct, method to detect steady-state is to calculate the slope of the data using linear regression[6-8]. When the slope of the data is zero, the system can be assumed to be unchanging and at steady-state. This method is limited in its application to KMC due to the fact that small regions of time may be present when the data has a very small slope. However, the time scale across which regression is performed may be so small compared to the time scale of interest that even a very small slope would translate to a large departure from the current state. Alternatively, many methods use alternative statistical techniques in order to detect steady-state. One such method is the method of Rhinehart and Cao [7] which uses an F-type statistic that computes the ratio of variances of two adjacent data

windows. When the process is at steady-state, the ratio of these two variances is 1 [7, 9-11]. This method has a setback for use on KMC data in that filters are necessary in order to deal with noise in the data. Noise is inherently present in KMC data due to the stochastic operation of the simulation, but the level of noise is difficult to predict across all outputs and thus, the choice of the filters requires prior knowledge or on-the-fly calculation. A method that combines the use of the slope, standard deviation and the mean was proposed by Kelly et al. [8], but requires specification of the appropriate window size which may vary across simulations and could have the same implications mentioned previously for the slope if selected improperly. Alternative methods are wavelet based methods and are increasingly complex in their application [12].

In the current work, a variation or combination of the previously mentioned techniques is combined to develop a three step window based steady-state detection technique. The technique provides the required amount of rigor in ensuring that a true steady-state has been reached and can be performed simultaneously with the KMC simulation. Within this method, the appropriate window size is automatically determined through rolling and growing the windows and applying statistical techniques to compare the two windows. The method first uses an F-test to calculate the necessary initial window size and exit any initial simulation warm-up period. Additional adjustment of the window size is performed while moving forward in time across the data and applying a t-test to check that the means of the two windows are equal. The final test uses a t-test to calculate a predicted value to ensure that any change that occurs will be insignificant. In the following sections, a description of the KMC method used for the current work, the steady-state detection algorithm and its application to a KMC data, will be provided to exhibit the proficiency of the algorithm for its use on KMC simulations of complex chemical reaction networks.

9.4   Background

A window based steady-state detection technique has been developed in order to detect a true steady-state in a complex chemical reaction network on a crystalline surface, investigated by lattice kinetic Monte Carlo simulation. The primary output of interest for detecting steady-state in this study is the event frequency (EF) of the reaction processes (i.e. the number of times a reaction occurs per second). In the current section, a brief description of the lattice kinetic Monte Carlo technique, the associated intricacies that the steady-state detection technique is capable of handling, and the steady-state detection technique will be provided.

9.4.1   Lattice Based Kinetic Monte Carlo

Lattice based kinetic Monte Carlo simulations have been implemented within the KMOS framework [13]. The utility of the lattice based KMC technique for simulating complex chemical reaction networks stems from its ability to precisely account for local configurations within a crystalline sample. As with many other lattice based KMC techniques, the KMOS implementation transitions a system along a trajectory of configuration space by randomly selecting a reaction process with a probability that is weighted by the reaction's transition frequency, w, (the transition frequency typically has an Arrhenius-like form, but this is not required) and the availability of the necessary surface configuration for the reaction process to occur. As such, the primary inputs for the KMC simulation are the crystalline geometry, extended periodically in x-, y-, and z-directions, the reaction transition frequencies and the necessary geometric conditions and actions associated with the occurrence of a reaction process. At each KMC step, a single reaction process is selected for occurrence. Within KMOS, the variable step-size method (VSSM)[14-16] is utilized to increment the time in the following way:

$$\Delta t^s = \frac{-\ln{(r)}}{\sum_{i=1}^{M} w_i} \text{ and } t = t + \Delta t^s \tag{1}$$

where, r is a random number uniformly distributed on the interval of (0,1], w_i is the transition frequency of process i, and $\sum_{i=1}^{M} w_i$ is the sum of all (*M*) available transition frequencies in the current surface configuration. Thus, since two subsequent configurations can have a different availability of reaction processes and through the use of a uniform random number, the time steps are variable in size at each step.

For the purposes of steady-state detection, the primary output of interest in the current study is the EF (i.e. the reaction rate, where KMOS uses units of events per second per unit cell). When *all* reaction processes' EF are unchanging through time, the reaction network is at steady-state since no new reactions, nor any change in the reaction rates, is driving an evolution of the system (this is closely related to the steady-state approximation for chemical kinetics [17]). As mentioned previously, only one reaction process occurs at each KMC step. Thus, in a simulation consisting of N unit cells, the EF for a specific reaction process, a, at any KMC step is defined as:

$$EF_a^s = \frac{1}{N\Delta t^s} \; if \; the \; process \; occurs \qquad (2)$$

or,

$$EF_a^s = 0 \; if \; the \; process \; does \; not \; occur \qquad (3)$$

From this definition, at a given KMC time, if there are two or more reaction processes with similar configurational availability and similar transition frequency, their respective number of occurrences in that sequence of time steps would be close to equal. As such, the EFs of these processes would produce "spikey" data (i.e. oscillating between 0 and EF). In order to mitigate the severity of spikey data that is produced in a simulation, the KMC outputs are typically grouped into a larger series of KMC steps called a KMC snapshot. The appropriate size of the KMC snapshot is system dependent, but for the current work, it is typically on the order of 10^4 to 10^5 KMC steps. Generally speaking, the snapshot size should be sufficiently large to get a large

enough sample of events occurring through the KMC snapshot time to have relatively "smooth"

data when compared to analyzing individual steps. However, the snapshot size should not be so

large as to compromise the overall efficiency of gathering sufficient data from the simulation. The

time elapsed in a given KMC snapshot consisting of X KMC steps is:

$$\Delta t^{sp} = \sum_{i=1}^{X} \Delta t_i^s \tag{4}$$

where, Δt_i^s is the time increment for KMC step i. From Eq. 2, the EF for process a during a KMC

snapshot is defined as:

$$EF_a^{sp} = \sum_{i=1}^{X} EF_a^s \tag{5}$$

Thus, in order to meet the criteria that a true steady-state of the chemical reaction network

has been reached within the KMC simulation, we can state:

$$\frac{dEF_a^{sp}}{dt} = 0 \tag{6}$$

for all reaction processes in the simulation.

In the development of a steady-state detection technique for application to a KMC

simulation of a complex chemical reaction network, one must anticipate and accommodate for, the

possible trends of the output data that may be produced by any given simulation. In the following

section, the anticipated trends and the associated methods for accommodation are introduced along

with the algorithm.
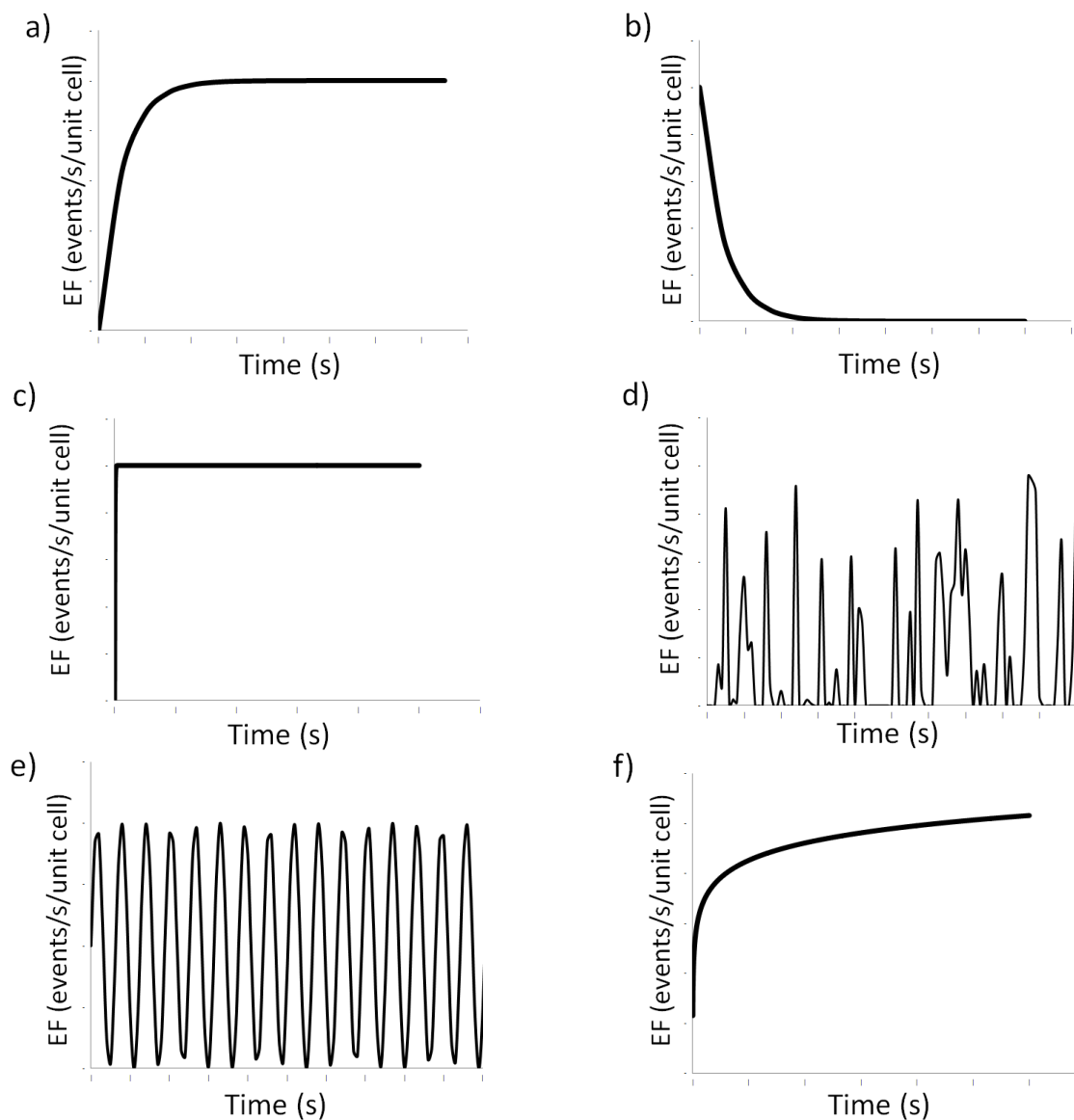
Figure 9.1 Anticipated trends in the EFs from KMC simulations a) rising exponential, b) falling exponential, c) "immediate steady-state", d) rare-events (or "spikey" data), e) oscillating steady-state and f) infinitely-rising. Each of these trends will need to be properly treated by the steady-state dection algorithm.

9.4.2   *Steady-State Detection Algorithm*

In the current study, the trends that have been anticipated are shown in Figure 9.1. With the exception of Fig. 9.1f (represented by a natural log functional form), each of the example trends for the EF in Fig. 9.1 could be present in either steady-state or transient simulation periods. Fig. 1 a, b and c all reach a trend in which the infinitesimal change in the EF is close to 0 (i.e. zero slope), but if all reaction processes are not at steady-state, the system may be driven into a state where the EF with the zero slope trend begins to increase or decrease. In addition, these three

113

examples exhibit an initial "warm-up" period that can heavily skew the EF data, adding complications to the application of statistical quantities (e.g. the standard deviation or the mean) to detect steady-state. Thus, allowing the simulation to exit this period is of key importance. Alternatively, Fig. 9.1 d and e represent data trends which may be mistaken for transient behavior if only a small chunk of the data is analyzed, when in reality, a steady-state trend is present. For these reasons, the algorithm developed in this work employs a technique in which two adjacent data windows (i.e. data series through time) of the same number of EF output data are statistically compared. To avoid the issues of: 1) detecting steady-state too soon or 2) not detecting steady-state because of a limited chunk of data being analyzed, the adjacent windows both roll (i.e. progress along the data trend eliminating earlier data points from the sample) and grow (i.e. additional data elements are added) until sufficient data is present to pass steady-state criteria. The SSD algorithm developed within this work relies on three statistical tests which must be passed in subsequent order as follows (the full algorithm is shown in Appendix A Figure A.2):

1) An f-test to check that the windows' standard deviations are equal (i.e. the null hypothesis is that $\sigma_{W1} = \sigma_{W2}$).

2) A two-sample t-test to check that the windows' means are equal (i.e. the null hypothesis is that $\mu_{W1} = \mu_{W2}$).

3) A prediction of a future EF at a future time (x^*), where the mean lies between the 95% confidence intervals of the predicted value and the predicted value is within +/- 5% of the upper or lower bound of the confidence intervals.

These tests ensure that the SSD algorithm is sufficiently strict so as to not confuse a quasi-steady-state for a true steady-state, while having the flexibility to handle data sets which are oscillating or "spikey". The latter is especially important as the example trends shown in Fig. 9.1

114

(a-f) are only representative of the types of overall trends that will be seen from a KMC simulation. In reality, typical data from KMC simulations will have some level of stochastic noise due to the stochastic selection of reaction processes (assuming that the snapshot size is significantly smaller than the number of steps it takes to reach steady-state). The full algorithm, assumptions and user defined criteria are given in Figure A.1 and A.2 in Appendix A.

9.5 Results

In the current section, the SSD algorithm will be applied to the sample data profiles (shown in Figure 9.1) that have been generated with random noise and random spacing along the x-axis that is of different random size. In doing so, the utility of the algorithm to detect steady-state in the types of data trends produced by KMC simulation will be demonstrated. Three different spacings have been considered along the x-axis, which will be referred to as "small random spacing", "large random spacing", and "uniform spacing". In addition, levels of random noise will be applied to each of the data trends which will be referred to as "0.01", "0.2", and "0.6" noise levels. To obtain the (x,y) data for each of the functions, the noise levels and the random spacings along x have been obtained in the following way:

- Two arrays of random numbers have been created: r_1 and r_2, where $0 < r_1, r_2 < 1$

- The spacing for "large random spacing" is: $10^{10^{0.1*r_1}}$ where $r_1 \in r_1$

- The spacing for "small random spacing" is: r_2 where $r_2 \in r_2$

- The spacing for "uniform spacing" is 0.01

- The noise levels (n) have been applied to each of the functions as: $f(x) + nr$, where $r \in r_1$ or r_2. If "large random spacing" has been applied, then $r \in r_2$. If "small random spacing" has been applied then, $r \in r_1$. If "uniform spacing" has been applied, $r \in r_1$.

- The y data for "spikey" data with "large random spacing" has been obtained by: If $0.25 < r_1 < 0.75$, $y = 1000nr$, where $0 < r < 1$ and $r \neq r_1, r_2$. Else, $y = 0$.

115

- The y data for "spikey" data with "small random spacing" has been obtained by: $If\ 0.25 < r_2 < 0.75,\ y = 1000nr$, $where\ 0 < r < 1\ and\ r \neq r_1, r_2.\ Else, y = 0.$

- The y data for "spikey" data with "uniform spacing" has been obtained by: $If\ 0.25 < r_1 < 0.75,\ y = 1000nr$, $where\ 0 < r < 1\ and\ r \neq r_1, r_2.\ Else, y = 0.$

A comparison of the time scales resulting from the applied methods for "large random spacing", "small random spacing" and "uniform spacing" is shown in Figure 9.2 where each data set contains 1000 data points. It is shown that "large random spacing" results in a data set which extends 3 orders of magnitude farther along x than "uniform spacing" and approximately 1 order of magnitude farther in along x than "small random spacing". The maximum step along x in this case is on the order of 10^1. For "small random spacing", the maximum step along x is 10^0 and for "uniform spacing", the maximum step along x is 10^{-2}. From these different spacings along the x axis, the effects of non-uniform spacing on the ability of the algorithm to detect steady-state have been investigated. The noise levels that have been applied to the functional forms are shown in Figure 9.3. The natural log has been omitted from these images and will be discussed in its own subsection.
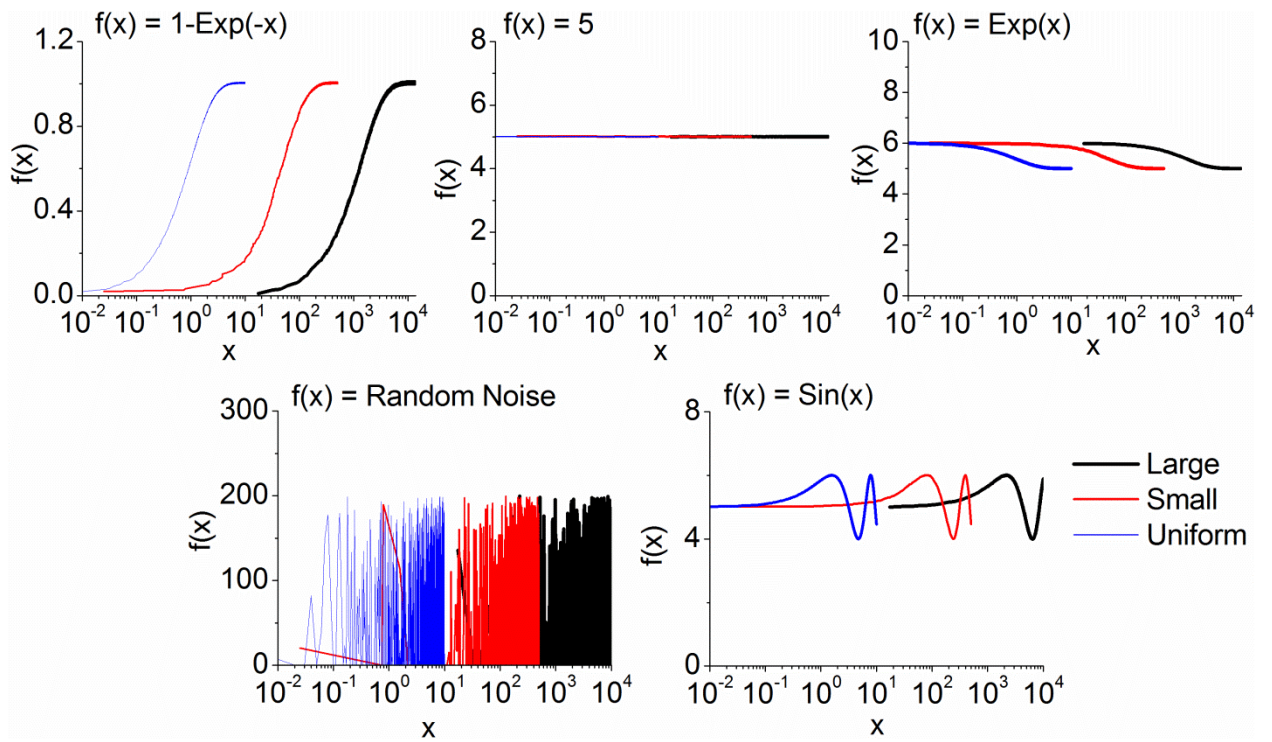
Figure 9.2 Comparison of the distribution along the *x*-axis of 1000 data points generated by functional forms that have been used to test the SSD algorithm.
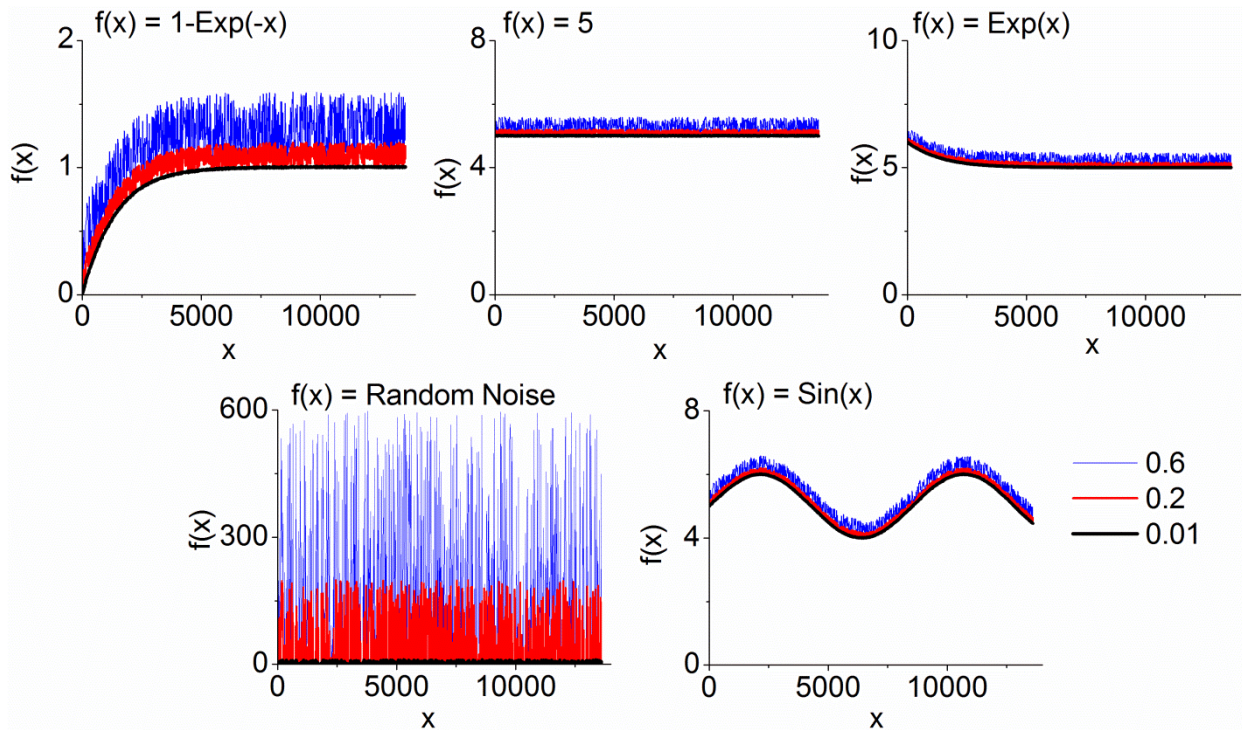
Figure 9.3 Comparison of the noise levels applied to the functional forms.

In the following subsections, the SSD algorithm has been applied to each of the functional

forms. The base testing for the following subsections requires the slope test (i.e. the final test to

117

trigger steady-state) to be passed two consecutive times, though additional testing of this parameter will be performed and reported. In addition, the algorithm is applied to a KMC simulation for a chemical reaction occurring on a surface which leads to CH_2O production from an initial input of CH_3OH. The details of the chemical reaction network are not of high importance for the current work, but the intention is to show that the steady-state detection algorithm can be applied to real KMC data and successfully determine when the system has reached steady-state. In all cases, the predicted value of y is calculated at ten times the maximum x-value of window 2.

9.5.1   Infinitely Increasing f(x) = Ln(x)

$Ln(x)$ approaches infinity as x goes to infinity, though the approach to infinity becomes increasingly gradual as x increases. As such, this is not a true steady-state and thus, a steady-state detection algorithm should be capable of eliminating such a trend as a steady-state. The currently implemented algorithm does not detect steady-state in data generated with a natural log function containing any level of noise, or spacing, with even the loosest criteria of passing the slope test only two consecutive times. In fact, the t-test very rarely passes, so the slope test rarely has the opportunity to be tested. This strongly suggests that the window sizing methods used here are capable of gathering a large enough sample to avoid a false detection. If a natural log type of trend presented itself within KMC data, the current approach would be to allow the simulation to run until the relevant simulation time has been reached. If the simulation reaches that time before steady-state, the simulation would be automatically ended, and the conclusion is that the initial conditions were not capable of producing a steady-state in the time scale of interest.

9.5.2   Rising Exponential f(x) = 1-exp(-x)

The rising exponential trend has been tested and steady-state has been successfully detected in the asymptotic region of the functional trend. This particular functional trend provides a strong test of the capability of the SSD algorithm to successfully exit a warm-up period that may exist

within KMC data. The point at which steady-state has been detected is shown in Figure 9.4 and it is clearly seen that the data windows have surpassed the warm-up period and reached the asymptotic region.

Figure 9.4 Steady-state detection algorithm as applied to data generated by a rising exponential functional form, "large random spacing" and 0.6 noise level. The data windows are shown in red and the point at which steady state is reached is indicated.

The functional form has been tested for each noise level and spacing along the *x*-axis. The number of data points in the data windows, the number of steps to steady-state, the means of the windows, the standard deviations of the windows and the predicted *y*-values are shown in Table 9.1. The spacing seems to have a minimal effect on the number of steps to detect steady-state and in all cases, the lowest level of noise reaches steady-state nearly immediate after exiting the warm-up period as expected.

Table 9.1 The number of data points considered in each window, the number of steps to steady-state, the mean of window 1 and window 2, the standard deviation of window 1 and window 2, and the predicted y values as calculated by the SSD algorithm for each noise level and spacing along the *x*-axis.

	N_{elem}	N_{step}	μ_1	μ_2	σ_1	σ_2	$\hat{y}$
Large Spacing							
0.01	132	1867	1.0052	1.0051	0.0029	0.0028	0.9981
0.2	600	3894	1.1021	1.0991	0.0578	0.0579	1.0731
0.6	600	3894	1.3064	1.2972	0.1733	0.1736	1.2192
Small Spacing							
0.01	102	1502	1.0055	1.0051	0.0027	0.0027	1.0015
0.2	611	3949	1.1022	1.1072	0.5886	0.0057	1.1848
0.6	611	3949	1.3067	1.3217	0.1766	0.1710	1.5545
Uniform Spacing							
0.01	100	1394	1.0050	1.0055	0.0031	0.0028	1.0128
0.2	652	5376	1.0997	1.1009	0.0584	0.0570	1.1095
0.6	652	5376	1.2992	1.3029	0.1751	0.1710	1.3286

9.5.3   Straight Line f(x) = 5

The functional form for a straight line with noise is strongly representative of a KMC data trend that would correspond to an immediate steady-state. The SSD algorithm tested here successfully detects that the trend it at steady-state with a reasonable efficiency. The detection of steady-state and the associated data windows are shown in Figure 9.5.
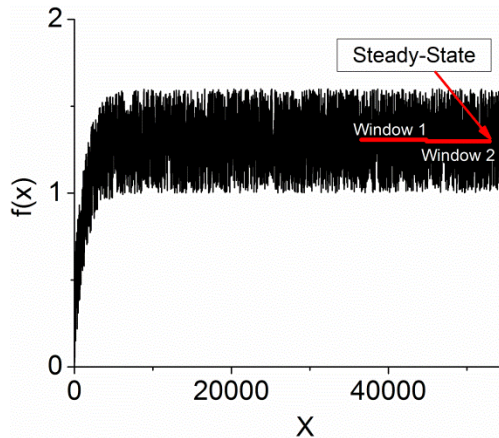
Figure 9.5 Steady-state detection algorithm as applied to data generated by a straight line functional form, "large random spacing" and 0.6 noise level. The data windows are shown in red and the point at which steady state is reached is indicated.

As shown in Table 9.2, the spacing does not largely impact the detection of steady-state in this case. However, for each spacing, the 0.6 noise level takes the longest to detect steady-state, while both 0.01 and 0.6 detected steady-state in the same number of steps.

Table 9.2 The number of data points considered in each window, the number of steps to steady-state, the mean of window 1 and window 2, the standard deviation of window 1 and window 2, and the predicted y values as calculated by the SSD algorithm for each noise level and spacing along the *x*-axis.

	N_{elem}	N_{step}	μ_1	μ_2	σ_1	σ_2	$\hat{y}$
Large Spacing							
0.01	100	395	5.0049	5.0052	0.0027	0.0028	5.0085
0.2	100	395	5.0984	5.1044	0.0548	0.0561	5.1701
0.6	604	3513	5.2899	5.3002	0.1674	0.1731	5.4801
Small Spacing							
0.01	104	415	5.0048	5.0050	0.0028	0.0027	5.0122
0.2	104	415	5.0965	5.1006	0.0564	0.0564	5.2437
0.6	610	2945	5.3008	5.3060	0.1722	0.1722	5.3311
Uniform Spacing							
0.01	104	415	5.0048	5.0052	0.0028	0.0029	5.0121
0.2	104	415	5.0964	5.1038	0.0566	0.0575	5.2416
0.6	601	3498	5.3079	5.3116	0.1718	0.1753	5.5130

9.5.4 *Falling Exponential f(x) = exp(-x)*

The falling exponential functional form is another case where there exists a distinctive warm-up period at the initial stages of the data and thus, it is an important test case for the effectiveness of the SSD algorithm's applicability to KMC generated data. Similar to the rising exponential, the algorithm once again successfully exits the warm up period and detects steady-state well into the asymptotic region of the generated data in all cases. The data windows and the point at which steady-state was detected are shown in Figure 9.6.

Figure 9.6 Steady-state detection algorithm as applied to data generated by a falling exponential functional form, "large random spacing" and 0.6 noise level. The data windows are shown in red and the point at which steady state is reached is indicated.

The trends for the number of steps to reach steady-state are largely similar to the straight line case for the falling exponential trend. In this case, the spacing has little effect on the number of steps that it takes to reach steady-state, but the noise levels do not, as shown in Table 9.3.

Table 9.3 The number of data points considered in each window, the number of steps to steady-state, the mean of window 1 and window 2, the standard deviation of window 1 and window 2, and the predicted y values as calculated by the SSD algorithm for each noise level and spacing along the *x*-axis.

	N_{elem}	N_{step}	μ_1	μ_2	σ_1	σ_2	$\hat{y}$
Large Spacing							
0.01	132	1867	5.0052	5.0051	0.0029	0.0028	4.9981
0.2	132	1867	5.1041	5.1014	0.0582	0.0562	4.9626
0.6	600	3894	5.3063	5.2972	0.1732	0.1736	5.2192
Small Spacing							
0.01	102	1502	5.0055	5.0051	0.0027	0.0027	5.0013
0.2	102	1502	5.1103	5.1028	0.0547	0.0540	5.0280
0.6	611	3949	5.3067	5.3217	0.1765	0.1710	5.5544
Uniform Spacing							
0.01	100	1394	5.0051	5.0055	0.0031	0.0028	5.0125
0.2	100	1394	5.1008	5.1103	0.0627	0.0561	5.2541
0.6	652	5376	5.2992	5.3029	0.1751	0.1710	5.3286

9.5.5   *Oscillating f(x) = Sin(x)*

The functional form for oscillating data has been tested and is another possible trend that could result from KMC generated data. As long as the overarching trend does not have an slope and the data is oscillating around a mean value, the data would be considered to be at steady-state and thus, a sinusoidal curve is representative of this data. The data windows and the point at which steady-state was detected are shown in Figure 9.7. It is shown that steady-state is detected when the window sizes are large enough such that they encompass roughly one full period of the sinusoidal curve. It would be expected that one full period would be the minimum window of data necessary to determine that an oscillating trend was in fact oscillating around a constant mean and did not have a slope. Thus, this demonstrates that the SSD algorithm is capable of efficiently (in terms of data quantity) detecting steady-state in an oscillating trend.
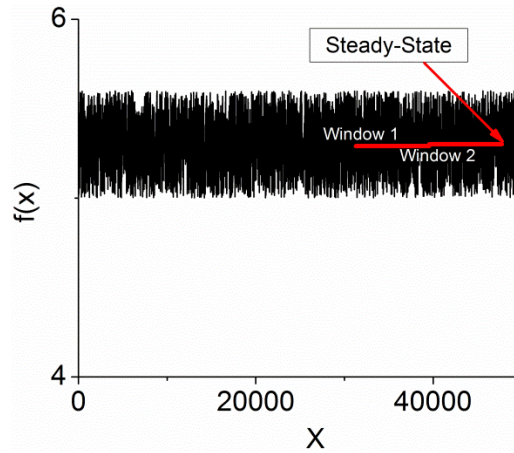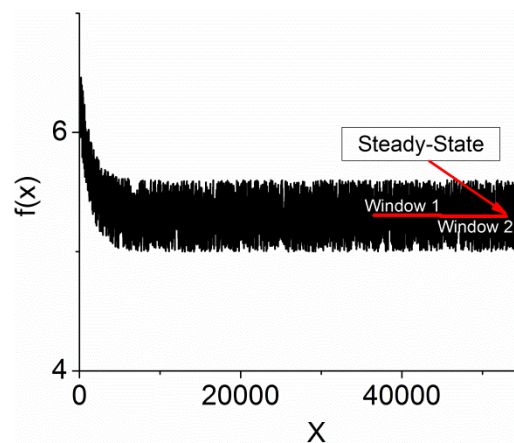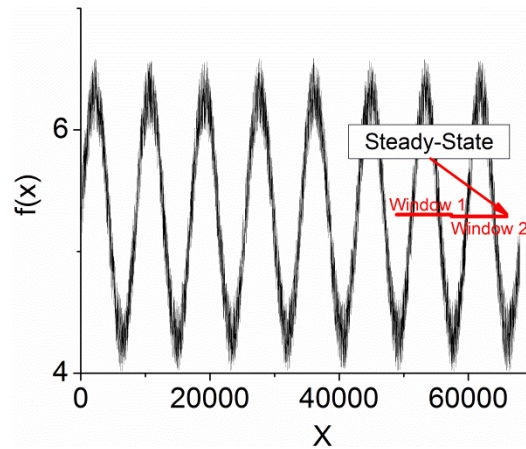
Figure 9.7 Steady-state detection algorithm as applied to data generated by an oscillating functional form, "large random spacing" and 0.6 noise level. The data windows are shown in red and the point at which steady state is reached is indicated.

In this case, the noise levels and the spacing have very little influence on the ability to detect the steady-state. This is likely because the oscillating trend of the data overshadows the noise within the functional data. The number of steps to reach steady-state in the case of large random spacing with 0.2 noise added was the highest, yet the window size is similar. This indicates that the algorithm was passing the slope test once, but not the second time, thus the window was repeatedly shifted by N (the window length), rather than 1 when the t-test for the means is failed. In a sinusoidal case, it is easy to see that if a data window is largely comprised of points that are near the maxima or minima of the curve, the slope would be close to zero. Once the test passes one time, the windows are shifted by the window length for a subsequent test. At this point the data windows lie along the ascending or descending portions of the trend and the slope is non-zero. This behavior demonstrates the importance of the requirement to have the slope test pass at least twice. As shown in Figure 9.7, a window size of roughly 630 for large spacing corresponds to roughly one full period of the sinusoidal curve. Within one full period of a sinusoidal curve, the trend is repeated twice. Thus, one full period is the absolute minimum amount of data that would be necessary to say that the trend is oscillating around a common mean.

Table 9.4 The number of data points considered in each window, the number of steps to steady-state, the mean of window 1 and window 2, the standard deviation of window 1 and window 2, and the predicted y values as calculated by the SSD algorithm for each noise level and spacing along the *x*-axis.

	N_{elem}	N_{step}	μ_1	μ_2	σ_1	σ_2	$\hat{y}$
Large Spacing							
0.01	629	4854	5.0016	5.0014	0.7088	0.7090	6.1525
0.2	630	6113	5.0935	5.0957	0.7123	0.7117	6.1561
0.6	628	4851	5.3047	5.2887	0.7219	0.7334	6.3843
Small Spacing							
0.01	629	4853	5.0277	5.0275	0.7135	0.7136	6.1409
0.2	628	4223	5.1288	5.1246	0.7161	0.7144	6.2993
0.6	629	4228	5.3429	5.3301	0.7382	0.7361	6.0976
Uniform Spacing							
0.01	629	4854	5.0056	5.0055	0.7068	0.7070	6.1421
0.2	630	5485	5.1001	5.1005	0.7116	0.7069	6.2287
0.6	628	4224	5.3195	5.3086	0.7291	0.7254	6.3067

9.5.6   *Random Noise*

Random noise or "spikey" data is strongly representative of rare or slow events in kinetic Monte Carlo simulations. In certain circumstances, these rare events can cause a system to progress out of a quasi-steady-state, and thus it is important to ensure that all processes have reached steady-state. However, these types of trends can also exist at steady-state where some event occurs very sporadically and thus, it is important for a SSD scheme to be capable of detecting steady-state. The data windows and point at which steady-state detection occurs are shown in Figure 9.8.
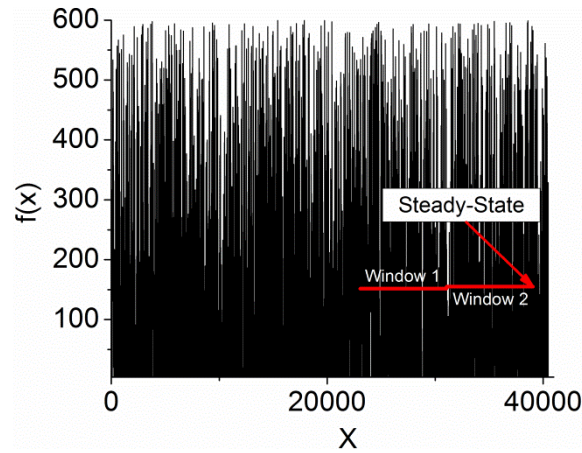
Figure 9.8 Steady-state detection algorithm as applied to random noise or "spikey" data, "large random spacing" and 0.6 noise level. The data windows are shown in red and the point at which steady state is reached is indicated.

It is shown in Table 9.5 that in all cases, steady-state is detected in nearly the same number of steps, where the spacing and the noise levels have very minimal effect on the detection. In this case, it is found that the predicted y value is occasionally calculated to be a negative number, but all of the data is 0 or a positive number. This occurs because the data is randomly generated where approximately 50% of the data is positive and approximately 50% of the data is 0. However, for a given window size, the distribution of positive numbers and zeros may vary. Thus, the upper and lower bounds of the confidence intervals may span both positive and negative numbers and still contain the mean and be within 5% of the predicted value.

Table 9.5 The number of data points considered in each window, the number of steps to steady-state, the mean of window 1 and window 2, the standard deviation of window 1 and window 2, and the predicted y values as calculated by the SSD algorithm for each noise level and spacing along the *x*-axis.

	N_{elem}	N_{step}	μ_1	μ_2	σ_1	σ_2	$\hat{y}$
Large Spacing							
0.01	599	2890	2.5140	2.5876	3.2693	3.2532	2.8483
0.2	599	2890	48.7792	50.7292	63.9440	63.7298	85.8682
0.6	599	2890	151.7010	155.0360	197.5719	196.5081	64.4417
Small Spacing							
0.01	609	2320	2.5594	2.4429	3.1501	3.1501	-1.1397
0.2	609	3536	51.5500	50.7452	64.2642	64.2308	3.0593
0.6	609	3536	157.6207	157.5808	197.2204	200.1334	187.2849
Uniform Spacing							
0.01	601	3498	2.5344	2.4791	3.1726	3.2065	4.0931
0.2	601	3498	50.9992	47.6782	64.5185	63.1805	-13.1075
0.6	601	3498	148.4512	150.0074	191.7938	190.9313	312.9837

9.5.7   *Number of consecutive attempts to pass the slope test*

As shown for the case of the oscillating data trend, the slope test can introduce significant differences in the number of steps required to detect steady-state. However, the importance of performing this test more than once was emphasized by the oscillating data to ensure that the detection of steady-state at a given point in a data trend is not fortuitous. The more times this test is required to pass, the more certain one can be that the data trend is in fact at a true steady-state. However, increasing the number of consecutive attempt also increases the number of data points required. As such, a compromise between certainty and computational efficiency exists. The effects of passing the slope test an increased number of times are shown in Table 9.6. It is shown that the number of steps to reach steady-state increases in all cases, which is expected. By the differences in the number of steps to reach steady-state, it is clear that more failures of the test occur with increasing number of consecutive attempts to pass the slope test. However, the window sizes stay very close to the same for each successive increase in the number of attempts.

Table 9.6 Comparison of the number of steps and the window sizes for 2, 3, and 4 attempts to pass the slope test for each set of generated data. Each test represents data generated with 0.6 noise and large random spacing.

	2		3		4	
	N_{elem}	N_{step}	N_{elem}	N_{step}	N_{elem}	N_{step}
1-Exp(-x)	600	3894	604	5712	667	8733
5	604	3513	604	4115	606	6537
Exp(-x)	600	3894	604	5712	604	6314
Sin(x)	628	4851	631	8630	631	9259
Random Noise	599	2890	606	5322	606	5926

9.5.8   *Application to KMC data*

The SSD algorithm has been applied to a kinetic Monte Carlo simulation of a simplified chemical reaction network. Within this simulation, there is an input of CH_3OH gas and through a series of reaction processes, an output flux of CH_2O gas is produced. The input flux of the CH_3OH gas is held constant, but in addition to the CH_2O gas, there is also an output flux of CH_3OH gas. Thus, the SSD algorithm must monitor both output fluxes to determine when the system has reached steady-state. The algorithm has been applied to both sets of data and is shown in Figure 9.11. In this case, the algorithm detects steady-state very early (430 KMC snapshots of size 10^5) in the reaction for the CH_3OH output flux as shown in Fig 9.11 a which is very similar in nature to the generated data set for the immediate steady-state. This occurs because the simulation starts with an initially uncovered pristine surface. Thus, when the input flux is introduced, it is quickly filled and the output flux of the original gas quickly reaches equilibrium. However, steady-state is not triggered at this point because the CH_2O output flux is still evolving. Steady-state is triggered for the KMC simulation after 2910 KMC snapshots when both output fluxes are unchanging.
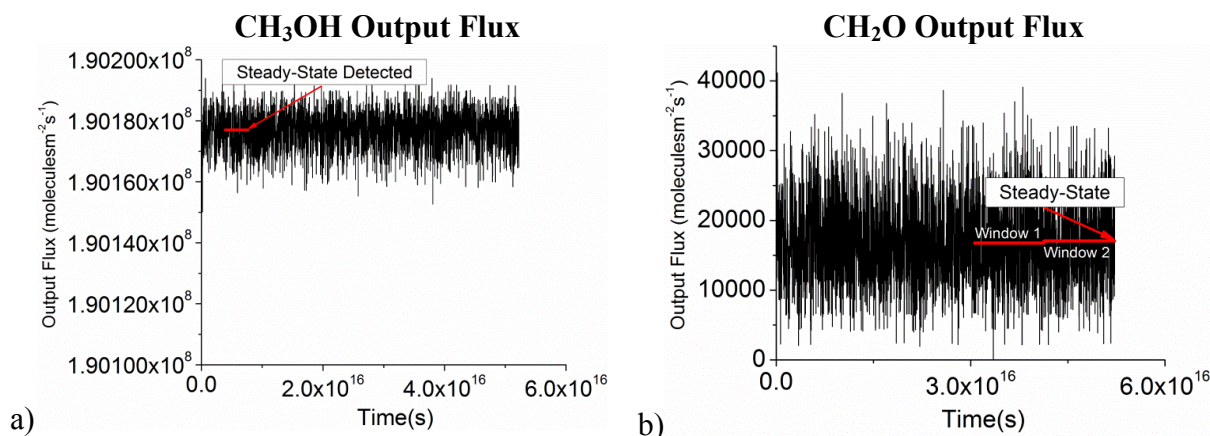
Figure 9.9 Steady-state detection algorithm as applied to KMC simulation data for a chemical reaction that produces CH3OH and CH2O output fluxes. Steady-state is detected earlier in the CH3OH output flux, but steady-state is not actually triggered until the CH2O output flux has reached steady-state.

9.6   Discussion

The steady-state detection algorithm effectively and accurately detects steady-state in each case of functionally generated data and each set of data is strongly representative of possible KMC trends with differing levels of noise. In all cases, it is strongly indicated that the spacing along the x-axis does not play a significant role in the number of steps, or the required window size, to reach steady-state detection. This is not surprising as the spacing along the x-axis is accounted for in the linear regression that is performed in the procedure for calculating the predicted value of the slope.

In all cases shown in section 9.5, the residuals calculated for use in linear regression for the slope extrapolation test were not weighted. However, additional tests were performed using regression that applied a weighting factor to the residuals. Since the VSSM is used in our KMC simulations, the y data points do not represent equal increments of time. Thus, the weighting of the residuals was performed based on the particular interval of time that a given y-value represents. No significant differences were found between the SSD algorithm that used non-weighted residuals and the algorithm that used weighted residuals except for the case of the oscillating data. The oscillating data with 0.6 noise, large random spacing and 2 consecutive slope tests required to

be passed, the number of steps to steady-state detection was 57352. The corresponding window size was 9420, which is an order of magnitude larger than any of the cases that used non-weighted residuals. This was the largest number of steps found, and though we have tested a fairly all-encompassing range of functional forms, this may not be the ceiling for the number of steps a given trend may require when using weighted residuals. The same test case for the non-weighted residuals was shown to detect steady-state with a window size that spanned one period (i.e. the minimum required to detect steady-state for an oscillating trend). In many cases, a given y-value represents a snapshot of KMC data that can span on the order of 10^4 to 10^6 KMC steps. Thus, in the event that oscillating data arose in a KMC simulation, the steady-state detection algorithm would require on the order of 10^9 to 10^{11} KMC steps if weighted residuals are used. From this, the non-weighted residuals are taken to be the more efficient algorithm in terms of the algorithmic computational expense, data required and ease of implementation. In addition, no significant increase in accuracy is introduced by the weighted residuals and the tests cases shown with non-weighted residuals do not raise any concerns with their accuracy of detection.

In nearly all of the test cases, the highest level of noise takes the largest number of steps to reach steady-state detection. This is likely due to the fact that the higher the level of noise, the more likely it is that the slope test fails. This demonstrates the importance of selecting an appropriate snapshot size so as to reduce the effects of the stochastic noise of the KMC simulation as much as possible.

9.7   Conclusions

A window based steady-state detection algorithm was developed and tested on a variety of potential data trends that could be produced by kinetic Monte Carlo simulations. The successive testing of the equality of the standard deviations and the means of the windows was shown to be effective at surpassing any warm-up type periods that exist in data trends. In addition, the slope

test within the algorithm effectively detected steady-state for each of the test cases and successfully declined steady-state in the case of the gradually, but infinitely, increasing non-steady-state trend. The SSD algorithm was applied to KMC data for a simulation generating output fluxes of CH_3OH and CH_2O gas and steady-state was detected for both sets of output fluxes. The utility of the implemented algorithm extends beyond KMC and can be used for a variety of simulation techniques, process monitoring or data analysis.

9.8 Acknowledgements

References

[1]   A. Farkas, F. Hess, and H. Over, The Journal of Physical Chemistry C **116** (2012).

[2]   E. W. Hansen, and M. Neurock, Journal of Catalysis **196** (2000).

[3]   S. Matera, H. Meskine, and K. Reuter, J Chem Phys **134** (2011).

[4]   D. Mei, J. Du, and M. Neurock, Ind. Eng. Chem. Res. **49** (2010).

[5]   M. Stamatakis, and D. G. Vlachos, ACS Catalysis **2** (2012).

[6]   R. M. Bethea, and R. R. Rhinehart, *Applied Engineering Statistics* (Taylor & Francis, 1991).

[7]   S. Cao, and R. R. Rhinehart, J. Proc. Cont. **5** (1995).

[8]   J. D. Kelly, and J. D. Hedengren, Journal of Process Control **23** (2013).

[9]   E. Crow, F. Davis, and M. W. Maxfield, *Statistics Manual* (U.S. Naval Ordnance Test Station, 1955).

[10]   R. R. Rhinehart, in *American Control Conference (ACC), 2013*2013), pp. 4477.

[11]   M. Mansour, and J. E. Ellis, Applied Mathematical Modelling **32** (2008).

[12]   A. Mhamdi *et al.*, *On-line optimization of MSF desalination plants* (LPT, RWTH, 1999).

[13]   M. J. Hoffmann, S. Matera, and K. Reuter, Computer Physics Communications **185** (2014).

[14]   K. A. Fichthorn, and W. H. Weinberg, The Journal of Chemical Physics **95** (1991).

[15]   D. Gillespie, Journal of Computational Physics **22** (1976).

[16]   D. Gillespie, The Journal of Physical Chemistry **81** (1977).

[17]   S. J. Fraser, The Journal of Chemical Physics **88** (1988).

10. Generalized Adsorption Isotherms for Molecular and Dissociative Adsorption of a Polar Molecular Species on Two Polar Surface Geometries: Perovskite (100) (Pm-3m) and Fluorite (111) (Fm-3m)

The following manuscript has been submitted to the Journal of Chemical Physics and is currently under review.

10.1 Abstract

Lattice based kinetic Monte Carlo simulations have been used to determine a functional form for the second order adsorption isotherms on two commonly investigated crystal surfaces: the (111) fluorite surface and the (100) perovskite surface which has the same geometric symmetry as the NaCl (100) surface. The functional form is generalized to be applicable to all values of the equilibrium constant by a shift along the pressure axis. Functions have been determined for estimating the pressure at which a desired coverage would be achieved and for estimating the coverage at a certain pressure. The generalized form has been calculated by investigating the surface adsorbate coverage across a range of thermodynamic equilibrium constants that span the range 10^{-26} to 10^{13}.

10.2 Authors and Affiliations

Thomas Danielson[1], Celine Hin[1,2], Aditya Savara[3*]

*Corresponding Author: savaraa@ornl.gov

[1]Department of Materials Science and Engineering, Virginia Polytechnic Institute and State University, Blacksburg, VA, USA

[2]Department of Mechanical Engineering, Virginia Polytechnic Institute and State University, Blacksburg, VA, USA

[3]Chemical Sciences Division, Oak Ridge National Laboratory, Oak Ridge, TN, USA

10.3 Introduction

Adsorption isotherms are functions which relate the coverage, θ, to the pressure, P, or other measure of the adsorbate's activity at a given pressure. Prior to the 20th century, adsorption isotherms were only obtainable via empirical data. The first analytical approximations for

adsorption isotherms were developed by Langmuir in the early 20th century, but the underlying assumptions such as an adsorbate species that behaves like an ideal gas, no lateral interactions of adsorbates and a simple first order adsorption process, are valid for only the most elementary and controlled reactions [1]. Langmuir's approximations have been extended, in an analytical way, to include lateral interactions and higher order adsorption reaction processes [2-13], but currently, there are many adsorption processes and surface geometries which do not have an analytical solution, such as molecular adsorption of a polar molecule on a polar substrate. Thus, obtaining an adsorption isotherm for a particular gas adsorbing or reacting on a surface with a particular geometry would require experimentation or accurate simulation/modeling [14-21].

Lattice kinetic Monte Carlo (KMC) simulations are a tool for simulating chemical reactions on surfaces that can take into account the local configuration [22-26]. The probability of a particular reaction occurring in a given time period is based on the reaction rate, which is fixed by its rate constant and thus, the stochastic simulation technique is capable of mimicking the statistical occurrence of real-world reaction processes in a way that is exact, assuming that the model is accurately parameterized. As a result, performing lattice KMC simulations with adsorption and desorption processes allows an effective empirical method for determining adsorption isotherms with increased accuracy when compared to analytical approximations.

In the current work, lattice KMC simulations have been used to determine a functional form for the adsorption isotherm across the entire parameter space on two different surface geometries of widespread interest; the (111) fluorite surface and the (100) perovskite surface. The isotherms for the (100) perovskite surface also apply to (100) surfaces for the NaCl structure, as these have the same geometric symmetry. For each surface, the general functional forms derived are capable of being used to determine the coverage as a function of pressure, or vice-a-versa, for

134

any value of the equilibrium constant, and thus at any pressure. The same packing (and thus isotherms) should apply for cases of liquid to surface adsorption, as well.

10.4   Theoretical Background and Computational Setup

10.4.1   Theoretical Background for Analytical Solutions and KMC of Adsorption Isotherms

To understand the relationship between all adsorption isotherms for a given surface geometry, we first consider the analytical solution for an adsorption isotherm based on the Langmuir adsorption model (this is unrelated to how the kinetic Monte Carlo simulations are performed). First we define an adsorption process of a polar molecular species, *M*, on a polar substrate (i.e. a surface with two unequal sites, *A* and *B*, where the adsorption process results in a bridging occupation of both *A* and an adjacent *B*):

$$\mathbf{M}\ (g)\ +\ A\ +\ B_{adjacent}\ \rightarrow\ A-\mathbf{M}_{bridging}\ (ads)-B$$
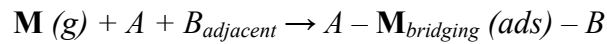
or for a dissociative adsorption process:

$$\mathbf{M}\ (g)\ +\ A\ +\ B_{adjacent}\ \rightarrow\ \mathbf{M}^{+}-A\ +\ \mathbf{M}^{-}-B$$
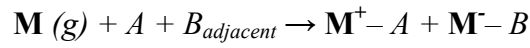
In these types of adsorption processes, multiple molecular orientations are possible between *A* and *B* sites (during adsorption, an *A* site is filled along with only one of the *N* neighboring *B*). In the mean field approximation where local configurations are ignored, the rates of adsorption and desorption are proportional to the concentrations of the sites and surface species involved, allowing us to write:

$$r_{ads} = k_{ads}\ P[A][B] \tag{1}$$

$$r_{des} = k_{des}\ \theta \tag{2}$$

where, *P* is the pressure, θ is the relative surface coverage, [A] is the fraction of open A sites, and [B] is the fraction of open B sites. The concentrations of the open sites and the surface coverage ([A], [B], θ) are each bound by [0,1]. k_{ads} and k_{des} are the rate constants for adsorption and desorption and are defined as:

$$k_{ads} = \frac{S}{\sqrt{2\pi k_B Tm}} e^{\frac{-E_A}{RT}} A_u \tag{3}$$

$$k_{des} = Ae^{\frac{-E_A}{RT}} \tag{4}$$

where, S is the steric factor, k_B is the Boltzmann constant, T is the temperature, m is the molecular mass of the gas phase molecule, E_a is the activation energy, A_u is the area corresponding to an A site along with one adjacent B site, R is the gas constant and A is the pre-exponential factor (typically with units of s⁻¹).

When considering the impacts of local configurations, analytical solutions to the isotherm for this situation can be derived for the low coverage cases. In this case, the adsorption rate requires having an open B site next to an open A site, and we can write:

$$r_{ads} = k_{ads} P[A] [B]_{adjacent} \tag{5}$$

Where *[B]adjacent* reflects the probability of an open B site adjacent to an open A site. The desorption rate is unchanged.

At very low coverages (e.g. $\theta \le 0.01$), we can say that to a very good approximation any unoccupied A is neighboring an unoccupied B. Thus, the rate of adsorption can be simplified based on the approximation that all B sites are unoccupied (i.e. *[B]adjacent = 1*) which gives:

$$r_{ads} = k_{ads} P[A] [B]_{adjacent} = k_{ads} P[A] = k_{ads} P (1 - \theta) \tag{6}$$

At equilibrium, the forward and reverse rates are equal, so we can set the forward and reverse rates equal followed by rearranging to obtain an expression for the isotherm. Using eq. 6 for the rate of adsorption and eq 2 for the rate of desorption, setting $r_{ads} = r_{des}$, we find that the very low coverage isotherm can be approximated by:

$$\theta_i = \frac{KP}{1 + KP} \text{ where } K_i = \frac{k_{ads}}{k_{des}} \tag{7}$$

where, K is the equilibrium rate constant of adsorption and desorption for a specific isotherm (i.e., specific temperature and surface).

For medium coverages (e.g. $0.1 \leq \theta \leq 0.3$), the approximation that all B sites are uncovered no longer holds. Instead, the odds of finding an unoccupied B site adjacent to an unoccupied A site is approximately the same as the odds of finding an unoccupied A site to begin with (i.e. *[B]adjacent* ≈ *[A]*). Using this approximation, the rates of adsorption and desorption are defined as:

$$r_{ads} = k_{ads}\, P[A]\, [B]_{adjacent} = k_{ads}\, P[A][A] = k_{ads}\, P\, (1 - \theta)^2 \tag{8}$$

$$r_{des} = k_{des}\ \theta \tag{9}$$

and again, setting r_{ads} = r_{des}, the equilibrium coverage for a given isotherm is:

$$\theta_i = \frac{2KP - \sqrt{4KP + 1} + 1}{2KP} \tag{10}$$

At high coverages (e.g. $\theta \geq 0.3$), we can no longer analytically determine the surface concentration of B sites because it is uncertain how increasing the occupation of A sites affects the concentration of B sites adjacent to unoccupied A sites. Thus, a numerical method, such as KMC, is necessary in order to determine the equilibrium coverage for the high coverage regimes.

Lattice kinetic Monte Carlo simulations within the KMOS framework [27] have been used to determine a functional form for all coverage regimes of the adsorption isotherm of a polar adsorption process. Within the lattice KMC framework, the surface stochastically evolves along a trajectory of configuration space that is probabilistically defined by the transition frequencies, w, for the processes considered. The link between KMC and the analytical solutions for the equilibrium coverage of a specific adsorption isotherm is made by the fact that the probability of the system transitioning (i.e. transition frequency, w) from configuration u to a subsequent configuration v via reaction process q is defined by the same kinetic parameters (activation energy

137

and pre-exponential) as the chemical kinetics reaction rate constant for that reaction. However, the probability of a reaction occurring within KMC is also defined by the surface configuration (as opposed to surface concentration in the analytical formulations). That is, if the surface configuration is such that process q can occur, the reaction process's transition frequency is w. If the configuration is such that process q can occur, the reaction process's transition frequency is 0 until a configuration arises where the process can occur. Thus, on a particular site, s, the rate at which a particular reaction, q, transitions the system to a new configuration is proportional to the number of times that the local configuration exists where process q is available to occur. That is:

$$r_q^s = w_q C_o \tag{11}$$

where, C_o is 0 or 1, depending on whether or not the configuration exists. From this, the net rate of reaction q is:

$$r_q^{net} = \sum_1^N w_q C_o \tag{12}$$

where, N is the total number of a particular site type on which reaction process q can occur.

If we define configuration u to be the surface with N adsorbates and configuration v to be the surface with $N-1$ adsorbates, the reaction process, q, is desorption and w is defined by:

$$w_{des}^{u \to v} = A e^{\frac{-E_A}{RT}} \tag{13}$$

Alternatively, if the initial configuration, u, is the surface with N adsorbates and configuration v is the surface with $N+1$ adsorbates, the reaction process q is adsorption and w is defined by:

$$w_{ads}^{u \to v} = \frac{P * A_c * S}{\sqrt{2\pi k_B T m}} e^{\frac{-E_A}{RT}} \tag{14}$$

where, S is the steric factor, P is the pressure and A_c is the area corresponding to the KMC cell for which the transition is being defined (which can be larger than a single site). In our simulations,

A_C corresponds to a single KMC unit cell, which can be larger than one crystallographic primitive unit cell.

From this, the evolution of the surface concentration in a KMC simulation containing adsorption and desorption processes is given by:

$$\frac{d\theta}{dt} = r_{ads}^{net} - r_{des}^{net} \tag{15}$$

The equilibrium surface coverages depend upon the balance of the rates of adsorption and desorption, which in turn depend upon the adsorption and desorption transition frequencies (i.e. $W_{Eq} = \frac{w_{ads}}{w_{des}}$). To find a functional form that extends across the entire realistic parameter space for the ratio of w_{ads} to w_{des}, realistic upper and lower bounds of adsorption equilibrium constants were determined and KMC simulations covering equilibrium constants spanning the entire realistic parameter space have been investigated. Realistic ranges for the kinetic parameters are shown in Table 1, and were used to determine realistic bounds for the equilibrium constant. Based on the boundaries in Table 1, the lower and upper bounds for realistic thermodynamic equilibrium constants for gas-solid adsorption are 10^{-26} and 10^{13} respectively, with 1 bar as the reference pressure P°. The molecular mass of methanol (32 atomic mass units) was used in the adsorption rate constant: all phase molecules under standard conditions have masses within 1 order of magnitude of methanol, so the bounds here are realistic for all gas phase molecules under standard conditions.

Table 10.1 Upper and lower bounds for all relevant parameters in k_{ads} and k_{des}

	Lower Bound	*Upper Bound*
P	10^{-8} bar	10 bar
S	10^{-6}	1
T	5 K	1000 K
E$_a$	10 kJ	200 kJ
A	10^9 s^{-1}	10^{18} s^{-1}

The adsorption isotherms for a polar molecule have been investigated on two distinct, multi-species surfaces: the fluorite (111) surface (e.g. CeO_2) and the perovskite (100) surface (e.g. CaTiO3), shown in Figure 10.1. Below, we consider the sites corresponding to A and B in Equations 16 and 17. to be a cation and an anion, though the work is general enough to apply to other surfaces. Within this context, the adsorption process has been investigated for the situations of non-dissociative adsorption and dissociative adsorption:

1) Non-dissociative Adsorption (a.k.a. Molecular Adsorption) occurs where there is a bridging of a polar molecule between the two distinct surface species (e.g. molecular adsorption of CH_3OH bridging between a cation and an anion with the CH_3O end occupying the cation site and the H end occupying the anion site), but no dissociation of the molecule occurs

2) Dissociative adsorption occurs where immediately upon adsorption, the molecule dissociates (e.g. dissociative adsorption of CH_3OH that results in CH_3O^- occupying the cation site and the H^+ occupying the anion site).

The conditions that must be satisfied for the adsorption processes to occur are: an unoccupied cation site and at least one unoccupied first nearest neighbor anion site. As can be seen in Figure 10.1, this gives a maximum of three molecular orientations for each cation site on the fluorite(111) surface and four molecular orientations on the perovskite (100) surface. If more than one of the neighboring anion sites are unoccupied, the orientation of the adsorbate is randomly selected with an equal probability defined by the adsorption transition frequency. Within the KMC simulation of this study, the simulation size contains on the order of 400 unit cells and periodic boundary conditions are applied in the x and y directions. The surface unit cell for each structure investigated is indicated by the black box in Figure 10.1. There are two distinct anion sites and two distinct cation sites in each structure. Each orientation on each surface site has its own

transition frequency, w, though in reality, the kinetics of each is defined by the same energetics. As a result of this, the net transition frequency for adsorption processes on each cation site is:

$$w_{Ads}^{net,Fluorite} = w_{ads}^{A-B1} + w_{a\ s}^{A-B2} + w_{ads}^{A-B3} \quad (16)$$

$$w_{Ads}^{net,Perovskite} = w_{ads}^{A-B1} + w_{ads}^{A-B2} + w_{ads}^{A-B3} + w_{ads}^{A-B4} \quad (17)$$

where, w_{ads}^{A-B1} would indicate the transition frequency for an adsorption process to occur where the molecule is bridging (or dissociating) between the cation site, A, and the neighboring anion site, $B1$, as shown for each surface configuration in Figure 10.1. In a more generalized form, the net transition frequency of adsorption on a cation site that has multiple possible orientations between surrounding anion sites is given as:

$$w_{Ads}^{net} = \sum_{i=1}^{M} w_{ads}^{i} \quad (18)$$

where, M is the number of possible orientations on all sites within the kinetic Monte Carlo simulation cell (A_c), and w_{ads}^{i} is the adsorption rate constant for a specific A-B orientation, i. The rate constants from Eq. 2 and 3 is different from the transition frequencies in KMC, since the former depends on concentrations and the latter depends on configurations. To understand the relationship between the chemical kinetics rate constant for adsorption and the KMC transition frequency for adsorption, we need to look at the *net rate* of adsorption. To compare the net rate of adsorption from KMC is compared to the net rate of adsorption from the analytical solution for a given surface area, we must convert the relative rate from Eq. 6 to an absolute rate (i.e. $\frac{molecules}{m^2 s}$)

by dividing Eq. 6 by area A_u and then multiplying by the area considered in the KMC simulation, A_c. In doing so, comparing the absolute rates of adsorption from Eqs. 6 and 18 (for an area of A_c):

$$\frac{k_{ads} P[A]}{A_u} A_c \; versus \; \sum_{1}^{M} w_q^i C_o \qquad (19)$$

For our simulations, $A_c = 2A_u$, because our KMC unit cells encompassed 2 cations and 2 anions. We can find a relationship between k_{ads} and w_{ads} with the use of a symmetry factor, X, that corresponds to the presence of equivalent configurations in the KMC that are not separated explicitly in the mean-field equations. For the case when $[A] = C_o$:

$$X(2k_{ads} P) = \sum_{1}^{M} w_q^i \qquad (20)$$

where, and X is the factor that accounts for the number of possible adsorption orientations in the area A_u. In this case, the number of orientations comes from the symmetry, and we find that $X= 3$ for the fluorite (111) structure and $X=4$ for the perovskite (100) structure. In our simulations, the fluorite structure has 6 orientations in within a KMC unit cell ($A_c = 2.534x10^{-19} \; m^2$), and the perovskite structure has 8 orientations within a KMC unit cell ($A_c = 1.46x10^{-19} \; m^2$).
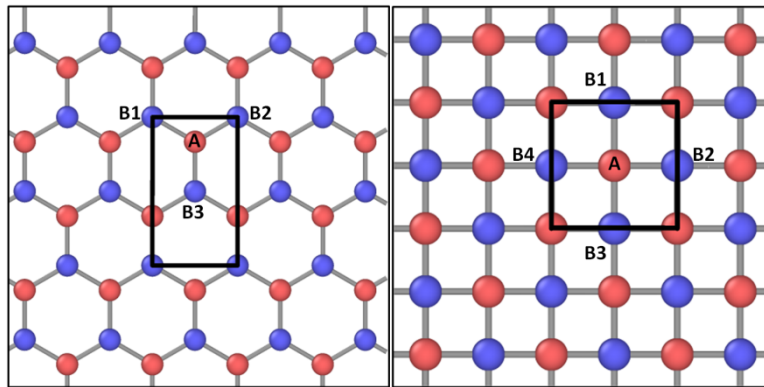

Figure 10.1(Left) Flourite (111) Structure and (Right) perovskite (100) structure. The black box indicates a single surface KMC unit cell. A and B labels indicate surface cation and anion sites respectively.

The surface coverage for the upper and lower bounds of the equilibrium transition frequency ratio was calculated across a range of pressures that would correspond to coverages in the range of [0,1] based on the Langmuir adsorption isotherm approximation. The calculated functional form is general for each surface geometry and each adsorption type and thus, the atomic surface species are less important than the geometry of the surface which defines the way in which the adsorption process occurs.

10.4.2 *Generalization of the adsorption isotherms*

The isotherms for low and medium coverages (Eqs. 7 and 10) can be extended to any value of the equilibrium constant based on a shift along the pressure axis, since K appears as a coefficient of P. That is, to determine the coverage of a different isotherm, $\theta_2(P)$, where K_1 is related to K_2 by a constant, c, we have:

$$cK_1 = K_2 \tag{21}$$

$$\theta_2 = \frac{cK_1P}{1 + cK_1P} \tag{22}$$

Which can be rewritten as:

$$\theta_2 = \frac{10^{Log(cK_1)}10^{Log(P)}}{1 + 10^{Log(cK_1)}10^{Log(P)}} = \frac{10^{Log(c)+Log(K_1)+Log(P)}}{1 + 10^{Log(c)+Log(K_1)+Log(P)}} \tag{23}$$

This shows that when changing the equilibrium constant from K_1 to K_2, the isotherm has the same functional form, with the new coverage θ_2, shifted along the pressure axis by a factor of c. The same can be shown for the medium coverage case from eq. 10. It is clear that the most important factor for determining any given isotherm is the equilibrium constant and also that a generalized functional form exists for all isotherms with respect to a given surface geometry, provided that K appears as a coefficient of P in the form of the isotherm that is solved for coverage. If the kMC derived isotherms also have this attribute (that K can be treated as a coefficient of P when the

isotherm is solved for coverage) then the KMC derived isotherms will also be generalizable for arbitrary values of K.

10.5   Results

In the current section, a functional form (for the cases of pressure or coverage being the dependent variable) will be presented for the (111) fluorite and (100) perovskite surface geometries. The generalizability of the functional forms to any adsorption isotherm for the given surface geometry will be shown through the shift along the pressure axis. In all equations of this manuscript, "Log" implies the logarithm with base 10.

10.5.1   Perovskite (100) surface geometry

10.5.1.1   Molecular Adsorption

To obtain an isotherm functional form for molecular adsorption on the (100) perovskite surface geometry, 100 different pressures in the range 0.0014 to 1606525 bar were applied to an adsorption isotherm with K = 0.018001. This corresponds to 100 KMC simulations to calculate the steady-state surface coverage. The functional dependence of the coverage on the log of pressure for the adsorption isotherm is described by piecewise fitting applied to two regions (fit to KMC data shown in Figure 10.2):

$$For\ Log\left(\frac{P}{P^\circ}\right) \epsilon\ [-2.8551, 1.4035], \tag{24}$$

$$\theta = 0.118366\ + 0.225402\left(Log\left(\frac{P}{P^\circ}\right) - Log\left(\frac{KP^\circ}{0.072004}\right)\right)$$
$$+ 0.140317\left(Log\left(\frac{P}{P^\circ}\right) - Log\left(\frac{KP^\circ}{0.072004}\right)\right)^2$$
$$+ 0.00648402(Log(\frac{P}{P^\circ}) - Log(\frac{KP^\circ}{0.072004}))^3$$
$$- 0.0198329(Log(\frac{P}{P^\circ}) - Log(\frac{KP^\circ}{0.072004}))^4$$
$$- 0.0045132(Log(\frac{P}{P^\circ}) - Log(\frac{KP^\circ}{0.072004}))^5$$

$$For\ Log\left(\frac{P}{P^\circ}\right) \epsilon\ [1.4035, 6.205887], \tag{25}$$

$$\theta = -0.270651 + 0.981059\left(Log\left(\frac{P}{P^\circ}\right) - Log\left(\frac{KP^\circ}{0.072004}\right)\right)$$

$$- 0.30278\left(Log\left(\frac{P}{P^\circ}\right) - Log\left(\frac{KP^\circ}{0.072004}\right)\right)^2$$

$$+ 0.0457836(Log(\frac{P}{P^\circ}) - Log(\frac{KP^\circ}{0.072004}))^3$$

$$- 0.00330246(Log(\frac{P}{P^\circ}) - Log(\frac{KP^\circ}{0.072004}))^4$$

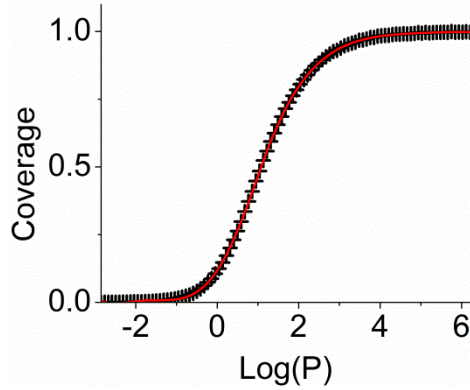$$+ 0.0000865719(Log(\frac{P}{P^\circ}) - Log(\frac{KP^\circ}{0.072004}))^5$$

Figure 10.2 Functional (red line) dependence of coverage on pressure from kMC simulations (black symbols) of molecular adsorption on the perovskite (100) surface, fitted with a piecewise function.

The inverse function, which is the functional dependence of the log of pressure on the coverage is described using piecewise fitting applied to four regions as follows functions (fit to kMC data in Figure 10.3):

For $\theta \in [0.00025, 0.124625]$, (26)
$$Log\left(\frac{P}{P^\circ}\right) = \left(0.944439 + 0.463005 * Ln(\theta)\right) - Log(\frac{KP^\circ}{0.072004})$$

For $\theta \in [0.12645, 0.87175]$, (27)
$$Log\left(\frac{P}{P^\circ}\right) = (-0.612019 + 6.00428\theta - 8.36136\theta^2 + 6.21532\theta^3)$$
$$- Log(\frac{KP^\circ}{0.072004})$$

For $\theta \in [0.87175, 0.0.991]$, (28)
$$Log\left(\frac{P}{P^\circ}\right) = (-580.433 + 2001.12\theta - 2294.26\theta^2 + 878.394\theta^3)$$
$$- Log(\frac{KP^\circ}{0.072004})$$

For $\theta \in [0.991, 0.99725]$, (29)

$$Log\left(\frac{P}{P^\circ}\right) = (-114767 + 353107\theta - 362150\theta^2 + 123816\theta^3)$$
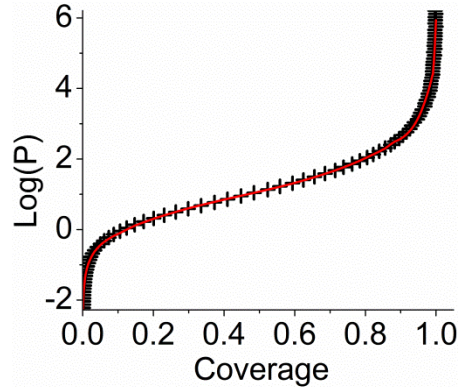$$- Log(\frac{KP^\circ}{0.072004})$$

Figure 10.3 Functional dependence (red line) of pressure on coverage from kMC simulations (black symbols) of molecular adsorption on the perovskite (100) surface, fitted with a piecewise function.

In order to illustrate the generalizability of the adsorption isotherm across an entire parameter space of equilibrium rate constants, multiple adsorption isotherms have been simulated and the shift along the pressure axis has been investigated. Figure 10.4 shows that the adsorption isotherms are shifted along the pressure axis by a factor of $c = Log(\frac{W_2}{W_1})$. The central line is the generalized fit to the original isotherm and the curves on the left and right are the lower and upper bound with the shifted fit functional form. The markers indicate the actual output of the adsorption isotherm from the KMC simulation.
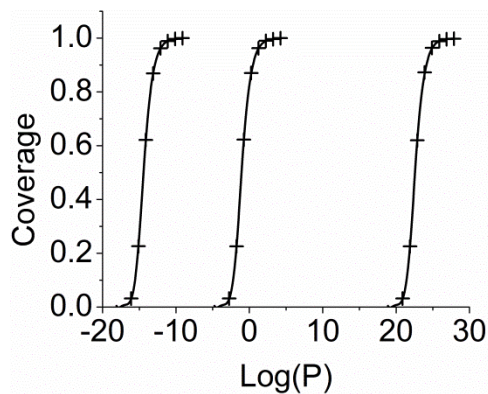

Figure 10.4 Illustration of the generalization of the functional form for any isotherm between the upper and lower bounds. The central curve corresponds to the location along the pressure axis of the original fit and the markers are the KMC data. The curves to the left and right of the central curve are the extremes close to the

146

upper bound (K_{eq} P° = 1.656x10^{12}) and lower bound (K_{eq} P° = 1.656x10^{-25}) of the equilbrium parameter space. The data is plotted with the piece-wise function from Eqs 24 and 25. As can be seen, this single piecewise function matches all of the kMC simulations.

10.5.1.2   Dissociative Adsorption

Dissociative adsorption was investigated across the same range of pressures for the same value of K. The functional dependence of coverage on the log of pressure is described by piecewise fitting applied to two regions as follows (fit to kMC data shown in Figure 10.5):

$$For\ Log(\frac{P}{P°}) \in [-2.8551833, 1.13169], \tag{30}$$

$$\theta = 0.161556 + 0.158883\left(Log(\frac{P}{P°}) - Log(\frac{KP°}{0.072004})\right)$$
$$+ 0.0604624\left(Log(\frac{P}{P°}) - Log(\frac{KP°}{0.072004})\right)^2$$
$$+ 0.00448308\left(Log(\frac{P}{P°}) - Log(\frac{KP°}{0.072004})\right)^3$$
$$- 0.0033256\left(Log(\frac{P}{P°}) - Log(\frac{KP°}{0.072004})\right)^4$$
$$- 0.0007052(Log(\frac{P}{P°}) - Log(\frac{KP°}{0.072004}))^5$$

$$For\ Log(\frac{P}{P°}) \in [1.13169, 6.205887], \tag{31}$$

$$\theta = 0.173997 + 0.0544927\left(Log(\frac{P}{P°}) - Log(\frac{KP°}{0.072004})\right)$$
$$+ 0.224246\left(Log(\frac{P}{P°}) - Log(\frac{KP°}{0.072004})\right)^2$$
$$- 0.0866211\left(Log(\frac{P}{P°}) - Log(\frac{KP°}{0.072004})\right)^3$$
$$+ 0.0123429\left(Log(\frac{P}{P°}) - Log(\frac{KP°}{0.072004})\right)^4$$
$$- 0.0006257(Log(\frac{P}{P°}) - Log(\frac{KP°}{0.072004}))^5$$

Figure 10.5 Functional dependence (red line) of coverage on pressure from kMC simulations (black symbols) of dissociative adsorption on the perovskite (100) surface, fitted with a piecewise function.

The functional dependence of the log of pressure on the coverage can be described using

piecewise fitting applied to three regions as follows (fit to kMC data shown in Figure 10.6):

$For\ \theta \in [0.009625, 0.0944375],$ (32)

$$Log(\frac{P}{P^\circ}) = (1.74793 + 0.950838 * Ln(\theta)) - Log(\frac{KP^\circ}{0.072004})$$

$For\ \theta \in [0.0944375, 0.891],$ (33)

$$Log(\frac{P}{P^\circ}) = (-1.40205 + 10.6793\theta - 15.2563\theta^2 + 10.31870\theta^3)$$
$$- Log(\frac{KP^\circ}{0.072004})$$

$For\ \theta \in [0.891, 0.995375],$ (34)

$$Log(\frac{P}{P^\circ}) = (-274.236 + 974.356\theta - 1147.74\theta^2 + 452.9910\theta^3)$$
$$- Log(\frac{KP^\circ}{0.072004})$$

$For\ \theta \in [0.891, 0.995375],$ (35)

$$Log(\frac{P}{P^\circ}) = (-13170.2 + 44305.60\theta - 49280.5\theta^2 + 181520\theta^3)$$
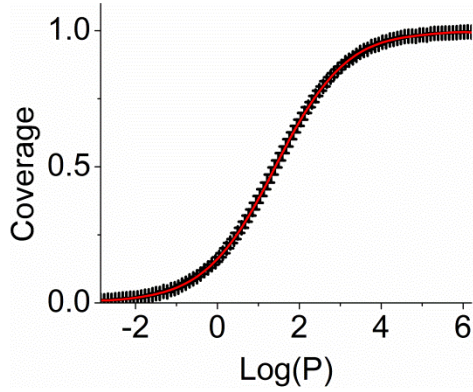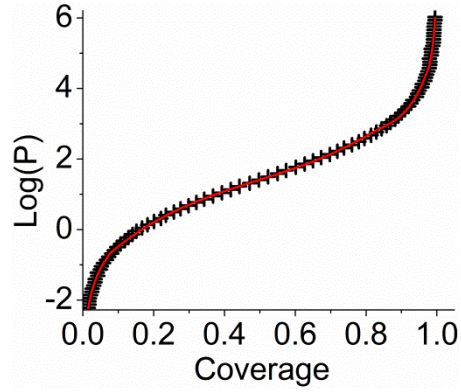$$- Log(\frac{KP^\circ}{0.072004})$$

Figure 10.6 Functional dependence (red line) of pressure on coverage from kMC simulations (black symbols) of dissociative adsorption on the perovskite (100) surface, fitted with a piecewise function.

In the dissociative case, the horizontal shift again reproduces the adsorption isotherms across the entire parameter space K in a similar fashion to the molecular adsorption case.

10.5.2 Fluorite (111) surface geometry
10.5.2.1 Molecular Adsorption

To obtain a functional form for molecular adsorption on the (111) fluorite surface geometry, 100 KMC simulation were run with pressures in the range 1.1×10^{-9} to 1.262 (bar) with K= 916313.5. The functional dependence of coverage on the log of pressure for this isotherm is described by piecewise fitting applied to two regions as follows (fit to kMC data shown in Figure 7):

$$For\ Log(\frac{P}{P^\circ}) \in [-8.9599, -5.60727],$$

$$\theta = -187.408 - 130.695(Log\left(\frac{P}{P^\circ}\right) - Log(\frac{KP^\circ}{916313.5}))$$
$$- 35.6458(Log(\frac{P}{P^\circ}) - Log(\frac{KP^\circ}{916313.5}))^2$$
$$- 4.78022(Log(\frac{P}{P^\circ}) - Log(\frac{KP^\circ}{916313.5}))^3$$
$$- 0.316384(Log(\frac{P}{P^\circ}) - Log(\frac{KP^\circ}{916313.5}))^4$$
$$- 0.0082893(Log(\frac{P}{P^\circ}) - Log(\frac{KP^\circ}{916313.5}))^5$$

(36)

149

$$For\ Log(\frac{P}{P^\circ}) \in [-5.6073, 0.101203], \theta \tag{37}$$

$$= 0.999419 - 0.0004015(Log(\frac{P}{P^\circ}) - Log(\frac{KP^\circ}{916313.5}))$$
$$- 0.0029524(Log(\frac{P}{P^\circ}) - Log(\frac{KP^\circ}{916313.5}))^2$$
$$- 0.0008746(Log(\frac{P}{P^\circ}) - Log(\frac{KP^\circ}{916313.5}))^3$$
$$+ 9.7722x10^{-5}(Log(\frac{P}{P^\circ}) - Log(\frac{KP^\circ}{916313.5}))^4$$
$$+ 9.6801x10^{-5}(Log(\frac{P}{P^\circ}) - Log(\frac{KP^\circ}{916313.5}))^5$$

Figure 10.7 Functional dependence (red line) of coverage on pressure from kMC simulations (black symbols) of molecular adsorption on the fluorite (111) surface, fitted with a piecewise function.

The functional dependence of the log of pressure on the coverage for a particular isotherm is described using piecewise fitting applied to four regions as follows (fit to kMC data shown in Figure 10.8):

$$For\ \theta \in [0.002125, 0.05725], \tag{38}$$
$$Log(\frac{P}{P^\circ}) = (-5.88671 + 0.495858 * Ln(\theta)) - Log(\frac{KP^\circ}{916313.5})$$

$$For\ \theta \in [0.05725, 0.7985], \tag{39}$$
$$Log(\frac{P}{P^\circ}) = (-7.60375 + 6.08201\theta - 8.69927\theta^2 + 6.5102\theta^3)$$
$$- Log(\frac{KP^\circ}{916313.5})$$

$$For\ \theta \in [0.7985, 0.97225], \tag{40}$$
$$Log(\frac{P}{P^\circ}) = (-112.983 + 386.32\theta - 465.93\theta^2 + 189.752\theta^3)$$
$$- Log(\frac{KP^\circ}{916313.5})$$

$$For\ \theta \in [0.97225, 0.992], \tag{41}$$

$$Log(\frac{P}{P^o}) = (7564.51 - 22141.6\theta + 21499.9\theta^2 - 6924.54\theta^3)$$
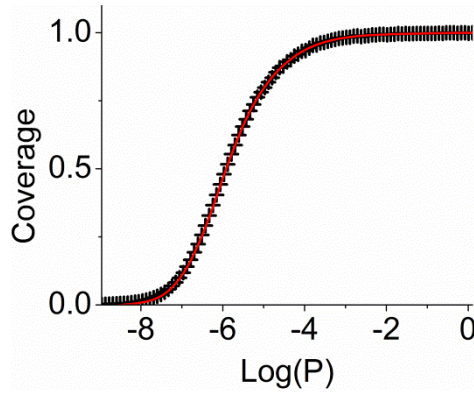$$- Log(\frac{KP^o}{916313.5})$$

Figure 10.8 Functional dependence (red line) of pressure on coverage from kMC simulations (black symbols) of molecular adsorption on the fluorite (111) surface, fitted with a piecewise function.

Once again, the functional form is shifted along the pressure axis and shows that a different surface geometry does not affect the ability of the function to represent the entire parameter space in a general form.
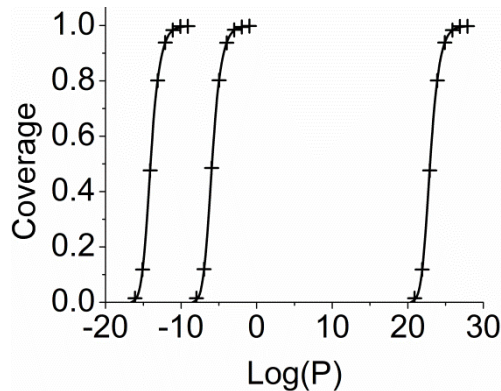
Figure 10.9 Illustration of the generalization of the functional form for any isotherm between the upper and lower bounds. The central curve corresponds to the location along the pressure axis of the original fit and the markers are the KMC data. The curves to the left and right of the central curve are the etremes close to the upper bound ($K_{eq} P^o = 1.248 \times 10^{14}$) and lower bound ($K_{eq} P^o = 1.248 \times 10^{-23}$) of the equilbrium parameter space. The data is plotted with the piece-wise function from Eqs 36 and 27. As can be seen, this single piecewise function matches all of the kMC simulations.

10.5.2.2 Dissociative Adsorption

The generalized functional form of the adsorption isotherm for dissociative adsorption on the Fluorite (111) surface geometry has been investigated for the same adsorption isotherm as the

molecular adsorption case. The functional dependence of coverage on the log of pressure for

isotherm is described by piecewise fitting applied to two regions as follows (fit to kMC data shown

in Figure 10.10):

$$\textbf{\textit{For Log}}(\frac{\boldsymbol{P}}{\boldsymbol{P^{\circ}}}) \,\epsilon\, [-8.9599, -5.15422],\tag{42}$$

$$\boldsymbol{\theta} = -19.5558 - 14.6236(\boldsymbol{Log}(\frac{\boldsymbol{P}}{\boldsymbol{P^{\circ}}}) - \boldsymbol{Log}(\frac{\boldsymbol{KP^{\circ}}}{916313.5}))$$
$$- 3.98238(\boldsymbol{Log}(\frac{\boldsymbol{P}}{\boldsymbol{P^{\circ}}}) - \boldsymbol{Log}(\frac{\boldsymbol{KP^{\circ}}}{916313.5}))^{2}$$
$$- 0.514522(\boldsymbol{Log}(\frac{\boldsymbol{P}}{\boldsymbol{P^{\circ}}}) - \boldsymbol{Log}(\frac{\boldsymbol{KP^{\circ}}}{916313.5}))^{3}$$
$$- 0.032126(\boldsymbol{Log}(\frac{\boldsymbol{P}}{\boldsymbol{P^{\circ}}}) - \boldsymbol{Log}(\frac{\boldsymbol{KP^{\circ}}}{916313.5}))^{4}$$
$$- 0.000782926(\boldsymbol{Log}(\frac{\boldsymbol{P}}{\boldsymbol{P^{\circ}}}) - \boldsymbol{Log}(\frac{\boldsymbol{KP^{\circ}}}{916313.5}))^{5}$$

$$\textbf{\textit{For Log}}(\frac{\boldsymbol{P}}{\boldsymbol{P^{\circ}}}) \,\epsilon\, [-5.15422, 0.101203],\tag{43}$$

$$\boldsymbol{\theta} = 0.9996123 - 0.0043383(\boldsymbol{Log}(\frac{\boldsymbol{P}}{\boldsymbol{P^{\circ}}}) - \boldsymbol{Log}(\frac{\boldsymbol{KP^{\circ}}}{916313.5}))$$
$$- 0.008662(\boldsymbol{Log}(\frac{\boldsymbol{P}}{\boldsymbol{P^{\circ}}}) - \boldsymbol{Log}(\frac{\boldsymbol{KP^{\circ}}}{916313.5}))^{2}$$
$$- 0.0042707(\boldsymbol{Log}(\frac{\boldsymbol{P}}{\boldsymbol{P^{\circ}}}) - \boldsymbol{Log}(\frac{\boldsymbol{KP^{\circ}}}{916313.5}))^{3}$$
$$- 0.0011727(\boldsymbol{Log}(\frac{\boldsymbol{P}}{\boldsymbol{P^{\circ}}}) - \boldsymbol{Log}(\frac{\boldsymbol{KP^{\circ}}}{916313.5}))^{4}$$
$$- 2.80549x10^{-5}(\boldsymbol{Log}(\frac{\boldsymbol{P}}{\boldsymbol{P^{\circ}}}) - \boldsymbol{Log}(\frac{\boldsymbol{KP^{\circ}}}{916313.5}))^{5}$$
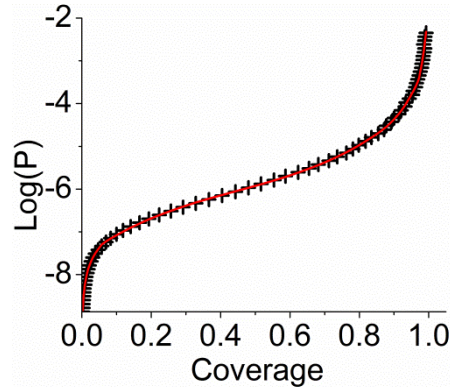

Figure 10.10 Functional dependence (red line) of pressure on coverage from kMC simulations (black symbols) of dissociative adsorption on the fluorite (111) surface, fitted with a piecewise function.

The functional dependence of the log of pressure on coverage is described by piecewise

fitting describing four regions (fit to kMC data shown in Figure 10.11):

152

$$For\ \theta \in [0.023, 0.127875], \tag{44}$$

$$Log(\frac{P}{P^\circ}) = (-5.35059 + 0.961118 * Ln(\theta)) - Log(\frac{KP^\circ}{916313.5})$$

$$For\ \theta \in [0.127875, 0.795813], \tag{45}$$

$$Log(\frac{P}{P^\circ}) = (-8.3184 + 9.11649\theta - 11.4801\theta^2 + 7.58151\theta^3)$$

$$- Log(\frac{KP^\circ}{916313.5})$$

$$For\ \theta \in [0.795813, 0.9757], \tag{46}$$

$$Log(\frac{P}{P^\circ}) = (-192.777 + 664.601\theta - 787.854\theta^2 + 314.101\theta^3)$$

$$- Log(\frac{KP^\circ}{916313.5})$$

$$For\ \theta \in [0.97106, 0.996], \tag{47}$$

$$Log(\frac{P}{P^\circ}) = (24106.6 - 73723.9\theta + 75100.5\theta^2 - 25484.6\theta^3)$$

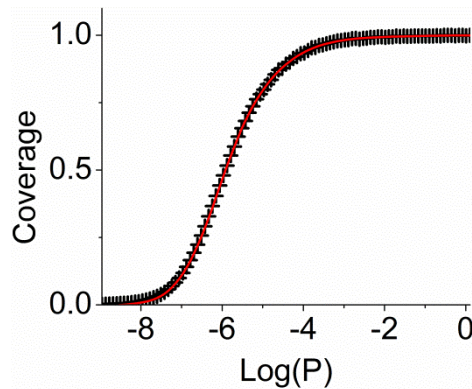$$- Log(\frac{KP^\circ}{916313.5})$$
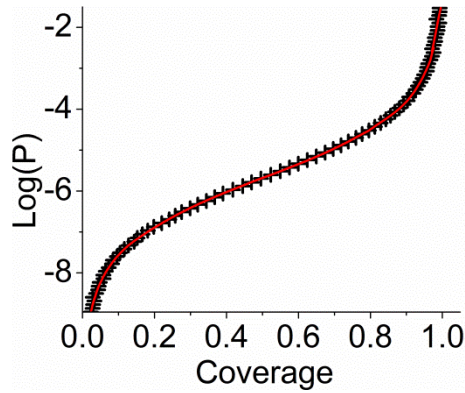
Figure 10.11 Functional dependence (red line) of pressure on coverage from kMC simulations (black symbols) of dissociative adsorption on the fluorite (111) surface, fitted with a piecewise function.

Again the shift along the pressure axis can be utilized to determine all adsorption isotherms

for dissociative adsorption on the Fluorite (111) surface geometry.

10.6   Discussion

By fitting to data obtained from kMC simulations, functional forms for the isotherms have

been calculated for the coverage as a function of the log of pressure and the log of pressure as a

function of coverage for molecular and dissociative adsorption processes on two distinct surface

geometries. The functional form is general, where all adsorption isotherms can be determined by

a horizontal shift of $c = \frac{w_2}{w_1}$ along the pressure axis as shown for the analytical solutions in Section

10.4. Interestingly, it was found, for both geometries and adsorption processes, that there was no cutoff coverage for this surface (i.e. that the coverage always reached 100 percent). In previous adsorption studies involving a second order dissociative molecular adsorption process on equal sites, it was found that there was a maximum coverage that the surface would reach that was close to 90 percent coverage [1, 28].

In Figure 10.12 a and b the kMC isotherms versus the analytical approximations in Eqs. 7 and 10 have been plotted. These plots give insights into what governs the functional forms of the isotherms, and similar qualitative behavior is observed for both surface geometries. At very low coverages (i.e. $\Theta < 0.01$), there is nearly perfect agreement between the KMC simulations and the analytical solution. This shows that at very low coverages, the approximation that the "adjacent anion sites" are always unoccupied is sufficiently accurate. For low coverages (i.e. $0.01 < \Theta < 0.1$), the KMC data for both non-dissociative and dissociative adsorption processes begin to deviate from the analytical solutions. The deviation for the case of dissociative adsorption is more extreme and results from an increasing concentration of isolated dissociated species occupying the surface: these are cases where an isolated M^+ species is left behind after the M^- species originally associated with it combines with a different M^+ and leaves behind the original M^+ as the remnant. Such isolated dissociated species have a longer residence time while they wait to find a new partner for leaving, and thus lead to an underestimation of the coverage from Eqs. 7 and 10.   From low to high coverage (i.e. $\Theta > 0.1$), the KMC data for molecular adsorption falls between the analytical solutions from Eq. 7 and 10: this is because in molecular adsorption, the filling of sites is correlated such that the odds of finding an open B site adjacent to an open A site are higher than the odds implied by Eq. 10. In contrast, for coverages greater than ~0.25 on both surface geometries, the KMC data for dissociative adsorption falls below both Eqs. 7 and 10. This results from an

increased accumulation of dissociated species. As the concentration of dissociated species increases, the surface contains an increasing number of isolated sites associated with isolated species -- and paired sites are necessary for adsorption to occur, causing the analytical solutions to overestimate the coverage. Ultimately, we find that the kMC simulations for the molecular adsorption cases are fairly well described byEq. 10, with differences from equation 10 are understandable, though the piecewise fitting from this work should be more accurate than Eq. 10 We find that the dissociative adsorption cases deviate significantly from both analytical solutions, and are thus only well described by the piecewise fitting from this work.
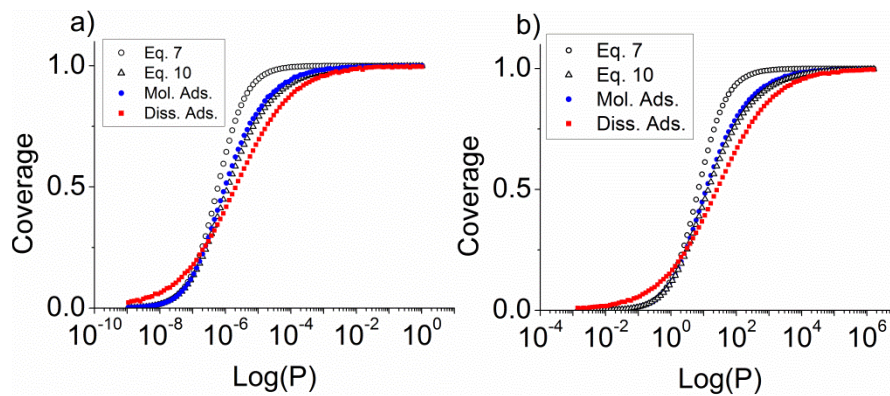
Figure 10.12 Comparison of KMC adsorption isotherms to analytical solutions in Equations 7 and 10 for a) the Fluorite structure KP°= 229078.4 and b) the perovskite structure for K P°= 0.018001.

The KMC simulations that have been performed in the current study do not consider any coverage dependence for adsorption, however, the same functional forms used here can be used when a coverage dependence is involved simply by using a coverage dependent equilibrium constant (i.e. $K(\Theta)$). If a coverage dependent K is being considered, it is recommended to use the piecewise fits which have beensolved for the log of pressure (e.g., Eqs 44-47) since in this case an explicit function is formed with all terms depending on Θ will appear on the right side of the equation. Attempting to use a coverage dependent equilibrium constant, $K(\Theta)$, in a piecewise fit that has been solved for coverage (e.g., Eqs. 42-43) form an implicit function which is harder to solve.

During our study, we found that the functional forms which were solved for coverage (e.g., Eqs. 42-43) were prone to numerical errors when using arbitrary values of K: this was due to machine rounding errors arising from the K terms with exponents of degree >1 (such numerical errors are more likely when using a program such as Excel rather than a program with less rounding, such as Mathematica). The functional forms solved for the log of pressure (e.g., 44-47) avoid such numerical errors, since in these expressions the K terms do not have any exponents of degree >1.

10.7   Conclusions

Generalized functional forms for adsorption isotherms have been obtained from fitting kMC simulated data for polar non-dissociative adsorption as well as polar dissociative adsorption processes on the perovskite surface(100) and fluorite (111) surface using KMC simulations. The results for the perovskite (100) surface are also applicable to cases with the NaCl(100) structure, since the geometry is the same. The functional forms provided give accurate values for the coverage as a function of pressure, or pressure as a function of coverage. In addition, they are applicable for any values of the equilibrium constant, and can even be used in cases where the equilibrium constant varies as a function of coverage, i.e. $K(\Theta)$. The functional forms which have been solved for the log of pressure (e.g., Eqs. 42-43) are less prone to numerical errors when using arbitrary values of K, and are also easier to solve when using a coverage dependent K.

10.8   Acknowledgments

References

[1]   R. I. Masel, *Principles of adsorption and reaction on solid surfaces* (Wiley, New York :, 1996), Wiley series in chemical engineering; Wiley series in chemical engineering.

[2]   W. Band, The Journal of Chemical Physics **8** (1940).

[3]   J. Cortes G., The Journal of Chemical Physics **71** (1979).

[4]   D. N. Misra, The Journal of Chemical Physics **52** (1970).

[5]   H. D. Hurwitz, The Journal of Chemical Physics **48** (1968).

[6]   L. Tonks, The Journal of Chemical Physics **8** (1940).

[7]   C. V. Heer, The Journal of Chemical Physics **55** (1971).

[8]   T. Keii, The Journal of Chemical Physics **25** (1956).

[9]   G. W. Woodbury, The Journal of Chemical Physics **77** (1982).

[10]   F. Fang, and I. Szleifer, The Journal of Chemical Physics **119** (2003).

[11]   C. A. J. Hoeve, The Journal of Chemical Physics **44** (1966).

[12]   G. Jura, and W. D. Harkins, The Journal of Chemical Physics **11** (1943).

[13]   G. L. Aranovich, J. S. Erickson, and M. D. Donohue, The Journal of Chemical Physics **120** (2004).

[14]   R. Gordon, The Journal of Chemical Physics **48** (1968).

[15]   K. G. Ayappa, C. R. Kamala, and T. A. Abinandanan, The Journal of Chemical Physics **110** (1999).

[16]   B. L. Severson, and R. Q. Snurr, The Journal of Chemical Physics **126** (2007).

[17]   L. H. Taylor, W. W. Longley, and P. J. Bryant, The Journal of Chemical Physics **43** (1965).

[18]   Y. Zhan, W. L. Mattice, and D. H. Napper, The Journal of Chemical Physics **98** (1993).

[19]   A. Martinez *et al.*, The Journal of Chemical Physics **126** (2007).

[20]   F. Moulin *et al.*, The Journal of Chemical Physics **127** (2007).

[21]   J. A. Boscoboinik, S. J. Manzi, and V. D. Pereyra, Physica A: Statistical Mechanics and its Applications **389** (2010).

[22]   A. Farkas, F. Hess, and H. Over, The Journal of Physical Chemistry C **116** (2012).

[23]   E. Hansen, and M. Neurock, Journal of Catalysis **196** (2000).

[24]   E. W. Hansen, and M. Neurock, Journal of Catalysis **196** (2000).

[25]   S. Matera, H. Meskine, and K. Reuter, J Chem Phys **134** (2011).

[26]   M. Stamatakis, and D. G. Vlachos, ACS Catalysis **2** (2012).

[27]   M. J. Hoffmann, S. Matera, and K. Reuter, Computer Physics Communications **185** (2014).

[28]   H. A. Bethe, Proceedings of the Royal Society of London. Series A, Mathematical and Physical Sciences **150** (1935).

11. Conclusions

In Part I of this dissertation, results were presented on the investigation of helium trapping at oxide nanoclusters in nanostructured ferritic alloys. The DFT investigation was performed on the Y_2O_3 and $Y_2Ti_2O_7$ systems and developed a strong theoretical framework of the trapping mechanisms of helium. In addition, an oxide nanocluster with the $Y_2Ti_2O_7$ structure was embedded in a BCC Fe system to give a complete picture of the interaction of helium with the oxide nanoclusters in NFAs. The results of this investigation can be described as follows:

- The formation energy of helium interstitials is significantly lower in the bulk oxides than in BCC Fe

- The migration barriers of helium are significantly higher in the oxides than in Fe

- Oxygen atoms play a key role in impeding the diffusive motion of helium defects

- Metal oxygen bonding in the oxide NCs gives rise to complex potential energy surfaces

- The potential energy landscape in BCC Fe contains very few potential energy-wells that are less spatially expansive than the oxide's and this is attributed to the metallic bonding in the crystal

- When the oxides are embedded in BCC Fe, spatially expansive potential energy-wells exist at oxide NCs due to the localized iono-covalent bonds that make trapping and subsequent nucleation of bubbles highly favorable

In Part II of this dissertation, two algorithms were successfully developed to overcome challenges associated with performing large numbers of KMC simulations with efficiency. The first algorithm overcomes problems caused by "KMC stiffness" that arise from large discrepancies between the fastest and slowest process rate constants. The algorithm overcomes this problem by dynamically throttling the transition probabilities based on the reaction rates at a given point in the KMC simulation and allows for a significant increase in the simulation time for complex chemical

159

reaction networks. The second algorithm detects steady-state using an on-the-fly statistical window-based method. The algorithm's three-part test was shown to be capable of automatically exiting any warm-up periods and detecting steady-state given a minimum quantity of required data to detect a steady-state within its loosest criteria. The final result in Part II was the development of a method to use KMC simulations as a means to derive a generalized functional form for adsorption isotherms that span the entire parameter space for the equilibrium constant and is independent of molecular, or surface species, but only depends on the surface geometry and the adsorption process.

Appendix A

The following assumptions and user defined criteria have been employed within the steady-state detection algorithm:

- The initial window size, *N*, is set to 100. This ensures that the standard error of the mean (i.e. standard deviation divided by the square root of the sample size) is 10% of the standard deviation. This assumption allows us to say that the initial sample size is large enough to contain a set of points that lie "close" to the sample mean.

- If two samples are capable of passing an f-test, where the null hypothesis is that the standard deviations of Window 1 and Window 2 are equal, then a sufficiently large sample has been gathered for performing further statistical tests. Having strict criteria that the sample standard deviations of Window 1 and Window 2 are equal allows us to ensure that any "warm-up" period that has extreme noise will be either dampened by a large enough sample to avoid significant skew, or the samples will grow large enough such that the algorithm shifts the window out of that region. This shifting occurs when if the sample size has grown to 10 x $N_{initial}$ (where $N_{initial}$ = 100 in the current work). This shifting criterion in the f-test is a user defined parameter that can be increased or decreased, but has been selected because at this point, the sample would be large enough such that the standard error would be 1% of the standard deviation, indicating that a large majority of the sample's points lie very close to the mean.

- Comparison of the means of Window 1 and Window 2 with a sufficiently large sample size will be a good indication of the similarity of the two windows and thus, a two-sample t-test can be used where the null hypothesis is that the two sample means are equal. This test is performed once the f-test is successfully passed. This test will continue to move the windows outside of the warm-up periods such as the steep ascents (and descents)

shown in Fig. 9.1 (a-c) by rolling by 1 and growing the window by 1. Thus, it is ensured that the sample size grows large enough, but that the growing size of the windows does not overshadow any potential skewness of the data (i.e. as the sample grows, the data comes closer and closer to the mean). If the data did not roll and grow as the t-test failed, the potential exists for small regions of the data inside of a warm-up period to trigger passing the t-test as shown in Figure A.1. The choice to roll by 1 and grow 1 by is user defined and has been chosen so that steady-state is detected at the earliest point. For cases where it is known that there is a very large warm-up period, the windows could roll and grow by a larger value, but in KMC, we have little to no knowledge of the initial trends *a priori*.

- Calculation of an extrapolated *y*-value with high enough confidence intervals is an indication of the extremity of a slope and indicative of a stationary state (or lack thereof). If the sample mean falls within the upper and lower bounds of the confidence intervals for the extrapolated value, it is safe to assume that any slope is sufficiently small and no significant change is occurring.

- The extrapolation test (slope test) is required to pass on *N* chronologically shifted windows before a positive indication of steady-state is given. This is a user defined requirement, and can potentially be too strict (or not strict enough) for certain systems and can hamper the efficiency of an SSD algorithm depending on the chosen value. It is always recommended to use a value of at least 2 for *N* to ensure that a detection of a miniscule change in the predicted *y*-value is not fortuitous.

- Confidence intervals for the f-test, t-test and prediction of an extrapolated y value at a future *x* value have each been set to 95%. This is user defined based on the desired

strictness of the steady-state detection (i.e. the higher the confidence intervals, the more difficult it is to pass the test, but there is also increased certainty in the detection of a steady-state). It is highly recommended that the confidence intervals are taken to be 95% as decreasing this value will inherently increase the likelihood that steady-state is inaccurately, or prematurely, detected, thus only 95% confidence intervals will be tested in the current work.

- All statistical quantities (i.e. standard error, standard deviation, mean) have used means that are weighted by the amount of time in the associated snapshot to account for the fact that the EFs within a given window do not represent the same interval of time. This is necessary because the VSSM is used during the KMC and thus, certain time steps are significantly longer than others for a given snapshot. Two methods will be discussed for the predicted EF: 1) where the regression is performed with weighted residuals and 2) where the regression is performed without weighted residuals. In both cases, the weighted mean was still used for all quantities.

- The EF is taken to be representative of the midpoint of the time step (i.e. $t_{mdpt} = \frac{t_{final} + t_{initial}}{2}$) and thus, the (x,y) data points are given as (t_{mdpt}, EF). This technique has been employed because the EF reported at the end of a snapshot is a time average of the number of events that has occurred throughout the entire snapshot and thus, this more accurately represents the difference in time between two sequential events between two snapshots.
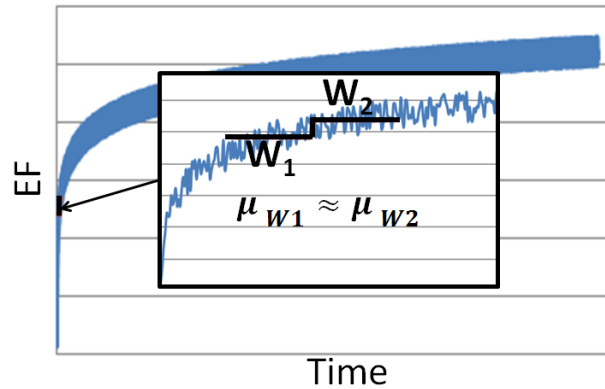
Figure A. 3 Small regions can exist within the warm-up period where the mean of two samples can be approximately equal. Thus, it is important to have large enough windows such that the mean is taken over a sufficiently large sample to avoid premature confirmation of passing the t-test.

Steady-State Detection Algorithm

Step 1 (f-test)

1. Create overlapping windows of EF output data (i.e. the final point in Window 1 is the first point in Window 2) with a minimum initial size of $N = 100$.

   a. Perform f-test to check if the standard deviations of Window 1 and Window 2 are the same to within 95% confidence (i.e. $\sigma_1 = \sigma_2$).

      i. If $\sigma_1 \neq \sigma_2$:

         1. $N = N+1$ (i.e. append Window 1 and Window 2 with one additional EF)

            a. If $N < 10 \times N_{initial}$:

               i. Repeat Step 1.1.a until $\sigma_1 = \sigma_2$) or until $N = 10 \times N_{initial}$

            b. else if $N = 10 \times N_{initial}$:

               i. Shift Windows 1 and Windows 2 and reset N to $N_{initial}$ (i.e. The first point in Window 2 becomes the first point in Window 1 with $N = 100$, The final point in the shifted Window 1 becomes the first point in Window 2 with $N = 100$)

               ii. Repeat step 1.1.a

      ii. If $\sigma_1 = \sigma_2$:

Step 2 (t-test)

   1. Calculate the mean of Window 1 and the mean of Window 2 (i.e. μ_1 and μ_2)

      a. If $\mu_1 = 0$ or $\mu_2 = 0$:

         i. $N = N+1$ (i.e. add another EF data point to Window 1 and Window 2)

ii. Repeat Step 2.1

b. If $\mu_1 \neq 0$ and $\mu_2 \neq 0$:

i. Perform two-sample t-test to check if $\mu_1 = \mu_2$

1. If $\mu_1 \neq \mu_2$:

a. Shift Window 1 by one point and make N = N+1 (i.e. "Roll and Grow Windows" -- First point in Window 2 becomes the new last point in Window 2)

b. Repeat Step 2.1

2. If $\mu_1 = \mu_2$:

Step 3 (slope-test)

1. Merge Window 1 and Window 2, calculate the mean (μ) and the predicted value of the slope ($\hat{y}$) at a value x^* and the associated upper and lower bounds ($\hat{y}_{upper}$ and $\hat{y}_{lower}$) of the 95% confidence intervals of $\hat{y}$ at x^* (keep track of indices of Window 1 and Window 2 at this step)

a. If ($\left|\frac{\hat{y}-\hat{y}_{upper}}{\hat{y}}\right| \leq 0.05$ or

$\left|\frac{\hat{y}-\hat{y}_{lower}}{\hat{y}}\right| \leq 0.05$) and

($\hat{y}_{lower} \leq \mu \leq \hat{y}_{upper}$):

i. Shift Window 2 becomes Window 1, Window 2 is shifted by N (final index of new Window 1 becomes first index of new Window 2)

ii. Repeat Step 3.1 until 3.1.a is passed in N consecutive tests (**When this test is passed N consecutive times, steady-state is reached for the reaction process**).

b. Else:

      i. "Roll and Grow" Window 1 and Window 2 (i.e. N = N+1)

     ii. Repeat Step 2.1

Figure A. 4 The steady-state detection algorithm as applied to a single reaction process. When each reaction process's EF data has successfully triggered steady-state, it is safe to assume that the simulation has reached steady-state.

Appendix B: Copyright Permission Letters

This is a License Agreement between Thomas L Danielson ("You") and Elsevier ("Elsevier"). The license consists of your order details, the terms and conditions provided by Elsevier, and the payment terms and conditions.

Get the printable license.

License Number	3833770229043
License date	Mar 21, 2016
Licensed Content Publisher	Elsevier
Licensed Content Publication	Journal of Nuclear Materials
Licensed Content Title	Structural and electronic effects of helium interstitials in Y2Ti2O7: A first-principles study
Licensed Content Author	Thomas Danielson,Celine Hin
Licensed Content Date	September 2014
Licensed content volume number	452
Licensed content issue number	1-3
Number of pages	8
Type of Use	reuse in a thesis/dissertation
Portion	full article
Format	both print and electronic
Are you the author of this Elsevier article?	Yes
Will you be translating?	No
Title of your thesis/dissertation	Investigation of static and dynamic reaction mechanisms at interfaces and surfaces using density functional theory and kinetic Monte Carlo simulations: Part I The ab initio investigation of helium trapping at oxide Nanoclusters in Nanostructured ferritic alloys and Part II: Addressing challenges associated with Kinetic Monte Carlo Simulation of Complex Chemical Reaction Networks
Expected completion date	Apr 2016
Estimated size (number of pages)	150
Elsevier VAT number	GB 494 6272 12
Price	0.00 USD
VAT/Local Sales Tax	0.00 USD / 0.00 GBP
Total	**0.00 USD**

Dear Thomas Danielson,

Thank you for your email and for taking the time to seek this permission.

When you transferred the copyright in your article to IOP, we granted back to you certain rights, including the right to include the Accepted Manuscript of the article within any thesis or dissertation. Please note you may need to obtain separate permission for any third party content you included within your article.

Please include citation details, "© IOP Publishing. Reproduced with permission. All rights reserved" and for online use, a link to the Version of Record.

The only restriction is that if, at a later date, your thesis were to be published commercially, further permission would be required.

Please let me know if you have any further questions.

In the meantime, I wish you the best of luck with the completion of your dissertation.

Kind regards,

Kathryn Shaw

Copyright & Permissions Team
Gemma Alaway – Rights & Permissions Adviser
Kathryn Shaw - Editorial Assistant